Fundamental Investigation of Thermal and Mechanical Properties of High-Entropy Alloys via Composition and Structural Analysis

A Dissertation Presented for the

Doctor of Philosophy

Degree

The University of Tennessee, Knoxville

Md Abdullah Al Hasan

May 2024

ACKNOWLEDGEMENTS

To begin, I deeply cherish the unconditional love and support of my beloved wife, and I extend heartfelt thanks to my father, mother, and siblings for their steadfast belief in me.

Beyond my family, I am profoundly grateful to my advisor, Dr. Seungha Shin, for his selfless support and vast knowledge throughout my Ph.D. journey and dissertation process. His expertise and guidance helped me stay focused and progress smoothly. Dr. Shin has also been a remarkable mentor in my personal life, and I owe much of today's achievement to his training and mentorship.

I would also like to express my appreciation to the rest of my Ph.D. committee: Dr. Anming Hu, Dr. David J. Keffer, and Dr. Peter K. Liaw, for their insightful feedback and encouragement during my research.

Lastly, my sincere thanks go to my colleagues, particularly Jiaqi Wang and Yu-Kai Weng, for their support and encouragement. I must also acknowledge the friends and companions I've had the privilege to know over the years, including Robin, Bushra, Latif, Maruf, Arup, and Sumi, whose unconditional support has been invaluable throughout this journey. Thank you all for helping me become a better person.

ABSTRACT

High-entropy alloys (HEAs), specifically AlCoCrFeNi HEAs, have attracted significant attention for their distinct microstructures and adjustable properties. To enhance the energy conversion efficiency, stability, and mechanical performance of their applications, further refinement or fine-tuning of the thermoelectric, thermodynamics, and mechanical properties of such HEAs is necessary. Effective analysis and design of HEAs require a comprehensive understanding of the effects of various structural parameters, such as composition and structural orders. However, the structural complexities and vast configurational space of HEAs have posed challenges in advancing the required fundamental understanding.

This research aims to develop an effective methodology capable of addressing elemental compositions and structural orders, thereby elucidating the understanding of the effects of various structural parameters on HEA properties. For this study, molecular dynamics (MD) simulations, Monte Carlo (MC) simulations, first-principles calculations, and Machine Learning (ML) techniques were employed, as they enabled the investigation of atomic properties and efficient data processing.

Firstly, this study investigated the influence of aluminum (Al) content on phonon transport and thermoelectric properties in $Al_xCoCrFeNi$ HEAs across a wide temperature range. Low Al concentrations were found to reduce phonon conductivity, increasing thermoelectric performance with minimal temperature dependence. Conversely, electrical conductivity and Seebeck coefficient increased with temperature, particularly at higher Al concentrations, enhancing the thermoelectric performance. Secondly, the effects of short-

range order (SRO) on the thermodynamic properties of $Al_xCoCrFeNi$ HEAs were examined, revealing prevalent negative SRO of Al-Fe and positive SRO of Al-Al pairs. SRO impacts the lattice thermal conductivity, bulk modulus, and thermal expansion coefficient, thereby aiding in the design of HEAs with tailored properties via structural tuning. Finally, machine learning models were trained with SRO parameters to predict yield strength of AlCoCrFeNi HEA families, deepening understanding of the SRO-mechanical property relationship and aiding in the design of HEAs for improved mechanical strength.

This study provides insights into the interactions among element concentrations, local atomic order, and physical properties of HEAs, thereby advancing the development of a quantitative theory-guided HEA design strategy for specific applications and energy conservation efforts. It also establishes a foundation for further studies extending into the design and optimization of other HEA systems.

TABLE OF CONTENTS

LIST OF TABLES

LIST OF FIGURES

Chapter 1

Introduction

1.1 Background: High-Entropy Alloys

Since the dawn of civilization, humans have been relentlessly searching for new materials with improved properties. This quest has intensified significantly in modern times due to growing demand across various applications in aerospace engineering, automobile, manufacturing, construction, energy, nuclear technology, and weapons. To meet this demand, researchers have been dedicated to developing materials with excellent thermal properties, high yield strength, and high ductility. For developing such materials, alloying and precipitate inclusion have been regarded as the most effective methods.

Conventional alloying, involving minor additions of one or more elements to the principal component, plays a significant role in acquiring promising changes to physical, mechanical, and chemical properties [1]. This traditional alloy technique was fortuitously discovered around 3,000 BC, by developing Bronze, a mixture of copper and tin. Since then, alloy development has predominantly focused on one or two primary elements, leading to the development of steels, Ti-Al intermetallics, bulk metallic glasses, and so on [2-5]. However, with modern technology pushing limits to this fabrication method of materials via conventional alloying, the need to find next-generation materials to optimize for several applications became imminent.

Surprisingly, the process of developing alloys composed of multi-principal elements took numerous decades. Initially, scientists anticipated that mixing several elements would result in the formation of many intermetallic compounds and complex microstructure, leading to poor mechanical properties [6]. To prevent the development of intricate microstructures, alloy design was typically limited to one or two principal elements. In contrast, B. Cantor along with his student A. Vincent [7] carried out first experimental investigations of 20-component alloys aiming to develop equiatomic multicomponent alloys around 1981. Subsequently, an extension of this investigation revealed that one composition of $Co_{20}Cr_{20}Fe_{20}Mn_{20}Ni_{20}$ at% exhibited a single face-centered cubic (FCC) phase, demonstrating that alloying multiple elements resulted in a single solid solution [8, 9]. Yeh also contributed to research on multi-component alloys around 1995, exploring different combinations of various elements, such as Ti, Cu, Ni, V, Al, Co,

Mo, and Zr, and reported numerous exciting properties, such as improved hardness and strengths in 2004 [10]. Due to multiple reports of these enticing properties at that time, 2004 was regarded as the birth year of multicomponent alloys, later referred to as high-entropy alloys (HEAs) with the potential to become next-generation materials [8, 10].

High-entropy alloys are composed of at least five elements, with each element's concentration ranging from 5 to 35 at% [11]. The formation of stable solid solution originates from the large-configurational entropy of the alloys [10]. This configurational entropy is defined as

$$\Delta S_{conf} = -R\sum_{i=1}^{N} c_i \ln c_i, \tag{1.1}$$

where R is the gas constant = 8.314 J/mol-K, c_i is the atomic fraction of each element. When the concentration of each element of an alloy is equimolar, the entropy is maximized, and the configurational entropy becomes

$$\Delta S_{conf} = R \ln N, \tag{1.2}$$

where N is the number of constituting elements. As N increases, the configurational entropy increases, and it is regarded as a criterion to determine high entropy alloys. If the ideal configurational entropy is larger than $1.5R$, the multicomponent alloys are defined as high-entropy alloys. Conventional alloys having configurational entropy lower than $1.5R$ are known as low-entropy alloys. Table 1.1 shows the configurational entropy with respect to the number of constituent elements using Eq. (1.2) [12, 13].

While increasing the number of constituent elements results in higher configurational entropy, containing more than 13 elements does not lead to a significant increase in entropy. Therefore, 5 to 13 elements in a HEA would be sufficient to maximize configurational entropy.

Table 1.1: Configuration entropy with respect to number of constituent elements of alloys

N	1	2	3	4	5	6	7	8	9	10
ΔS_{conf}	0	$0.69R$	$1.1R$	$1.39R$	$1.61R$	$1.79R$	$1.95R$	$2.08R$	$2.2R$	$2.3R$

However, it is observed that the concept relying solely on configurational entropy for the creation of solid solutions has sparked debate within this HEA field [14-20]. This is because multiple research investigations have discovered the presence of compounds and secondary phases in many HEAs [15, 19, 21]. Configurational entropy is crucial for stabilizing single-phase HEAs, while enthalpy and non-configurational entropy are pivotal in HEAs with phase separation [15]. In addition, melting temperature, processing temperature, interatomic correlations can also affect this formation of random solid solution [14]. Recent studies [22-25] suggest that alongside high configurational entropy, atomic-level stresses resulting from mixing different-sized elements in HEAs are equally crucial. In these HEAs, mismatches in atomic size and chemical interaction frequently induce short-range orders, thereby impacting the system's energetics, enthalpy, and phase diagram [25, 26].

Investigations of the single and multi-phase HEA gained significant traction among materials researchers, primarily due to the phase stability at high temperatures and enhanced physical properties. These include excellent thermal stability, superior fracture toughness, improved wear and corrosion resistance, and so on, compared to the traditional alloys [9-11, 27-30]. In the majority of research, HEAs are synthesized with the goal of attaining a single phase exhibiting superior properties, often compared to conventional alloys composed of individual constituent elements. For example, VCrMnFeCoNi HEA demonstrates outstanding cryogenic mechanical properties, demonstrating a yield strength exceeding 1 GPa [31] and the fatigue performance of $Al_{0.5}CrFeCoNiCu$ HEA exhibits a fatigue endurance limit to ultimate tensile strength ratio similar to that of conventional alloys [32]. Refractory HEAs, such as $Nb_{25}Mo_{25}Ta_{25}W_{25}$ and $V_{20}Nb_{20}Mo_{20}Ta_{20}W_{20}$, exhibit a significantly higher yield strength at elevated temperatures compared to conventional superalloys. Also, the wear resistance of $Al_{0.2}CrFeCo_{1.5}Ni_{1.5}Ti$ and $CrFeCo_{1.5}Ni_{1.5}Ti$ HEAs due to the excellent anti-oxidation property, surpasses that of traditional wear-resistant steels [33]. Al-Cr-Mn-Fe-Ni HEA exhibits exceptional workability, extending up to 4,260% in rolling without encountering any cracks [29].

Despite the considerable research conducted on the physical properties of HEAs, numerous questions remain unanswered, and many combinations of elements remain unexplored, primarily

due to the extensive composition space that is present in HEAs. For instance, limited research has explored leveraging the second phase's benefits in the HEAs, where proper alloy design can enhance various high-temperature properties such as strengthening, grain growth resistance, softening, and oxidation resistance [34]. While HEAs are considered potential materials for high-temperature applications, most property investigations are limited to room temperature according to literature review. In addition, due to their diverse compositions, HEAs can exhibit significantly varied properties, potentially surpassing those of conventional alloy systems like steels, however, many HEAs investigated so far are too brittle to be deemed practical for engineering applications [35]. Moreover, the requirement of precise control of intermetallic phase sizes and volume fractions poses a significant challenge in studying multiphase HEAs [36]. Besides, local atomic ordering or chemical short-range order is considered as a key factor influencing structural and mechanical properties of HEAs, however, research on it remains limited due to challenges in handling experimental complexities and interpreting pair correlations [37, 38]. Furthermore, a key challenge in HEAs lies in the need to balance multiple properties, as studies have often focused on singular properties of interest rather than the combination required for most applications [39, 40].

Nevertheless, HEAs present a novel and promising avenue for alloy design, particularly in the realm of structural materials. In this regard, the research emphasis should shift from pursuing single-phase HEAs to the development of alloys that achieve the appropriate balance of mechanical properties. Efficient research efforts in exploring HEA compositions require careful sampling of the vast compositional space to navigate the extensive number of potential candidates. In this regard, rapid-throughput screening methods may be required for evaluating potential compositions, with the careful assessment of the risk of prematurely discarding promising alloys due to their limited exploration of the intricate relationships between heat treatment, microstructure, and properties [35]. Future research efforts should prioritize both experimental and theoretical investigations aimed at studying and identifying the formation of local atomic ordering and its impacts on properties, as this represents a relatively novel research avenue in the field. Therefore, comprehensive evaluation of HEAs for their applicability as

structural materials requires substantial collaborations, integrating theoretical and computation analysis, modern data analytics, and experimental investigations. Enhanced understanding through comprehensive understanding will facilitate the practical application of HEAs.

1.2 Motivations and Objectives

The prominent difference between HEAs and conventional alloys can be attributed to the four core effects of HEAs, namely the high entropy effect, severe lattice distortion effect, sluggish diffusion effect, and cocktail effect, as illustrated in Fig. 1.1 [10, 41]. The high entropy effect is related to the stabilization of solid solution phases of HEAs, i.e., obtaining a simple microstructure. High configurational entropy lowers the thermodynamic free energy of solid solution phases, thus enhancing the formation of solid solution rather than complex intermetallic compounds in the near equimolar alloys containing five or more principal components [27, 41]. This can be demonstrated by the minimization of the Gibbs free energy (ΔG) equation [13]

$$\Delta G = \Delta H - T\Delta S, \tag{1.3}$$

where ΔH is the enthalpy and T is the temperature. As the number of components in an alloy increase, the configurational entropy rises with temperature causing the increase of $T\Delta S$. This facilitates the reduction of Gibbs free energy and the stabilization of phases in HEAs.

The severe lattice distortion effect arises from the different atomic sizes of the multiple constituent elements in an HEA. All atoms, being solute and significantly different in size, contribute to this lattice distortion, which is notably higher than in conventional alloys [29]. These distortions are also believed to improve the mechanical strength of the HEAs, especially in the body-centered cubic (BCC) HEAs [41].

The sluggish diffusion effect originates from the interactions between the elements of the HEAs. In order to reach phase equilibrium, all elements in the HEAs need to diffuse mutually. However, in HEAs, this event is hindered by the different atomic sizes. This effect, combined with the

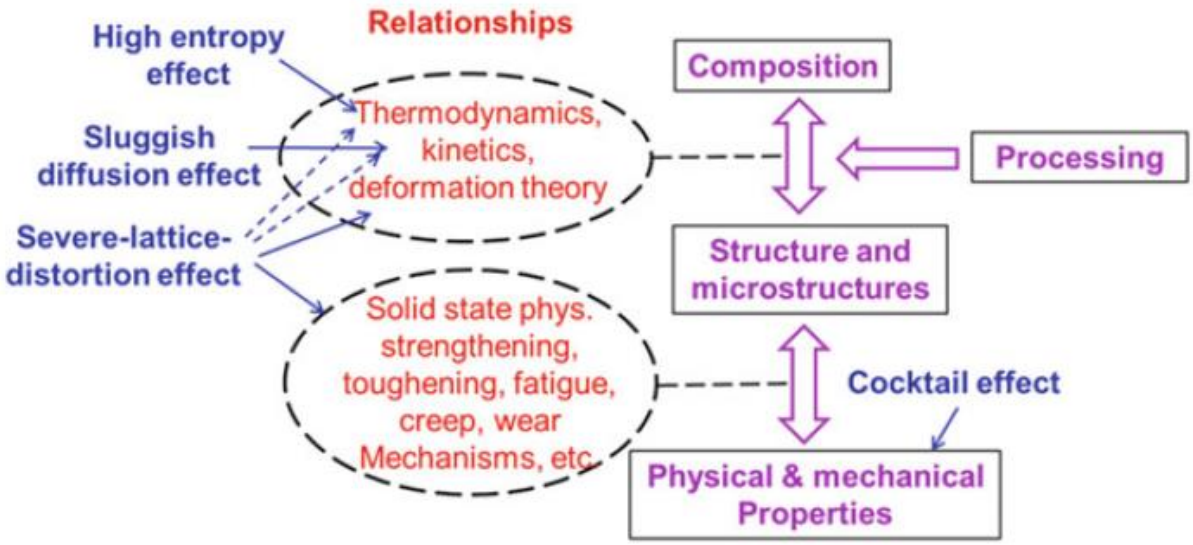

Figure 1.1: Illustration of the core effects of high-entropy alloys (HEAs) [42].

lattice distortion effect, can impede the atomic movement and lower the effective diffusion rate, hence named as sluggish diffusion [29]. This effect can be utilized to control the physical and chemical properties to enhance the performance of the HEAs.

The cocktail effect stems from alloying and changes in elemental compositions [41, 43, 44]. This effect can facilitate the generation of novel properties which cannot be observed otherwise from independent elements. For instance, adding lighter elements in the $Al_xCoCrCuNi$ HEAs significantly reduce the overall density while adding oxidation-resistant materials, such as Al, Cr, and Si, can increase oxidation resistance at higher temperatures [29]. Thus, the cocktail effect can be harnessed to obtain desirable properties by tailoring the components of HEAs.

To summarize, the four core effects are directly correlated with the properties of HEA: the high-entropy effect relates to HEA's phase formation and thermodynamics, the severe lattice distortion affects the strength, the sluggish diffusion is associated with kinetics, and the cocktail effect contributes to improved properties.

Composition of HEAs plays a crucial role in determining their functional properties. The majority of HEAs are categorized into either Cantor HEAs or refractory HEAs (Senkov) based on their compositions. Various microstructural phase formations, such as single FCC, single BCC, FCC+BCC, or hexagonal close packed (HCP), occur depending on the element concentration, as shown in Fig. 1.2. Generally, Al, Cr, Co, Fe, Ni, and Cu mostly form Cantor HEAs where Mo, Nb, Ta, or W-containing HEAs are labeled as refractory HEAs. Among the Cantor HEAs, Al-containing HEAs are regarded to be important due to their flexibility in modifying crystal structures. Being different in terms of atomic size and mass compared to other constituent elements in $Al_xCoCrFeNi$ HEA, Al content has a significant influence on this HEA's microstructural properties [45-50]. A larger size of Al atoms in $Al_xCoCrFeNi$ HEA induces higher lattice distortion that leads to the relaxation of this HEA by changing its phase formation, such as single or dual-phase microstructure [45-47]. Therefore, $Al_xCoCrFeNi$ HEA needs to be studied extensively to utilize this Al concentration effect to tailor HEAs with desirable properties.

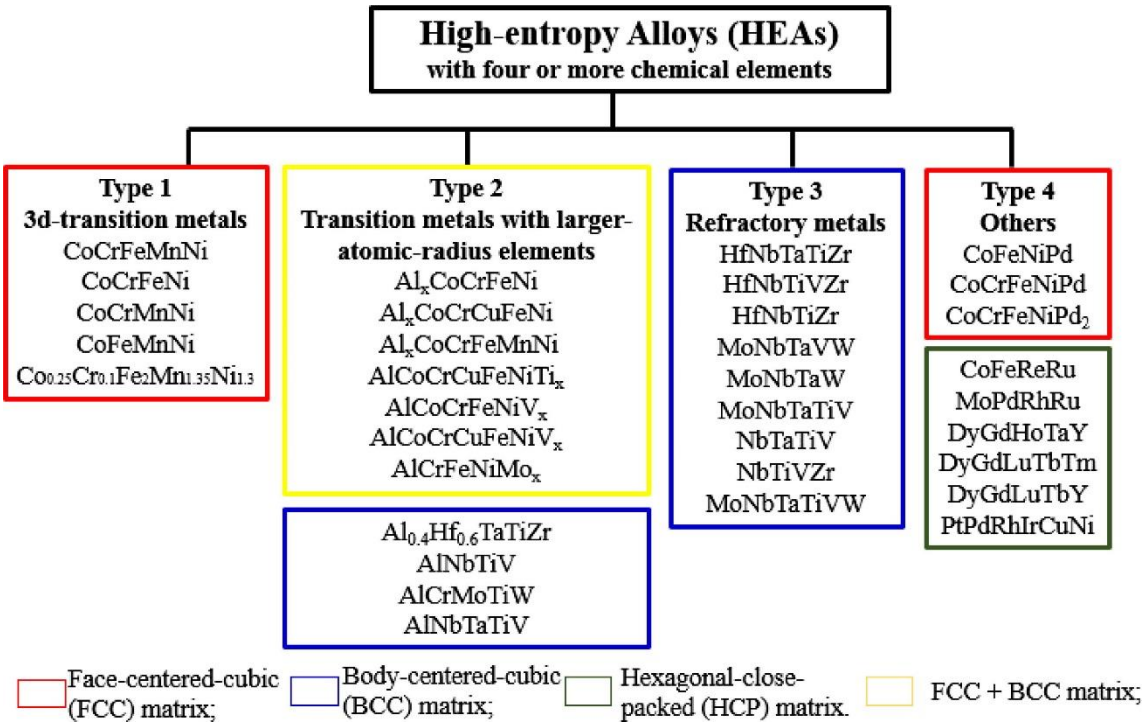

Figure 1.2: Categorization of HEAs according to their crystal structure and compositions [42].

In this research, a comprehensive investigation of the $Al_xCoCrFeNi$ HEA was conducted via composition and structural analysis aiming to achieve desirable material properties.

1.3 Methodology: Atomistic Modeling and Modern Data Analytics

Computational modeling and simulations have proved themselves as essential measures besides experiments to advance the materials science knowledge and discovery. Various simulation techniques have been employed to this date for modeling materials behavior and properties. Specifically, multiscale simulations have become very popular in recent times due to their strength in proving different time-length phenomena while simulating materials and extracting their properties. In this study, multiscale simulations, i.e., quantum-scale: first-principles calculations, atom-scale: classical molecular dynamics simulations, meso-scale: Boltzmann transport theory, and modern data analytics have been employed. To initiate any knowledge on a material, quantum-scale first-principles calculations, i.e., *ab-initio* molecular dynamics simulations are required, since this enables examining electron behavior in a material and provide us with important properties and behavior without any prior knowledge on that specific material. Then, to study the atomic dynamics and extract structural and dynamic properties, classical molecular dynamics simulations are essential. Moreover, to investigate properties of thermal transport or thermoelectric conversion, Boltzmann transport calculations can be useful. Finally, to integrate all the obtained information and predict material properties quickly, modern data analytics, i.e., correlation analysis and machine learning are essential.

1.3.1 Density Functional Theory

Density functional theory (DFT) has been extensively used to enhance understanding in materials science over the past few decades. It allows researchers to analyze complex materials and obtain essential information in cases where experimental investigations are challenging. DFT simplifies the complex problem of many-body interaction by treating system properties as functions of particle density, allowing for independent analysis of each particle's wavefunction based on three-dimensional density.

Here, the electron calculations are determined by the time-dependent Schrödinger equation, [51],

$$i\hbar\frac{\partial}{\partial t}\psi\left(\{\boldsymbol{r}_i\},\{\boldsymbol{R}_I\};t\right)=\hat{H}\psi\left(\{\boldsymbol{r}_i\},\{\boldsymbol{R}_I\};t\right), \tag{1.7}$$

where $\psi(\boldsymbol{r},\boldsymbol{R};t)$ represents the electronic wavefunction, $\hat{H}$ represents Hamiltonian operator for the electronic system, $\hbar$ is the reduced Planck constant, $\{\boldsymbol{r}_i\}$ represents position of electron *i*, and $\{\boldsymbol{R}_I\}$ denotes the position of nuclei *I*.

The many-body Hamiltonian $\hat{H}$ can be expressed as:

$$\begin{aligned}\hat{H}&=-\sum_I\frac{\hbar^2}{2M_I}\nabla_I^2-\sum_i\frac{\hbar^2}{2m_e}\nabla_i^2-\sum_{i<j}\frac{e^2}{\left|\boldsymbol{r}_i-\boldsymbol{r}_j\right|}-\sum_{I,i}\frac{e^2Z_I}{\left|\boldsymbol{R}_I-\boldsymbol{r}_i\right|}+\sum_{I,i}\frac{e^2Z_IZ_J}{\left|\boldsymbol{R}_I-\boldsymbol{R}_J\right|}\\&=-\sum_I\frac{\hbar^2}{2M_I}\nabla_I^2-\sum_i\frac{\hbar^2}{2m_e}\nabla_i^2+V_{n-e}\left(\{\boldsymbol{r}_i\},\{\boldsymbol{R}_I\}\right)\\&=-\sum_I\frac{\hbar^2}{2M_I}\nabla_I^2+\hat{H}_e\left(\{\boldsymbol{r}_i\},\{\boldsymbol{R}_I\}\right)\end{aligned} \tag{1.8}$$

where m_e is the electronic mass, e is the electronic charge, M_I is the mass of nuclei *I*, and *Z* is the atomic number.

In this equation, solving the electronic Hamiltonian, $\hat{H}_e\left(\{\boldsymbol{r}_i\},\{\boldsymbol{R}_I\}\right)$ analytically is impractical, thus requires approximation methods for electronic structure, which typically demands significant computational resources. Currently, the Kohn-Sham (KS) formulation of density functional theory stands as the predominant approximation for electronic structure calculations [52]. In this approach, the total energy is represented as a functional of mutually orthogonal single-particle electron orbitals $\psi_i(\boldsymbol{r})$ (where *i* ranges from 1 to n_e, the number of electrons). The KS energy functional comprises four components: the kinetic energy of a non-interacting reference system, the Hartree energy (which represents the classical electrostatic energy between two charge clouds arising from the electronic density), exchange-correlation energy, and the

energy contributed by a fixed external potential. Here, the exchange-correlation energy necessitates approximation when computing the total energy.

1.3.2 Classical Molecular Dynamics Simulations + *Ab Initio* Molecular Dynamics Simulations

Classical Molecular Dynamics Simulations:

Classical molecular dynamics (MD) simulation is a computational technique used to study the dynamics and behavior of atoms over time. Here, the motion of atoms and molecules is described using classical mechanics, where each particle is treated as a point mass with a set of interactions governed by Newton's laws of motion. MD simulations are extensively employed in materials science to investigate the structural and dynamical properties of various materials at the atomic and molecular level. This is a powerful tool for exploring diverse phenomena such as phase transitions, defect formation, mechanical behavior, and thermal properties across a wide range of materials, including metals, semiconductors, polymers, and ceramics. By simulating the interactions between atoms or molecules based on interatomic force fields, researchers can gain insights into the underlying mechanisms governing material behavior, facilitating the design and optimization of new materials with tailored properties for specific applications.

The basic principles of Classical Molecular Dynamics (CMD) are rooted in Newtonian physics, wherein the potential energy is determined using a prescribed empirical or semi-empirical mathematical formula, typically focusing solely on the interactions between atomic nuclei, as shown in Eq. 1.4 [53],

$$M_I \ddot{\boldsymbol{R}}_{\boldsymbol{I}} = -\frac{\partial}{\partial R_I}\left[U\left(\boldsymbol{R}_{\boldsymbol{I}}\right)\right], \tag{1.4}$$

where $\boldsymbol{R}_I$ denotes the atomic position, $U\left(\boldsymbol{R}_I\right)$ denotes the interatomic potential energy and is traditionally split into 1-body, 2-body, 3-body terms and so on, as [53],

$$U(\boldsymbol{R}_I) = \sum_i u(\boldsymbol{R}_I) + \sum_i \sum_{j>i} v(\boldsymbol{R}_I, \boldsymbol{R}_J) + \sum_i \sum_{j>i} \sum_{k>j>i} w(\boldsymbol{R}_I, \boldsymbol{R}_J, \boldsymbol{R}_K) + ..., \quad (1.5)$$

where, $U(\boldsymbol{R}_I)$ represents 1-body term, originating from an external potential field or boundary condition. $v(\boldsymbol{R}_{IJ}) = v(\boldsymbol{R}_I, \boldsymbol{R}_J)$ represents 2-body term, also known as the pair potential, which is solely determined by the distance between atoms and remains unaffected by the existence of additional atoms. The inclusion of a third atom alters the interaction between a pair of atoms, giving rise to the 3-body term, $w(\boldsymbol{R}_{IJK}) = v(\boldsymbol{R}_I, \boldsymbol{R}_J, \boldsymbol{R}_K)$. Typically, in full periodic simulations of bulk systems, the single-body component, $u(\boldsymbol{R}_I)$ is often disregarded, with primary attention directed towards the pair potential, $v(\boldsymbol{R}_{IJ})$ while the 3-body term, $w(\boldsymbol{R}_{IJK})$ and interactions of higher orders are typically neglected.

Interatomic potential can be classified into two main types: two-body and many-body potentials. Two-body potentials, exemplified by models like Lennard-Jones [54], Morse [55], and Buckingham potential [56], rely on a predetermined functional relationship for atomic interactions. These models adjust their parameters to match experimental data, thereby replicating material properties. The many-body potential typically originates from quantum-mechanical simulations, where it is obtained by fitting a potential energy surface. This potential may not follow a parameter-based analytical expression, such as those seen in models like the embedded atom method (EAM) [57] potential and bond order potential (BOP) [58]. Once the interatomic potential is established, it becomes possible to compute the forces exerted on atoms, which in turn dictate the evolving dynamics of the simulation system. Therefore, the interatomic potential plays a crucial role in MD simulations as it directly impacts the precision of simulation outcomes.

In this research, I have implemented EAM potential for MD simulations due to its distinctive capacity to comprehensively represent the complex interactions inherent in metallic bonding, leading to widespread adoption and notable achievements in simulating metallic materials [59,

60]. These highly effective and precise models have played a pivotal role in replicating various metal processes at the atomic level, encompassing deformation, diffusion, and sintering [57, 60, 61]. The total energy (U) of an EAM potential applied to a group of N atoms is expressed as follows:

$$U_{EAM} = \frac{1}{2}\sum_{\substack{I,J=1 \\ I\neq J}}^{N} v\left(\boldsymbol{R}_{IJ}\right) + \sum_{J=1}^{N} F_J\left[\sum_{\substack{J=1 \\ I\neq J}}^{N} \rho_{IJ}\left(\boldsymbol{R}_{IJ}\right)\right], \tag{1.6}$$

where $v\left(\boldsymbol{R}_{IJ}\right)$ is the two-body interaction, ρ_{IJ} is the electron density combined by atom *I* at atom *J*, and F_J represents the embedding function for atom *J*. To prevent duplicate computation of pairwise interactions, a factor of 1/2 is incorporated into the first term.

In addition to the interatomic potential, there are numerous other essential parameter configurations within CMD that may impact both the speed and accuracy of simulations. These include the (a) integration algorithm, (b) ensemble selection, (c) boundary condition, and (d) timestep. These parameters will be briefly discussed in the subsequent paragraphs.

(a) Integration Algorithm:

The potential energy function, $U\left(\boldsymbol{R}\right)$ is a complex equation involving 3N (where N is the number of atoms) coordinates of all atoms in the system. Since there is no analytic solution due to the complexity of the equations of motion, numerical solutions are required. Various integration algorithms such as Verlet [62], velocity Verlet [63], and leapfrog [64] have been developed. Among these, the velocity Verlet algorithm is commonly preferred today due to its enhanced accuracy compared to the traditional Verlet algorithm. Thus, I have applied the velocity Verlet algorithm to conduct all my MD simulations in this research project.

(b) Ensemble Selection

An ensemble represents a set of all potential states of a system, each possessing distinct microscopic characteristics while sharing an identical macroscopic or thermodynamic state. Various ensembles exist, each with unique attributes:

1. Microcanonical ensemble (*NVE*) [65] describes an isolated system with a fixed number of atoms (*N*), volume (*V*), and energy (*E*).

2. Canonical ensemble (*NVT*) [66] encompasses states of a system with a fixed number of atoms (*N*), volume (*V*), and temperature (*T*).

3. Isobaric-isothermal ensemble (*NPT*) [66] encompasses states of a system with a fixed number of atoms (*N*), pressure (*P*), and temperature (*T*).

In this study, the *NVE* ensemble is used for timestep testing and data extraction on phonon properties such as lattice thermal conductivity and phonon density of states. The *NPT* ensemble is preferred for accurately simulating systems at various temperatures as the volume change always occurs at different temperatures. However, the *NVT* ensemble is employed to investigate temperature effects, particularly in cases where the *NPT* ensemble is not applicable.

(c) Boundary Condition

In MD simulations, two common boundary conditions are utilized: periodic boundary and non-periodic boundary conditions [53]. The periodic boundary condition is particularly advantageous for simulating bulk materials as it allows macroscopic properties to be calculated from a fewer number of atoms. Under this condition, the primary cell is replicated in all dimensions, ensuring identical system size, shape, and atom positions across primary and image cells. Atoms within the primary cell can interact with those in neighboring images if they fall within the interaction cutoff distance. When atoms migrate across the boundary, they reenter the simulation box from the opposite side. Despite its suitability for bulk material simulation, a size test on the primary cell remains essential to ensure the convergence of calculated results.

The non-periodic boundary condition is typically utilized for simulating nanomaterials, restricting interactions to within the primary cell and preventing atom migration across boundaries. However, the boundary can move with the atoms if not fixed, allowing atoms to travel distances larger than the original cell size. The boundary can expand or shrink accordingly with atom movement. Nevertheless, employing non-periodic boundary may significantly alter the chemistry of the simulated system due to the creation of free surfaces and sharp corners with dangling bonds. Caution is advised to ensure accurate representation of basic physics when using non-periodic boundary conditions. Additionally, it is important to note that pressure control via barostat cannot be implemented under this non-periodic condition.

(d) Timestep

While conducting MD simulations, the timestep plays a critical role in balancing simulation efficiency with numerical accuracy. To extend simulation durations while conserving computational resources, larger timesteps are preferred. However, increasing the timestep size can lead to instability in integration algorithms like the Verlet method, primarily due to significant truncation errors during the integration process. This instability causes a rapid increase in the system's total energy, compromising simulation accuracy. Therefore, the choice of timestep significantly influences the numerical fidelity of CMD simulations.

Typically, timesteps ranging between 0.5 and 2 femtoseconds are selected [67]. This range is justified by ensuring that the timestep duration is comparable to the period of the highest vibrational frequency exhibited by molecules or atoms within the system.

To strike a balance between computational efficiency and accuracy, it is imperative to rigorously test different timestep sizes within the NVE ensemble prior to initiating simulations. This pre-simulation testing phase ensures that the chosen timestep effectively captures system dynamics while maximizing computational efficiency

***Ab Initio* Molecular Dynamics:**

Ab initio Molecular Dynamics (AIMD) is a computational method used in the field of theoretical materials science to simulate the dynamical behavior of atoms based on quantum mechanical principles without any empirical interatomic potential parameters. AIMD involves dynamically computing the quantum-mechanical potential energy of nuclei in a system via real-time electronic structure calculations as the molecular dynamics trajectory evolves. These electronic structure calculations provide the forces acting on atoms, which are then used to update the atomic positions and velocity in time using classical Newtonian dynamics. AIMD simulations can provide detailed insights into the structural and dynamical properties of molecules and materials, making it a valuable tool for studying chemical reactions, phase transitions, and material properties at the atomic level.

The Newtonian equation of motion can be expressed for the nuclei as:

$$M_I \left\{ \ddot{\boldsymbol{R}}_I \right\} = -\nabla_I \left[\varepsilon_0 \left(\left\{ \boldsymbol{R}_I \right\} \right) + V_{NN} \left(\left\{ \boldsymbol{R}_I \right\} \right) \right], \tag{1.9}$$

where $V_{NN}\left(\left\{\boldsymbol{R}_I\right\}\right)$ represents the coulombic interactions between the nuclei and $\varepsilon_0\left(\left\{\boldsymbol{R}_I\right\}\right)$ represents the relevant ground-state energy eigenvalue corresponding to the nuclear configuration at $\boldsymbol{R}_I$. Two frequently employed methods for computing the energy terms described in Eq. (1.9) are the Born-Oppenheimer dynamics [68] and the Car-Parrinello dynamics [69]. In Born-Oppenheimer dynamics, the energy is determined by minimizing the Kohn-Sham energy functional with respect to the nuclear configuration at each time step. In contrast, Car-Parrinello dynamics employ the Car-Parrinello extended Lagrangian approach to calculate energy. Subsequently, Eq. (1.9) can be solved directly via numerical integration utilizing a symplectic integrator, such as the Verlet algorithm.

1.3.3 Monte Carlo Simulations

Monte Carlo (MC) simulation, a stochastic numerical method involving random sampling, is commonly used for problems that are challenging to solve deterministically, even when the problem itself may be theoretically deterministic. MC simulation, particularly Markov Chain

Monte Carlo (MCMC) simulation is widely used in physics research for stochastically handling system evolution on a macroscopic scale by sampling likely states and configurations to calculate averages of observables.

The MCMC method relies on the concept of a Markov Chain, where the probability of the state at each step is dependent solely on the state of the previous step.

$$p\left(x_n | x_{n-1},.....,x_1\right) = p\left(x_n | x_{n-1}\right), \tag{1.10}$$

The transition probability from state *i* to state *j* is represented as $W_{ij} = p\left(x_j \mid x_i\right)$ and when the system is in equilibrium:

$$p_i = \sum_j W_{ij} p_j \tag{1.11}$$

The detailed balance condition ensures equilibrium in a Markov Chain by stating that the transition probability from state *i* to state *j* must equal that from state *j* to state *i* for any pair of states,

$$W_{ji} p_i = W_{ij} p_j \tag{1.12}$$

The Metropolis method determines the transition probability from state *i* to state j as [70]:

$$W_{ji} = T_{ji} A_{ji}, \tag{1.13}$$

where T_{ji} represents the attempt probability from state *i* to *j*, and A_{ji} represents the acceptance probability for the transition. It is beneficial to have $T_{ij} = T_{ji}$. To establish a probability distribution ***p***, if $p_j > p_i$, set $W_{ji} = T_{ji}$, otherwise $W_{ji} = T_{ji}\left(p_j / p_i\right)$.

The Metropolis method follows this algorithm [70]:

1. Compute the ratio $r = p\left(x_j\right) / p\left(x_i\right)$; if *r* is greater than 1, accept the transition and set x_{i+1} to x_j.

2. If r is less than 1, generate a random number t between 0 and 1. Accept the transition if t is less than r, setting x_{i+1} to x_j. Otherwise, keep x_{i+1} as x_i.

To simulate the canonical ensemble, the probability of a specific microstate must follow the distribution $p \propto \exp\left(-\frac{1}{k_B T} H\right)$. The acceptance probability for the next state is calculated as

$$p_a = \min\left(1, \exp\left(-\frac{1}{k_B T}\left(U_t - U_n\right)\right)\right), \tag{1.14}$$

Where k_B is the Boltzmann constant, U_t is the energy of the proposed state and U_n is the energy of the current state. This method ensures convergence to the system's true stable distribution [71].

One of the major limitations in MD simulation for solid-state is the low diffusion of atoms due to high energy barriers, causing atoms to stay near lattice sites and vibrate with temperature changes. This imposes a limitation on reaching solid-state equilibrium and potential short-range ordering. To address this, hybrid MD/MC simulation is developed, where MD simulation is utilized for small atomic movements and MC atomic swaps to reach equilibrium and observe short-range ordering. MC's acceptance of energy-favorable swaps aids in achieving solid-state equilibrium, crucial for HEA analysis.

1.3.4 Boltzmann Transport Theory Calculations

The Boltzmann theory is an effective method to enhance our understanding regarding the transport properties of materials [72-74]. This method treats conduction electrons in a semiclassical manner, meaning the movement of electrons with band index $\boldsymbol{n}$ can be modeled by a wave packet centered at a position $\boldsymbol{r}$ with wavevector $\boldsymbol{k}$. The electric current, j, under an electric field, a magnetic field, and a thermal gradient, can be defined as:

$$j_i = \sigma_{ij} E_j + \sigma_{ijk} E_j B_k + \nu_{ij} \nabla_j T + \cdots, \tag{1.15}$$

where E_j represents the electric field, B_k represents the magnetic field, ∇T represents the thermal gradient, and σ represents the conductivity. The conductivity tensors can be obtained as

$$\sigma_{\alpha\beta}\left(i,\boldsymbol{k}\right)=e^{2}\tau_{i,\boldsymbol{k}}v_{\alpha}\left(i,\boldsymbol{k}\right)v_{\beta}\left(i,\boldsymbol{k}\right), \tag{1.16}$$

where $v_{\alpha}\left(i,\boldsymbol{k}\right)=\frac{\partial\varepsilon_{i,k}}{\hbar\partial k_{\alpha}}$, represents the group velocity, and τ is the relaxation time.

The relaxation time τ can vary with the band index and $\boldsymbol{k}$ vector direction. However, studies show it is largely direction-independent. Therefore, this work assumes a constant relaxation time, τ, which is widely adopted in several research [75-77].

Moreover, the conductivity tensors can be defined in terms of energy:

$$\sigma_{\alpha\beta}\left(\varepsilon\right)=\frac{1}{N}\sum\nolimits_{i,\boldsymbol{k}}\sigma_{\alpha,\beta}\left(i,\boldsymbol{k}\right)\frac{\delta\left(\varepsilon-\varepsilon_{i,\boldsymbol{k}}\right)}{d\varepsilon}, \tag{1.16}$$

where N is the number of the sampled $\boldsymbol{k}$-points. Transport distributions and density of states will be assessed using fast Fourier transforms. Subsequently, the transport tensors are derived from the conductivity distributions.

1.3.5 Modern Data Analytics:

Modern data analytics, encompassing both conventional machine learning and cutting-edge deep learning techniques, are fundamentally transforming computer simulations and the field of material science. Machine learning enables capturing intricate patterns and can be optimized systematically through data-driven learning. Its effectiveness is further enhanced by accessible computing resources, streamlined algorithms, and vast datasets from experiments or computations, rendering ML a promising solution for addressing challenges in theoretical modeling of HEAs.

ML models compute much faster than conventional atomistic and quantum simulations, thus allowing simulation of materials with millions of atoms, surpassing conventional computational limits [78-80]. This ability is crucial for comprehending the exceptional mechanical attributes of HEAs, which arise from complex ordering, defects, and microstructures [81]. Moreover, ML

serves as an effective means to construct predictive models for material properties. By analyzing data, ML identifies key features, which are crucial for obtaining desired physical properties. These intricate, nonlinear relationships between structure and properties are difficult to identify through human observation. Identifying them enables researchers to explore the vast design possibilities of HEAs more effectively. These advantages outlined above have introduced a novel data-centric approach to HEA research, exemplified by its achievements in atomistic simulations, physical property prediction, and materials design [82-84]. Selection of the appropriate ML algorithm is crucial, considering its strengths and weaknesses in relation to the task objective and dataset size.

1.4 Research Overview

The overarching goal of this research is to elucidate the intricate relationship among the element concentration, atomic structure, and physical properties of the Cantor AlCoCrFeNi HEAs by conducting an extensive assessment, with the aim of enhancing understanding regarding the influence of various structural parameters on HEA properties. To achieve this goal, effective control of composition (i.e., element concentration, element size and mass mismatch) and structure (i.e., chemical short-range ordering) are employed, as depicted in Fig. 1.3. Various computational modeling and data analysis techniques, such as molecular dynamics simulations, hybrid molecular dynamics/Monte Carlo, first-principles calculations, and machine learning, are utilized to conduct this study.

Since non-uniform mass distribution and the inclusion of differently sized elements in $Al_xCoCrFeNi$ HEAs can affect phonon and electron transport, understanding the element concentration effect on these transport behaviors are very crucial for enhancing thermoelectric efficiency. However, element concentration control for tuning the thermoelectric properties of HEAs remains a significant challenge due to the numerous complexities involved, including disorder, high compositional entropy, and mismatches in mass and interactions [85]. Therefore, a novel combination of computational approaches is adopted in this study to investigate the various Al concentration effects on the thermoelectric efficiency of $Al_xCoCrFeNi$ ($0 \leq x_{Al} \leq 2$)

HEAs over a wide range of temperatures. Calculations of phonon transport, such as phonon density of states and lattice thermal conductivity, for this HEA were carried out via classical molecular dynamics (MD) simulations. Fundamental properties of electrons, such as electronic-band structures and spectrum, are evaluated using first-principles calculations, i.e., density functional theory calculations. Then, using the fundamental properties and the semi-classical Boltzmann transport theory calculations, electron transport and conversion properties, e.g., electronic thermal conductivity, Seebeck coefficient, and electrical conductivity, can be calculated. Integrating these calculations from diverse simulation methods, the thermoelectric efficiency of $Al_xCoCrFeNi$ HEAs is assessed, which is elaborated further in Chapter 2.

In addition, structural configurations, such as local atomic order, can play a significant role in determining physical properties of the HEAs [25, 26, 37]. Short-range ordering (SRO) in a HEA can affect the system energetics, phase formation, enthalpy, and so on [25, 26, 37, 38]. Thus, characterizing short-range order in $Al_xCoCrFeNi$ HEA is crucial to obtain optimal properties. However, experimental evaluation of SROs in HEAs is extremely difficult due to compositional complexities. Here, SRO values in HEAs are characterized by Warren-Cowley parameters [86] and calculated from hybrid molecular dynamics/Monte Carlo (MD/MC) simulations. Then, the SRO effect on the thermodynamic properties, i.e., lattice thermal conductivity, thermal expansion coefficient, and bulk modulus are investigated via molecular dynamics simulations and density functional theory calculations. This research is thoroughly discussed in Chapter 3.

Furthermore, due to the vast compositional space inherent in HEAs, it is extremely difficult to analyze all HEAs via traditional simulations or experimental means. Modern data analytic technologies including various machine learning algorithms have been developed and their applications are expected to contribute to overcoming the challenge. The strength of HEAs is critical to many real-world applications and a combination of proper concentration percentages of all the constituting elements is necessary to obtain high-strength HEAs. Therefore, alloying concentration and SRO effect on the mechanical strength of AlCoCrFeNi HEA families, i.e., yield strength is evaluated via molecular dynamics simulations and modern data analytics. Detailed discussions of this research are provided in Chapter 4.

Through this PhD study, understanding the role of aluminum content, local atomic order, and alloying concentrations on the thermoelectric, thermodynamic, and mechanical properties under various conditions are expected to be enhanced.

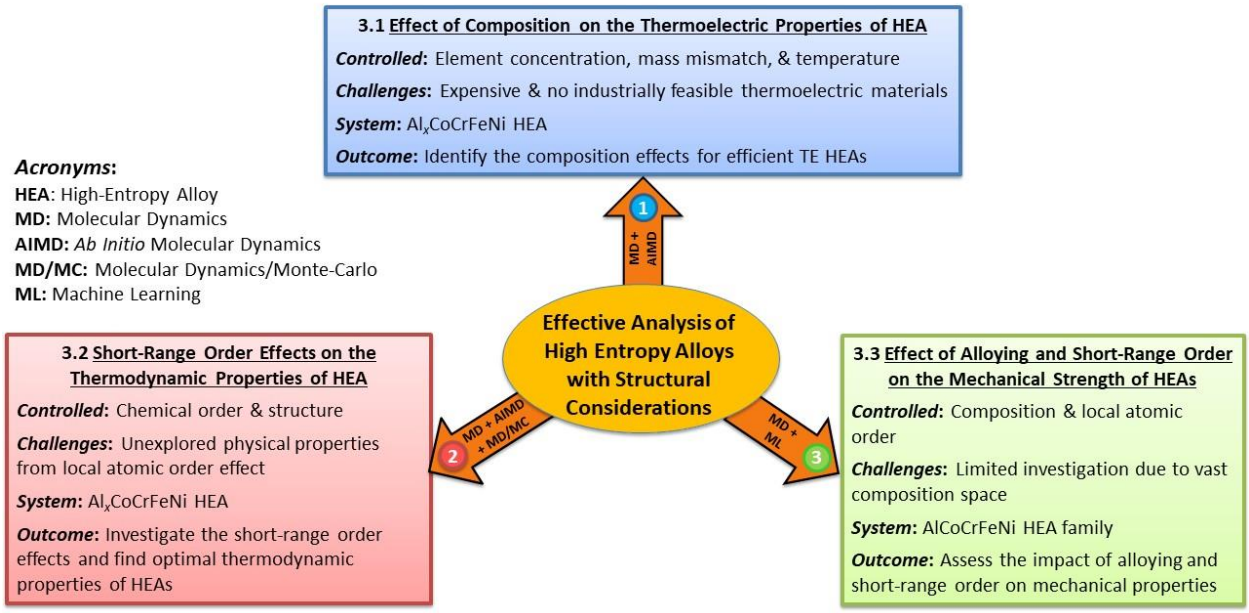

Figure 1.3: Overview of the accomplished research tasks in this dissertation, encompassing controlled variables, challenges, and outcomes.

This study will contribute to the knowledge of tuning composition and structure to control the specific physical properties of the HEAs, facilitating the design of tailored HEAs for targeted industrial applications. The knowledge from this research can be translated to other HEA systems while serving as a blueprint for experimentalists, guiding the design of thermally and mechanically efficient HEAs.

Chapter 2

Effects of Aluminum Content on Thermoelectric Performance of $Al_xCoCrFeNi$ High-Entropy Alloys

2.1 Abstract

Introducing a non-regular distribution in the mass and bonding by including distinctly different elements can reduce the phonon transport even within structurally well-ordered materials. These distributions are a quality of all high-entropy alloys (HEAs), however the inclusion of aluminum in $Al_xCoCrFeNi$ is particularly impactful due to the large mismatch in atomic mass with other components. The resultant low phonon conductivity is a requirement for high thermoelectric performance, motivating the investigation of the effects of Al content on phonon transport as well as other thermoelectric properties. This work examines the phonon and electron transport and thermoelectric conversion properties with various Al contents ($0 \leq x_{Al} \leq 2$) in this Cantor alloy using first-principles calculations, molecular dynamics, and semi-classical Boltzmann transport theory. The calculated phonon density of states and thermoelectric properties present reasonable agreements with experiments, including neutron scattering. A large reduction of phonon conductivity (k_L) is observed even with low x_{Al}s, which we attribute to effective phonon scatterings by the large mass mismatch. However, its temperature dependence is not significant, demonstrating a minor contribution of interphonon scattering. In contrast, electrical conductivity (σ) and Seebeck coefficient (S) increase with temperature at higher x_{Al}s with body-centered cubic structures. Therefore, the thermoelectric figure of merit (ZT) of $Al_xCoCrFeNi$ HEAs is enhanced by increasing the Al content mainly due to the increase of the thermoelectric power factor (σS^2) at high temperatures, while at low temperatures the phonon-scattering enhancement by mass mismatch is also important.

2.2 Disclosure

Chapter 2 is a modification of the published work: **Md Abdullah Al Hasan,** Jiaqi Wang, Seungha Shin*, Dustin A. Gilbert, Peter K. Liaw, Nan Tang, W.L. Namila C. Liyanage, Louis Santodonato, Lisa DeBeer-Schmitt, Nicholas P. Butch, "Effects of aluminum content on thermoelectric performance of AlxCoCrFeNi high-entropy alloys", Journal of Alloys and Compounds, 883, 160811 (2021). This publication is reprinted with permission from Elsevier.

The dissertation author listed in this publication directed and supervised the research which forms the basis for this publication.

2.3 Introduction

Thermoelectric materials have attracted enormous attention over the past decades due to their potential applications in the recovery of waste heat, providing cleaner energy and reducing greenhouse gas emissions [87-91]. Generally, the energy conversion efficiency in thermoelectric materials is determined by the figure of merit [92], $ZT = S^2\sigma T/(k_e + k_L)$, where S is the Seebeck coefficient, σ the electrical conductivity, k_e the electronic thermal conductivity, k_L the lattice thermal conductivity, and T the temperature; the higher ZT, the more efficient thermoelectric energy conversion [92, 93]. Therefore, suppressing thermal conductivity, while maximizing Seebeck coefficient and electrical conductivity, leads to a high figure of merit (ZT). However, the interdependence of these properties imposes a challenge on identifying efficient thermoelectric materials. Specifically, as the electron contribution to thermal transport dominates over phonon or atomic vibration in metallic materials, higher σ causes higher k. Semi-metals and semi-conductors have been broadly demonstrated as thermoelectrics, and high ZT values of Bi_2Te_3, PbTe, and $(Bi_{1-x}Sb_x)_2(Se_{1-y}Te_y)_3$ (based on *p*-block elements) have been reported [85]. However, these materials contain toxic or scarce elements, which are not suitable for scalable production, and quickly degrade at high temperatures (T > 800°C) [85, 93, 94]. Although half-Heusler type materials show high enough ZT (≈ 1) values at high temperatures that can compete with the state-of-the-art *n*-type SiGe compounds, they include expensive metals, such as Hf or Pd (i.e., corresponds to 90% of the total material cost), which hampers their commercial use [85, 95, 96]. Furthermore, some half-Heusler compounds are effective only at low Ts (< 650 K) [97].

High-entropy alloys (HEAs) have been regarded as novel types of alloys because of their unique microstructures and adjustable properties [8, 17, 41, 98]. In HEAs, five or more elements are mixed with equimolar or near-equimolar atomic fractions, each ranging from 5 to 35 atomic percent (at.%) [11]. Thus, the high configurational entropy of mixing, especially at elevated

temperatures, can thermodynamically stabilize solid solution alloys, and their complex phase space enables exceptional properties, including mechanical properties [36, 41, 98]. A recent study on HEAs reveals their promising features for high-T thermoelectric applications [85]. In HEAs, complexity through severe lattice distortions, point defects, and the precipitation of secondary phases enhance the phonon scattering, reducing lattice thermal conductivity, while maintaining a high mobility of the conduction electrons [85]. Furthermore, the high symmetry of crystal structures, such as body-centered-cubic (BCC) and face-centered-cubic (FCC) phases, in HEAs allows for a high convergence of the bands that are close to the Fermi level to obtain a high Seebeck coefficient [99]. However, due to the involvement of many complexities (i.e., disorder, high compositional entropy, mass and interaction mismatches) in HEAs, tuning of the thermoelectric properties remains a great challenge [85]. Therefore, a comprehensive study is required for the reduction of thermal conductivity and enhancement of desirable properties, i.e., Seebeck coefficient and electrical conductivity.

Different from other HEAs composed of elements with similar atomic mass, the Al in $Al_xCoCrFeNi$ has an atomic mass (m_{Al} = 26.98 g/mole) which is 52% smaller than the average mass of other elements ($m_{avg,others}$ = 56.37 g/mole) while the other elements have atomic masses within 8% of this average. This large distribution of atomic mass causes a significant increase of phonon scattering, reducing the lattice thermal conductivity. Thus, we can expect that more enhanced thermoelectric performance (or higher ZT) can be achieved via effective thermal transport control by the Al content (x_{Al}) in $Al_xCoCrFeNi$ HEAs. However, the Al content also influences other properties of $Al_xCoCrFeNi$, including the crystal structure, mechanical, electrical, magnetic, anticorrosive, and thermodynamic properties [45-47, 100, 101]. Therefore, the study of $Al_xCoCrFeNi$ for thermoelectric performance requires comprehensive understanding of the Al content effects on various properties that contribute to thermoelectric efficiency. Only a few experimental studies have been performed on the thermoelectric properties of $Al_xCoCrFeNi$; for example, Shafeie et al. [85] reported electrical conductivity (σ), Seebeck coefficient (S), thermal conductivity (k), power factor (σS^2), and figure of merit (ZT) for $0 \leq x_{Al} \leq 3$ in the

temperature range of 100-900°C. However, to our best knowledge, comprehensive computational study has not been found yet.

Through effective parametric control, computational approaches can facilitate the identification of effects of a specific control parameter on material properties. For multi-component alloy systems, several computational studies have been successfully performed to investigate the effects of element concentration. For example, first-principles calculations have been employed to study the effect of Mn and Al contents on the elastic properties, structural stability, and magnetic properties of FeCoNi-based alloys [102], BCC $Al_xHf_{1-x}NbTaTiZr$ [103], and $Al_xCrMnFeCoNi$ HEAs [104]. This research aims to identify the effects of Al content on thermoelectric performance of $Al_xCoCreFeNi$ HEAs ($0 \leq x_{Al} \leq 2$), the lattice thermal conductivity (k_L), electronic transport (σ and k_e), thermoelectric conversion coefficient (S), etc. over a wide temperature range (300 – 1,200 K) using molecular dynamics (MD), density functional theory (DFT), and the Boltzmann transport theory. Simulation results are compared with the experimentally measured phonon density of states.

2.4 Methodology

The atomic structures of the examined $Al_xCoCrFeNi$ HEAs present stable crystalline orders over the temperature range of 300 – 1,200 K. Previous experimental works have shown that the stable phase of the HEAs changes from FCC to BCC structures as the Al content (x_{Al}) increases [45, 47, 105]. In the current research, the crystalline structure and the lattice constant were determined by a minimum energy calculation in MD and DFT. In these models, the initial structures were created via random and uniform distribution of the constituent elements (Al, Co, Cr, Fe, and Ni) in the simulation space according to the corresponding Al concentration of each HEA, as shown in Fig. 2.1a [106]. Nine Al concentrations were modeled, which results in the atomic number ratio Al:Co:Cr:Fe:Ni of x_{Al}:1:1:1:1, where x_{Al} = 0, 0.3, 0.5, 0.75, 0.875, 1, 1.25, 1.5, and 2.

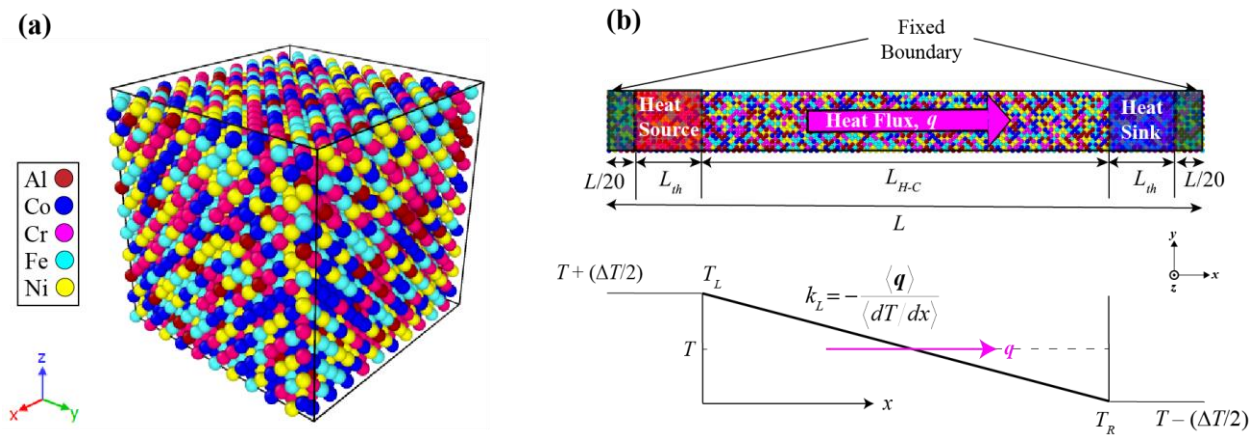

Figure 2.1: (a) 10 × 10 × 10 supercell for energy and phonon spectrum analysis via classical MD simulations, and (b) non-equilibrium MD simulation setup for the lattice thermal conductivity calculation with a 100 × 10 × 10 supercell.

Among the properties for thermoelectric performance, the phonon contribution to thermal transport in $Al_xCoCrFeNi$ was investigated, using classical MD simulations. A phonon spectrum (density of states, D_p) was also calculated to validate the MD simulations by comparing with experimental values and to understand the change in phonon transport. In the classical MD simulations, the interactions in the Al-Cr-Co-Fe-Ni elements were calculated employing the embedded atom model (EAM) potential [107, 108]. The EAM potentials have been widely employed to simulate various metallic processes in atomic scale and found successful in capturing many-body effects of metallic bonding [107-110]. Newton's equations of motion were integrated using the Verlet algorithm [63] with a time-step of 0.5 fs. Modeling was repeated with at-least five different initial structures for each Al concentration to verify the lattice-constant and crystal-order determinations. To examine the mass-mismatch effect on the phonon properties (i.e., the phonon density of state and lattice thermal conductivity) of the HEAs, a second series of simulations were performed, which assigned the mass of Al to match the average of the other elements, 56.367 g/mole. An energy minimization using the conjugate gradient (CG) algorithm [111] with a force and energy precision of 1.0×10^{-10} eV/Å was applied to the initial structures. Comparing the respective energy values of FCC and BCC cases, the crystal order of the lower energy value was determined for each Al concentration.

Phonon density of states (D_p) is calculated using the Fourier transform of the velocity autocorrelation function from the MD simulations [112]. The velocity data for the D_p calculations were obtained from simulations with $10 \times 10 \times 10$ supercells of an FCC or BCC lattice containing 4,000 or 2,000 of randomly distributed Al, Co, Cu, Fe, and Ni atoms. A canonical ensemble (*NVT*; constant number of atoms, volume, and temperature) with Nosé thermostats was employed, and the last 50 ps of simulation data were used for the velocity autocorrelation.

To validate the calculated D_p from MD, we also measured D_p via neutron scattering experiments. Polycrystalline ingots of the proposed HEA compositions were prepared by arc melting and subsequent annealing as described previously [101], and a 1 cm diameter ×1 cm tall cylinder was

cut from the ingot. The D_p of the prepared sample was measured on the Disc-Chopper Spectrometer (DCS) at the National Institute for Standards and Technology. Measurements were performed by heating the sample to 500 K in vacuum then illuminating it with 2.5 Å wavelength neutrons; using a time-of-flight scheme the change in the kinetic energy of the neutron after scattering is determined. Since the samples are polycrystalline, the diffraction pattern from the scattering appears as a ring, which is integrated to resolve scattering intensity versus momentum transfer vector (q) and the change in the neutron energy. The one-dimensional generalized density of states is generated by integrating the scattering intensity across all q; the scattering intensity is corrected for the Fresnel decay and a Boltzmann factor representing an activation probability. Results were analyzed using the DAVE software package [113].

The lattice thermal conductivity of $Al_xCoCrFeNi$ HEAs (k_L) is examined by analyzing the heat flow and temperature distributions generated by a non-equilibrium temperature setup in MD. 100 × 10 × 10 supercells (40,000 atoms for FCC and 20,000 atoms for BCC structures) are created for the nonequilibrium MD simulations. A non-periodic and fixed boundary condition is applied to the x direction, while periodic boundary conditions are to the y and z directions. To achieve fixed boundary conditions in the transport direction (x-direction), we fixed a few layers of atoms at both ends of the HEA length ([0, L/20]gt and [19L/20, L], where total length, $L = 100a$, and a is the lattice constant), as shown in Fig. 2.1b. Then, next to both fixed layers, hot (heat source, T_L) and cold (heat sink, T_R) thermostats are applied within a length of $L_{th} = L/10$ (red and blue shades in Fig. 2.1b, respectively). The system length ($L_{H\text{-}C}$) is defined by the distance between two thermostats. To calculate thermal conductivity at T, ($T + \Delta T/2$) and ($T - \Delta T/2$) are prescribed to the hot and cold thermostat regions, and $\Delta T = 100$ K was employed over the examined temperature range to observe a clear temperature gradient. For the calculation of a heat flux ($\boldsymbol{q}$, W/m^2) and temperature gradient (∇T, K/m), we employed 5 ns of simulation data, which ensure small enough fluctuations in the calculation. Then, the lattice thermal conductivity is calculated, using Fourier's law ($k_L = -\boldsymbol{q}/\nabla T$) [114].

The electronic-band structures of Al$_x$CoCrFeNi for thermoelectric properties involving electrons (e.g., k_e, σ_e, and S) are obtained from first-principles calculations, employing DFT. All the DFT simulations in the current research were performed, using the Vienna *ab* simulation package (VASP) [115] with the projector augmented wave (PAW) potentials [116]. The electronic exchange-correlation interaction was treated by the Perdew-Burke-Ernzerhof (PBE) functional with the generalized gradient approximation (GGA) [117]. The Methfessel-Paxton technique [118] was adopted with a smearing parameter of 0.2 eV. The plane-wave energy cutoff was set to 400 eV, and the electronic-energy convergence criterion to 10^{-4} eV. A 2×2×2 Γ-centered *k*-point mesh, which leads to 8 $\boldsymbol{\kappa}$-points, was used to conduct the integration over the Brillouin zone. For a wide temperature range of 300-1,200 K, we employed molecular dynamics, using the force field from DFT calculations, i.e., *ab initio* MD (AIMD). 3 × 3 × 3 FCC (108 atoms) and 4 × 4 × 4 BCC (128 atoms) supercells were created for AIMD. Using a canonical ensemble, *NVT* (i.e., constant number of atoms, volume, and temperature) with temperature control by the Nosé thermostats [119], the atomic position and velocity data were updated with a single time step of 0.5 fs, and 4,000 time step data were used for the analysis.

The AIMD results were then processed to evaluate the thermoelectric properties for Al$_x$CoCrFeNi ($0 \le x_{\mathrm{Al}} \le 2$), using the Boltzmann transport theory. The transport coefficients, i.e., electrical conductivity (σ), Seebeck coefficient (S), and electronic thermal conductivity (k_e) tensors, can be calculated as a function of the temperature (T) and chemical potential (μ) by integrating the transport distribution function ($\bar{\sigma}_{\alpha\beta}$) [75, 87, 120]:

$$\sigma_{\alpha\beta}(T,\mu) = \frac{1}{\Omega}\int \bar{\sigma}_{\alpha\beta}(E)\left[-\frac{\partial f_{\mathrm{FD}}(T,E,\mu)}{\partial E}\right]dE, \tag{2.1}$$

$$S_{\alpha\beta}(T,\mu) = \frac{1}{e_c T\Omega\sigma_{\alpha\beta}(T,\mu)}\int (E-\mu)\,\bar{\sigma}_{\alpha\beta}(E)\left[-\frac{\partial f_0(T,E,\mu)}{\partial E}\right]dE, \text{ and} \tag{2.2}$$

$$k_{e,\alpha\beta}(T,\mu) = \frac{1}{{e_c}^2 T}\int (E-\mu)^2\,\bar{\sigma}_{\alpha\beta}(E)\left[-\frac{\partial f_0(T,E,\mu)}{\partial E}\right]dE\ , \tag{2.3}$$

where Ω, f_{FD}, and e_c are the unit cell volume, the carrier Fermi-Dirac distribution function, and the electron charge, respectively. α and β are tensor indices, and the transport distribution function is defined as

$$\bar{\sigma}_{\alpha\beta}\left(E\right)=\frac{e_c^{\,2}}{N}\sum_{i,\boldsymbol{\kappa}}\tau u_{\alpha}\left(i,\boldsymbol{\kappa}\right)u_{\beta}\left(i,\boldsymbol{\kappa}\right)\frac{\delta\left(E-E_{i,\boldsymbol{k}}\right)}{\delta\left(E\right)}, \tag{2.4}$$

where $u_{\alpha}(i, \boldsymbol{\kappa})$ is the α-th component of the group velocity, $\boldsymbol{u}(i, \boldsymbol{\kappa})$, of carriers, N is the number of sampled $\boldsymbol{\kappa}$ points, i is the band index, and $\boldsymbol{\kappa}$ is the wave vector. The group velocity can be derived from the band structure by:

$$\boldsymbol{u}\left(i,\boldsymbol{\kappa}\right)=\frac{1}{\hbar}\nabla_{\boldsymbol{\kappa}}E_{i,\boldsymbol{\kappa}}, \tag{2.5}$$

where $\hbar$ is the reduced Planck constant.

Here, we fit the band structure data into the semi-classical Boltzmann transport theory, which is carried out via the BoltzTraP package [75]. Then, the thermoelectric properties of the HEAs are calculated, using Eqs. 2.1-2.5, based on their band structures. In the calculations of transport, the distribution function, the carrier relaxation time, τ, is a required input. For simplicity, we approximated its value to a constant (single relaxation time approximation or SRTA), using the experimental data for these HEAs that are available in the literature [85, 100]. Then, the transport properties (i.e., electrical conductivity, electronic thermal conductivity, etc.) are calculated with respect to the relaxation time. On the other hand, the Seebeck coefficient is independent of τ, assuming isotropic relaxation [75] and can be directly obtained using only the band-structure information. This approach has been adopted by several researchers previously and successfully employed to evaluate electrical transport properties of thermoelectric compounds [121, 122].

2.5 Results and Discussion

Prior to classical MD simulations for the phonon transport analysis, the crystal structure and lattice parameter for each HEA were evaluated by finding a minimum-energy atomic structure. In Al_xCoCrFeNi HEAs, due to the smaller atomic mass and larger size, compared to other

constituents, the Al content plays an important role in the structural configuration [47, 123-126]. Our simulations confirm the dependence of Al content on the HEA structure, and single FCC and BCC phases are observed for $0 \leq x_{Al} \leq 0.75$ and $0.875 \leq x_{Al} \leq 2$, respectively.

The lattice constants corresponding to the minimum energy states after relaxation are used to create the initial atomic structures for further simulations. The lattice constants and phases from the simulations agree well with the experimental values [45, 47] as shown in Fig 2.2a, validating the use of classical MD modeling in this work, including the interatomic potential. In general, increasing x_{Al} results in a larger lattice constant, increasing the average atomic volume (or reducing the atomic density), and especially, a large volume expansion is observed in the FCC-BCC transition as exhibited in Fig. 2.2b. Additionally, the addition of Al atoms reduces the average atomic mass (m_{avg}), while increasing the standard deviation (m_{std}) of the atomic-mass distribution.

The simulated and experimentally measured phonon density of states (D_p) for AlCoCrFeNi are shown in Fig. 2.3a and demonstrate good agreement in their major peaks and overall shape. This agreement demonstrates that our simulation model accurately describes the phonon behavior, which also supports the calculation accuracy of the lattice thermal conductivity. We also calculated the element-specific contributions to D_p ($D_{p,i}$, where i = Al, Co, Cr, Fe, and Ni), as shown in Fig. 2.3b. These plots show that $D_{p,Al}$ tends to peak at a much higher energy, ≈ 45 meV, compared to its heavier counterparts (Co, Cr, Fe, and Ni), which share similar peak positions at ≈ 20 meV. The higher-energy peak in Al can be attributed to the light mass of the Al atoms. The reduced overlap between $D_{p,Al}$ and the other $D_{p,i}$ tends to cause scattering of the phonons, rather than long-range coherent transport; suppression of coherent phonon transport directly corresponds to poor lattice thermal conductivity. A larger x_{Al} shifts of D_p to higher phonon energy (Fig. 2.3c). However, as Fig. 2.3d shows, no shift is observed when the mass mismatch of Al is excluded, that is, setting the mass of Al to match the average mass of the other elements (56.367 g/mole). In addition, the transition to a BCC phase at larger x_{Al} causes lower D_p at low

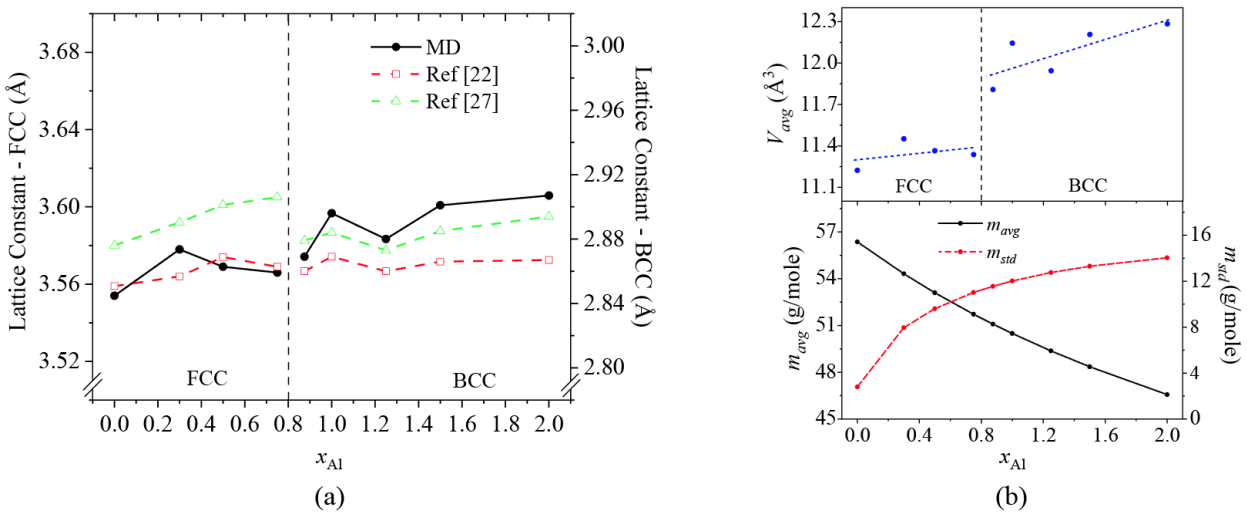

Figure 2.2: (a) Lattice constants of AlxCoCrFeNi ($0 \leq x_{Al} \leq 2$) from classical MD and experiments at room temperature (300 K) [45, 47] and (b) average atomic volume (V_{avg}), mass (m_{avg}), and standard deviation (m_{std}) of atomic mass with respect to x_{Al}.

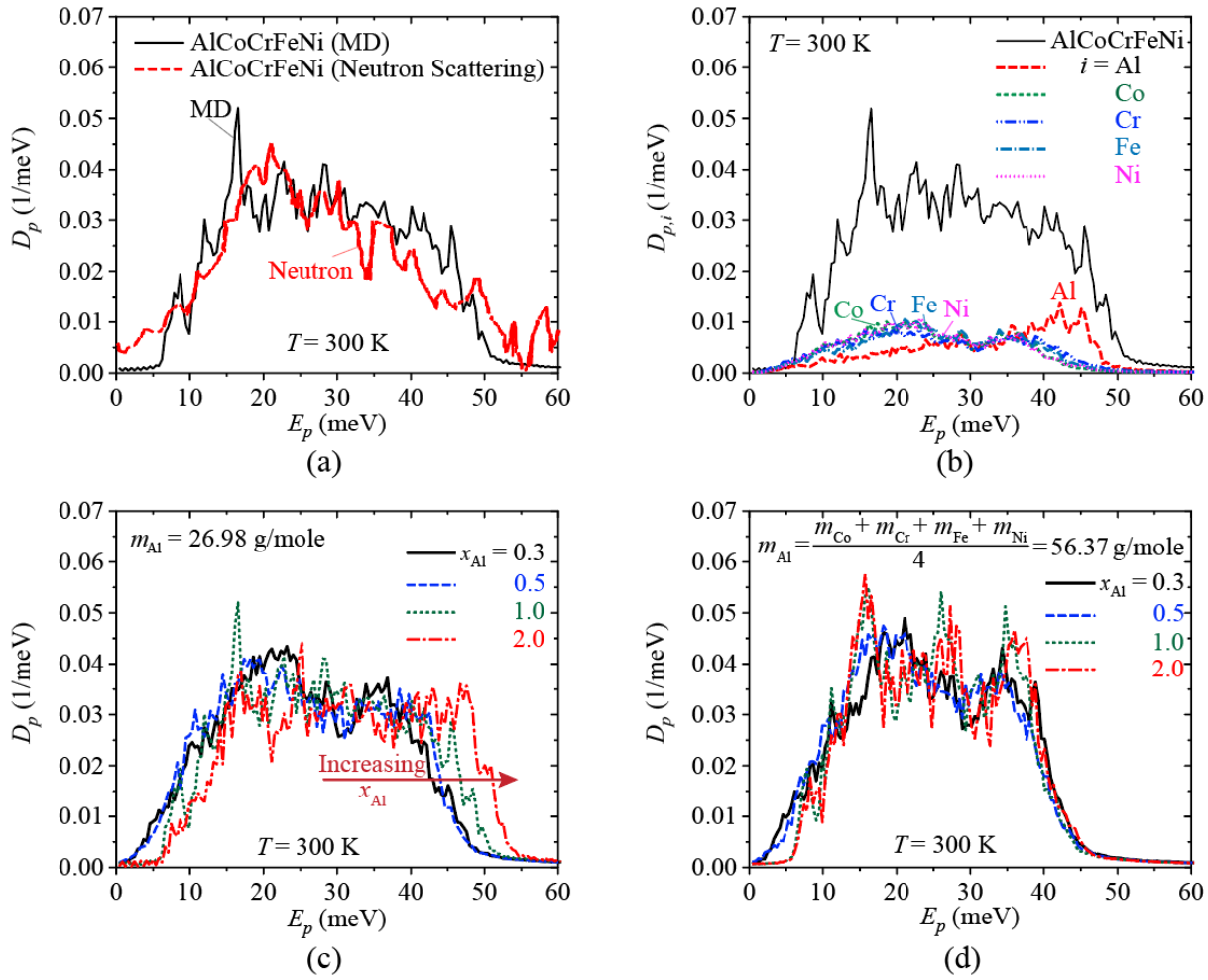

Figure 2.3: (a) Phonon density of states (D_p) of AlCoCrFeNi (x_{Al} = 1.0) with respect to the phonon energy (E_p) from MD simulation (black solid) and its comparison with neutron scattering experiment (red dashed). (b) Partial D_p of the constituent elements (Al, Co, Cr, Fe, and Ni) of the AlCoCrFeNi HEA. (c) D_ps of Al$_x$CoCrFeNi (x_{Al} = 0.3, 0.5, 1, and 2) with consideration of Al mass mismatch and (d) those without Al mass mismatch at 300 K from MD simulations.

energy, which can reduce heat capacity and possibly contribute to further reduction of the lattice thermal conductivity.

The lattice thermal conductivities (k_L) of $Al_xCoCrFeNi$ from NEMD simulations at 300 K appear in the range of 2.88-7.43 W/m-K at different Al contents ($0 \leq x_{Al} \leq 2$), as shown in Fig. 2.4a. This range is in good agreement with the experimental values of k_L for $Al_xCoCrFeNi$ [47]. Unlike other metallic materials, the phonon contribution to the thermal conductivity is comparable to the electronic contribution in the HEAs [47, 100, 127]. Therefore, the k_L control is important for the thermoelectric performance, especially at low temperatures. These calculated results in Fig. 2.4a present that small inclusions of Al initially cause a large reduction in k_L, however, with further inclusion the reduction is much less; a dramatic drop in k_L occurs at the FCC to BCC structural phase transition ($x_{Al} \sim 0.8$). Removing the mass effect, by setting the mass of the Al to 56.367 g/mole, we observe larger k_L values at all nonzero Al contents (x_{Al}), compared to the simulations employing actual Al mass (m_{Al} = 26.982 g/mole), and this difference is more significant at lower x_{Al}s. These results show the critical impact of the mass mismatch, but also implicate the role of scattering from another mechanism – lattice mismatch and a distribution in bonding strength [128].

According to the kinetic theory [129], k_L is inversely proportional to the total phonon scattering rate, which includes the scattering by Al and other scattering mechanisms (e.g., scattering by other phonons, boundaries, electrons, etc.) represented by $\dot{\gamma}_{Al}$ and $\dot{\gamma}_{others}$, respectively,

$$k_L \propto \frac{1}{\dot{\gamma}_{Al} + \dot{\gamma}_{others}}, \tag{2.6}$$

Higher x_{Al} leads to more phonon scattering, i.e., larger $\dot{\gamma}_{Al}$, by mass and lattice mismatch, thus reducing k_L. The considerable k_L reduction observed in our simulations confirms Al is an effective phonon scatterer. The modeling shows the critical impact of mass mismatch in reducing k_L, especially for small x_{Al}, and also implicates the role of other factors (lattice mismatch and a distribution in bonding strength) in increasing the scattering ($\dot{\gamma}_{Al}$). The initially rapid reduction

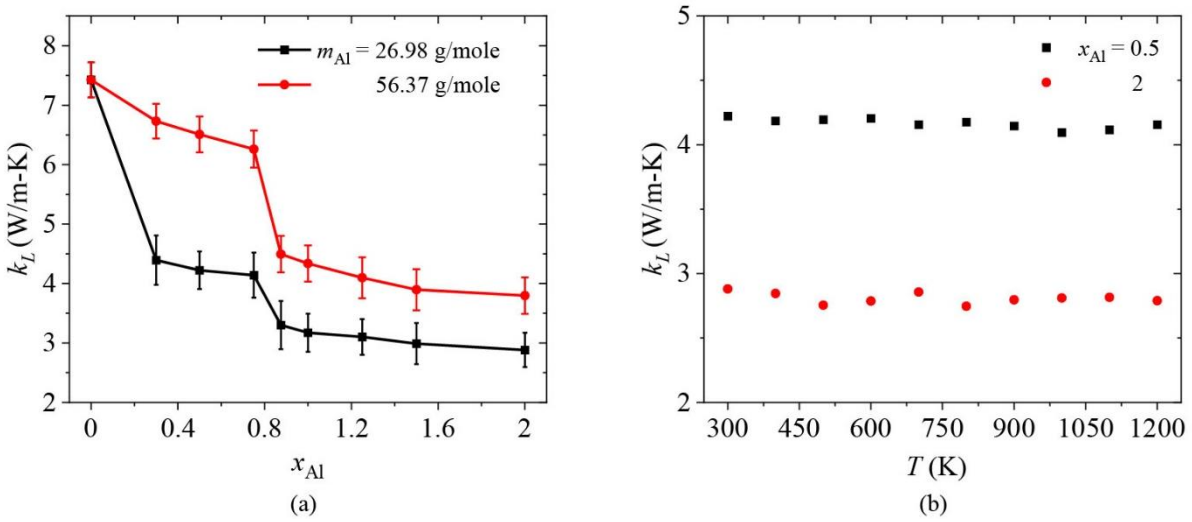

Figure 2.4: (a) Lattice thermal conductivity (k_L) with respect to the Al content (x_{Al}) calculated using non-equilibrium MD with and without consideration of Al mass mismatch. (b) Lattice thermal conductivity (k_L) with respect to temperature for FCC (x_{Al} = 0.5) and BCC (x_{Al} = 2.0) cases.

of k_L, which wanes at higher x_{Al}s, can be explained by Eq. 2.6 [128]: with the initial inclusion of Al, $\dot{\gamma}_{Al}$ quickly becomes larger than $\dot{\gamma}_{others}$ causing the initial decrease in k_L. At larger x_{Al}, the impact of adding additional Al to an already disordered system are moot, leading to an asymptotic limiting of k_L.

To investigate the possibility of phonon-phonon scattering, the k_L of two HEA cases [x_{Al} = 0.5 (FCC) and 2 (BCC)] were simulated at various T's, and showed little dependence on temperature as in Fig. 2.4b. If interphonon scattering is dominant over other scattering mechanisms, k_L would be expected to decrease with T (as observed in many crystal materials) as a higher T leads to a larger phonon population and more interphonon scatterings. Thus, this T independence demonstrates that scattering by random configurations is more significant than the phonon-phonon scattering in these HEAs.

In addition to suppressing k_L, the electronic properties (k_e, σ, and S) play a critical role in determining the thermoelectric efficiency; these properties are also affected by Al inclusion and are investigated here. The electron relaxation time (τ) for the transport coefficient of each HEA was estimated by comparing the electrical conductivity with the available experimental transport data for $Al_xCoCrFeNi$ [100] listed in Table 2.1. The calculated τ values for BCC HEAs are higher than FCC ones (i.e., more frequent electron scattering). These larger relaxation times indicate less electron scattering in the BCC structures. Therefore, better transport properties are expected at higher Al concentrations.

Using the calculated τ, electrical conductivities (σ) are obtained at different Al contents over a temperature range of 300-1,200 K, as shown in Fig. 2.5a. Electrical conductivity increases as the temperature increases in the BCC structures, while the electrical conductivity of the FCC structures decreases with the temperature. Figure 2.5b demonstrates the dependence of the Seebeck coefficient (S) of the HEAs on both temperature and Al concentration. The HEAs examined here show positive S values only at x_{Al} = 0 and negative S values for the rest of the HEAs over the temperature range, which represents that dominant charge carriers in

Table 2.1: Relaxation time approximation for AlxCoCrFeNi (0 ≤ xAl ≤ 2) with a total number of 108 atoms (FCC) and 128 atoms (BCC) at room temperature (300 K).

x_{Al}	Exp. electrical conductivity [100], σ_{exp} ($\times 10^5$ S/m)	AIMD electrical conductivity with a unity of relaxation time, σ/τ ($\times 10^{17}$ S/m-s)	Approximate relaxation time, τ (ps)
0	7.05	13.1	0.382
0.3	8.02	8.25	0.579
0.5	7.40	13.6	0.543
0.75	6.14	7.92	0.846
0.875	6.99	3.10	1.39
1	4.53	3.59	1.26
1.25	5.97	4.70	1.88
1.5	6.52	3.78	1.74
2	4.73	2.95	1.60

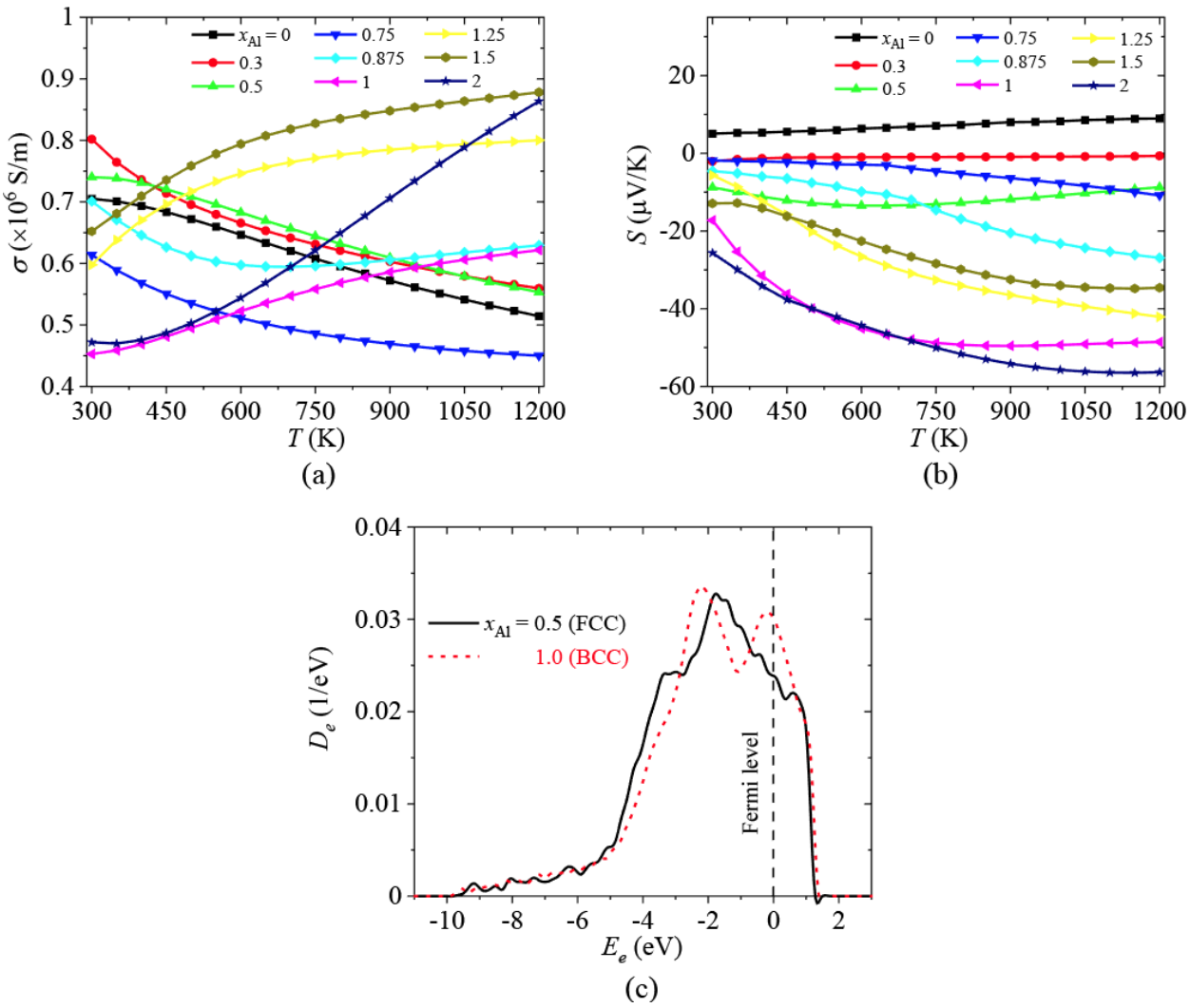

Figure 2.5: (a) Electrical conductivity and (b) Seebeck coefficients for $Al_xCoCrFeNi$ ($0 \leq x_{Al} \leq 2$) as a function of temperature, (c) Electron density of states for FCC ($x_{Al} = 0.5$) and BCC ($x_{Al} = 1.0$) structures.

$Al_xCoCrFeNi$ vary with Al concentration (holes for positive *S*, while electrons for negative *S*). Specifically, larger negative *S* values appear at high temperatures, indicating their *n*-type semiconducting nature. The absolute value of *S* increases with temperature in a BCC structure while *S* value in a FCC structure does not vary significantly. The maximum absolute *S* value (56.3 μV/K) over our calculated temperature range is found at $x_{Al} = 2.0$ at $T = 1{,}200$ K.

The different temperature dependencies of σ and *S* values in FCC and BCC HEAs can be attributed to different shapes and energy peaks in their electronic density of states from the analysis of the band structures. The larger peak of the electron density of states (D_e) near the Fermi level is found to be higher in the BCC structures, compared to the FCC structures, as illustrated in Fig. 2.5c. This peak was also observed in other literatures [130-133]. Higher D_e peaks near the Fermi level will allow more electron carriers in the BCC HEAs, increasing electrical conductivity and Seebeck values with the temperature at higher Al contents. Moreover, in both BCC and FCC HEAs, zero band gap was observed in their band structures, demonstrating the metallic characteristics, i.e., the overlapped conduction and valence bands.

The total thermal conductivity (k_{total}) values are calculated by adding the lattice thermal conductivities (k_L) and electronic thermal conductivities (k_e) from MD and AIMD simulations, respectively. The k_{total} values appear in the range from 6.77-37.6 W/m-K over the temperature range of 300-1,200 K for $Al_xCoCrFeNi$, as shown in Fig. 2.6a. The thermal conductivities present an increasing trend with temperature in both FCC and BCC phases due to the increasing k_e, which is attributed to a larger number density of electrons, different from the temperature independence of lattice thermal conductivity. Thus, the electron contribution to the overall thermal transport dominates over the phonon contribution, especially at high temperatures in the BCC $Al_xCoCrFeNi$ (Fig. 2.6b).

Power factor (σS^2) provides comprehensive electrical performance of the HEAs rather than *S* or σ alone. Figure 2.7a demonstrates that the power factor decreases or maintains constant values at lower x_{Al}s (i.e., FCC crystalline structures) with increasing temperature, while it increases with

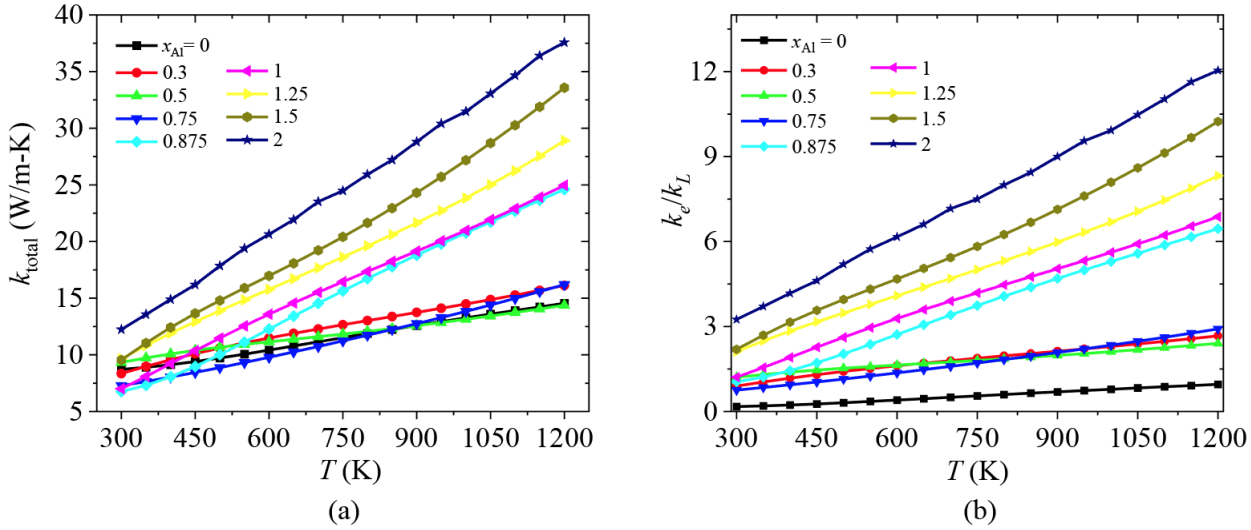

Figure 2.6: (a) Thermal conductivity ($k_{total} = k_e + k_L$) and (b) ratio of electronic and lattice thermal conductivity with respect to temperature in $Al_xCoCrFeNi$ ($0 \leq x_{Al} \leq 2$).

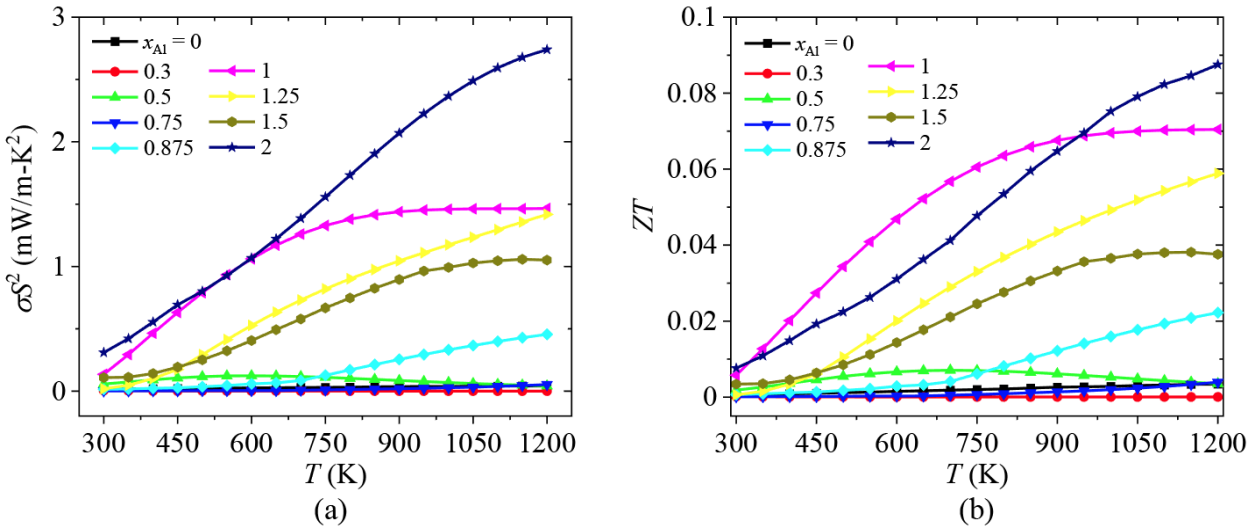

Figure 2.7: (a) Power factor (σS^2) and (b) the thermoelectric figure of merit (ZT) with respect to temperature in $Al_xCoCrFeNi$ ($0 \leq x_{Al} \leq 2$).

temperature at higher x_{Al}s with the BCC structure. The thermoelectric power factor is found at x_{Al} = 2.0 is 0.31 mW/m-K^2 at 300 K, which significantly increases with the temperature and attains the maximum value of about 2.74 mW/m-K^2 at 1,200K. A combination of larger Seebeck coefficient and higher electrical conductivity leads to a greater power factor in the BCC structures.

Figure 2.7b reveals that the temperature dependence of the figure of merit (*ZT*) is strongly affected by the Al concentration. While the *ZT* values at lower Al contents do not vary significantly with temperature, and *ZT* at higher x_{Al}s increases with *T*. The maximum *ZT* value is found for x_{Al} = 2.0 at 1,200 K, which is over 25 times higher than the *ZT* at x_{Al} = 0 at the same temperature. Although the enhanced phonon scattering by a large mass mismatch in $Al_xCoCrFeNi$ contributes to lowering the thermal transport and thus, higher thermoelectric efficiency, it is not a major factor to control thermoelectric performance, different from our initial hypothesis; the dominant factor appears to be the BCC structure. However, the results demonstrate that the significant improvement in the thermoelectricity of the HEAs can be achieved by controlling the lightweight Al content in the $Al_xCoCrFeNi$ HEAs. Furthermore, their high-temperature thermoelectric performance can make them more competitive in the search for new promising thermoelectric materials for future high-temperature applications.

2.6 Conclusions

Effects of light-weight Al content on the thermoelectric properties of $Al_xCoCrFeNi$ high-entropy alloys ($0 \leq x_{Al} \leq 2$) were investigated over a wide temperature range (300-1,200 K) using MD simulations, DFT calculations, and Boltzmann transport theory. As the Al concentration increases, the HEA phase changes from the FCC to BCC structure, and the phonon scattering is largely enhanced by a mass mismatch even with a small Al content, effectively suppressing the phonon transport. Simulations showed that the other thermoelectric properties of $Al_xCoCrFeNi$ HEAs were also strongly dependent on the Al concentration. Larger Seebeck coefficients, electrical conductivities, and electronic thermal conductivities are observed at high x_{Al}s due to the increased electron carriers in the BCC structures, which is supported by the calculation of the

electronic band structures and density of states. While the temperature dependence of the phonon transport is not found to be significant due to a minor contribution of interphonon scattering, both the electrical conductivity and Seebeck coefficient increase with temperature, especially at high Al concentrations. This feature allows us to conclude that the thermoelectric performance of $Al_xCoCrFeNi$ HEAs is enhanced by increasing the Al content mainly due to the increase of the thermoelectric power factor at high temperatures, but at low temperatures, the phonon-scattering enhancement by a large atomic mass mismatch is also important. This study will contribute to the design of efficient thermoelectric HEAs for high-temperature applications. Further enhancement is expected to be achieved by more comprehensive evaluation of the HEA's structure and by considering the chemical short-range order and quantification of the random structures. Also, modern data analytics, such as machine learning, can be employed to study a large number of HEAs and predict the thermoelectric performance, thus guiding the experimentalists to design high-performance thermoelectric HEAs effectively.

Chapter 3

Short-Range Order Effects on the Thermodynamic Behavior of $Al_xCoCrFeNi$ High-Entropy Alloys

3.1 Abstract

Short-range order (SRO) in high-entropy alloys (HEAs) has been observed both computationally and experimentally in recent studies. Despite their recognized influence on the physical properties of the HEAs reported, a comprehensive work on the relationship between SRO and the tuning of the thermodynamic properties of HEAs has been lacking. In this research, to identify the SRO-property relationship, the Warren-Cowley (WC) parameters, which quantify the degree of SRO, and thermodynamic properties in $Al_xCoCrFeNi$ HEAs were investigated, utilizing the molecular dynamics (MD) simulations, hybrid molecular dynamics/Monte Carlo (MD/MC) simulations, and density functional theory (DFT) calculations. We examined SROs in different phases of $Al_xCoCrFeNi$ HEAs by varying aluminum (Al) contents (x_{Al}) ranging from 0 to 2.0. Results reveal a prevalent negative SRO of Al-Fe and positive SRO of Al-Al pairs across all HEA cases. Under the influence of SRO parameters, lattice thermal conductivity and bulk modulus exhibit higher values, whereas coefficient of thermal expansion exhibit lower values. This research advances our understanding of the SRO-properties relationship in HEAs, contributing to the design of HEAs with tailored properties through structural tuning.

3.2 Disclosure

Chapter 3 is a modification of the developing manuscript: **Md Abdullah Al Hasan,** Seungha Shin*, Peter K. Liaw, "Short-Range Order Effects on the Thermodynamic Behavior of $Al_xCoCrFeNi$ High-Entropy Alloys". The dissertation author listed in this publication directed and supervised the research which forms the basis for this ongoing publication.

3.3 Introduction

High-entropy alloys (HEAs), which are a novel class of materials containing at least five principal elements [10, 35, 134], have attracted enormous research attention because of their unparalleled compositional varieties and exceptional physical, mechanical, chemical, and magnetic properties, compared to traditional alloys [8, 10, 35, 41, 135]. These unique properties

of HEAs are attributed to their high mixing entropy that stabilizes the random solid solutions [12, 27, 41, 135, 136]. Recent studies reported that not only high configurational entropy but high atomic-level stresses originating from mixing various sizes of elements are also of equal importance [22, 23, 27, 41, 137]. The chemical interaction and atomic-size mismatch often trigger short-range order (SRO) of atomic elements in HEAs, i.e., the preference for certain types of atomic pairing over the first few neighboring shells [22-25, 138].

Short-range ordering in an alloy can affect the system energetics, changing the configurational entropy, free energy, phase diagram, and enthalpy [25, 26]. The SRO was also claimed to be one of the key components influencing various structural and mechanical properties of the HEAs. For example, higher tensile strength in CoCrFeNiPd HEAs [37] and higher mechanical yield strength in CrCoNi alloys have been observed along with the presence of SROs [26, 38]. Therefore, the formation of SROs and their effects on the properties need to be studied and identified for the enhanced understanding and design of HEAs. However, the studies on the SRO in HEAs are very limited in number due to challenges in dealing with the experimental complexities and in interpreting the pair correlations [37, 139]. Despite the challenges in experimentally probing SROs, recent measurements using aberration-corrected transmission electron microscopy (TEM) provided direct evidence that various degrees of SROs exist in $(HfNbTiZr)_{98}O_2$, CoCrFeNiMn, and CoCrFeNiPd [37, 140].

In the quest for understanding SROs, several computational techniques have been employed, including the hybrid density functional theory/Monte Carlo (DFT/MC) [24, 26, 138]. SROs between Ni-Cr, Cr-Co, and Ni-Fe pairs in NiCrCo and NiCrCoFe alloys [26], and Ta-Mo and Nb-Mo pairs in refractory Mo-Nb-Ta-W HEAs [24, 138] have been reported from computational research using DFT/MC. Despite recent progress, studies using DFT/MC suffer from expensive computational cost, especially with large atomic structures. Classical molecular dynamics (MD) allows for simulations with a much larger number of atoms while addressing atomic structures and dynamic behaviors [110, 141, 142]. Through hybrid MD/MC simulations, strong chemical ordering between Fe and Ti was observed in $Co_{30}Fe_{16.67}Ni_{36.67}Ti_{16.67}$, and their effect on dislocation mobility was analyzed [142]. Without first-principles calculations, a force field or

interatomic potential needs to be computed by a mathematical model. However, reliable interatomic potential models for multi-element materials are limited, and the development and validation of such potential models require significant effort.

$Al_xCoCrFeNi$ is one of the most studied HEAs since it possesses a wide variety of microstructures depending on Al concentration, which can induce desired mechanical, thermal, and thermodynamic properties [48-50]. $Al_xCoCrFeNi$ HEA showcases exceptional overall performance and structural applicability when compared to HEA families, i.e., refractory HEAs and CoCrFeNi-based HEAs due to phase changing capability with the addition of Al content [49]. The impact of SRO on the mechanical and thermodynamic properties is crucial to design further improved $Al_xCoCrFeNi$ HEAs to function as a combination of efficient structural materials and functional materials, especially for marine applications, biomedical applications, aerospace applications, and so on [143-145]. A good combination of mechanical and tribological properties in $(NiAl)_x(FeCr)_yCo_{(x+y)/2}$ HEAs has been achieved via adjusting A2/B2 nano-coupled heterostructures [146], where SROs of Fe-Co, Ni-Al and Fe-Cr are enriched. Moreover, significant short-range orders around Al atoms were observed even at high temperatures (~1200°C) in the disordered body-centered cubic (BCC) phase of $Al_xCoCrFeNi$ HEA ($0.875 < x_{Al} \leq 2$) [147]. Although the SRO relationship with the mechanical properties of $Al_xCoCrFeNi$ HEAs have been reported [146, 148] , SRO effect on their thermodynamic properties, specifically thermal conductivity, thermal expansion coefficient, and bulk modulus have not been studied to our best knowledge. Additionally, the thermal transport and thermoelectric properties of $Al_xCoCrFeNi$ HEAs ($0 \leq x_{Al} \leq 2.0$) have been examined in several studies [149, 150]; however, they only addressed the effects of Al content without considering SROs.

In this research, we employed a combination of atomistic modeling techniques, such as molecular dynamics (MD), Monte Carlo (MC), and density functional theory (DFT), to investigate the effect of local atomic order or short-range order (SRO) on different types of thermodynamic properties, including lattice thermal conductivity, thermal expansion coefficient, and bulk modulus of $Al_xCoCrFeNi$ HEAs. The degree of SRO for various atomic pairs was quantified, and the frequencies of atomic orders and their relationship with the examined

thermodynamic properties were analyzed. For more robust analysis, several Al contents in $Al_xCoCrFeNi$ HEAs ($0 \leq x_{Al} \leq 2$) were employed, addressing the SRO-property correlations in different compositions. This paper first introduces atomic configurations of the examined face-centered cubic (FCC) and body-centered cubic (BCC) HEAs and provides the atomistic simulation details, characterization methods for SRO and then calculation of thermodynamic properties. Then, the characteristics of the SRO parameters and their correlations to the thermodynamic properties are determined, and effective design of HEAs using the SRO parameters is discussed.

3.4 Methodology

3.4.1 Atomic Configurations of $Al_xCoCrFeNi$ HEAs

Several Al contents (x_{Al} = 0.3, 0.5, 0.75, 1.0, 1.5, and 2.0) were employed to study the SRO behaviors in $Al_xCoCrFeNi$ HEAs. Initial structures with these Al contents were generated by random substitution of elements for atomistic simulations, following the atomic number ratio of the examined compositions. 3 × 3 × 3 FCC supercells (108 atoms) and 3 × 3 × 3 BCC supercells (54 atoms) with random element distributions were employed for DFT calculations as in Fig. 3.1a, while 21 × 21 × 21 FCC supercells (37,044 atoms) and 21 × 21 × 21 BCC supercells (18,522 atoms) were used for classical MD simulations as in Fig. 3.1b. For each composition, using different seed values for random generator, multiple initial structures (at least five) with different configurations were generated for this study.

3.4.2 Atomistic Simulations: Classical Molecular Dynamics, Hybrid Monte-Carlo/Molecular Dynamics and First-Principles Calculations

Classical MD allows to simulate a large number of atoms and to obtain a long-time correlation, which is essential to reveal the structural and dynamic behaviors of the simulated materials at

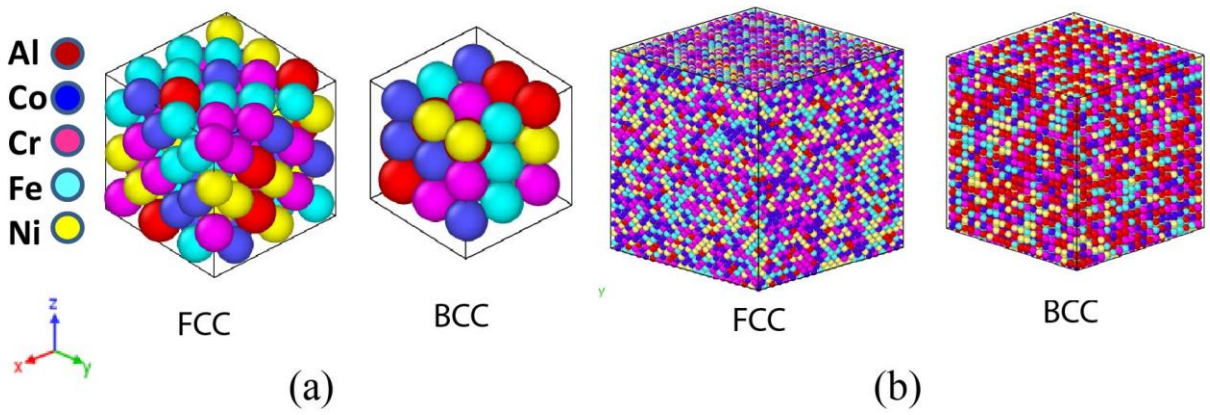

Figure 3.1: (a) Initial 3 × 3 × 3 supercell (FCC: 108 atoms and BCC: 54 atoms) for DFT calculations and (b) 21 × 21 × 21 supercells (FCC: 37,0444 atoms and BCC: 18,522 atoms) of $Al_xCoCrFeNi$ HEA structures for MD simulations.

atomic scale. All the MD simulations were performed using large-scale molecular dynamics massively parallel simulator (LAMMPS) [151]. An embedded-atom-method (EAM) potential for Al-Cr-Co-Fe-Ni was employed to describe the atomic interactions [108]. Prior studies on the calculation of the phase stability as a function of Al, cohesive energy, elastic constants, and lattice distortions [108] demonstrate that this potential is reliable and accurate for modeling the thermodynamic properties of the HEA. An energy minimization was conducted for the relaxation of the initial structures, using the conjugate gradient (CG) algorithm. The minimization process was conducted until the maximum net atomic force was below 10^{-10} eV/Å and the energy change between successive iterations is less than 10^{-10} of the total energy. Periodic boundary conditions were applied to the *x*, *y*, and *z* directions, and the timestep was chosen as 1 fs. An isothermal, isobaric ensemble, *NPT* (constant number of atoms, constant pressure, and constant temperature) was employed to perform the relaxation under zero pressure. Then, switching the *NPT* ensemble to canonical *NVT* ensemble (constant number of atoms, volume, and temperature), simulations continued for 10 ns to produce the atomic data for the characterization of the materials. A Nosé-Hoover thermostat and barostat were applied to control the temperature and pressure, respectively [152, 153].

Hybrid molecular dynamics/Monte Carlo (MD/MC) was employed to assess the short-range order in the HEAs. Random atomic swaps through MC led to the equilibration of the structure that cannot be obtained via conventional MD simulations. The hybrid MD/MC method was employed here under the variance-constrained semi-grand canonical ensemble [154]. The acceptance of MC swap between two different types of atoms is determined by the Metropolis criterion. After an atomic swap, if the energy of the swapped configuration is lower than that of the configuration before the swap, the proposed swap is accepted. However, a swapped configuration with higher energy can also be accepted with an acceptance probability, $\exp(-\Delta E/k_B T)$, where ΔE represents the change in potential energy associated with the proposed swap, and k_B denotes the Boltzmann constant. In the hybrid MD/MC process, a single MC cycle, comprising 1,500 trial swaps for each atomic pair, was performed every 1,000 MD time steps. Given that there are 10 combinations of two dissimilar atomic types in five-element HEAs, a

total of 15,000 MC swaps were attempted in one MC cycle. 1,500,000 MD time steps with a time step of 1 fs (equivalent to 1.5 ns) were executed for the hybrid MD/MC, resulting in 1,500 MC cycles and 22,500,000 MC swap attempts. Subsequently, bulk relaxations were performed via annealing for 1 ns employing the *NPT* ensemble, and the system will be equilibrated for another 500 ps, employing the *NVT* ensemble. During this process, the potential energy and the coordinates of the system were recorded.

First-principles calculations based on the density functional theory (DFT) were conducted to determine the equilibrium energy and lattice constant. All the DFT simulations were performed using Vienna *ab initio* simulation package (VASP) [115]. Periodic boundary conditions were applied in all directions. The projected augmented-wave (PAW) pseudo-potentials with the Perdew-Wang exchange-correlation were adopted here. A $2 \times 2 \times 2$ Γ-centered *k*-point sampling was used for the integration over the Brillouin zone. The plane-wave cutoff energy was set to 400 eV, and the electronic-convergence criterion was to 10^{-4} eV. The conjugate gradient method facilitated for the self-consistent calculation of the structure optimization. To identify and visualize crystalline order in atomic structures from both classical and quantum simulations, the common neighbor analysis (CNA) was conducted, using the Open Visualization Tool (OVITO) [155].

3.4.3 Characterization of HEAs

The Warren-Cowley (WC) parameter characterizes the degree of short-range order in $Al_xCoCrFeNi$ alloys. The WC parameter (α_{ij}) for two atom species *i* and *j* is calculated as [86]

$$\alpha_{ij} = 1 - \frac{p_{ij}}{c_j}, \tag{3.1}$$

where c_j is the molar fraction of the type *j* element, and p_{ij} is the probability of finding the *j*-type element around the *i*-type element in the nearest neighbor shell. The WC parameter is zero if $p_{ij} = c_j$, which indicates that there is no site preference between the *i*-type and *j*-type elements. The

negative α_{ij} represents the increase in the number of *i* and *j* pairs, while the positive value corresponds to the opposite.

For comprehensive evaluation of the SRO effects, we examined different types of thermodynamic properties of the HEAs, which are the lattice thermal conductivity, coefficient of thermal expansion, and bulk modulus, representing the effectiveness of thermal transport, the structural response to temperature changes, and the structural response to mechanical stress, respectively. To calculate thermal conductivity, equilibrium molecular dynamics (EMD) simulations, where a finite, uniform temperature is applied to the simulation domain, were conducted using *NPT* ensemble for first 2 ns of the equilibration, followed by the *NVT* ensemble (constant number of particles, volume, and temperature) for the next 8 ns, resulting in a total simulation time of 10 ns. The last 5 ns of the resulting data were recorded and used to calculate the lattice thermal conductivity (k_L) by the Green-Kubo formula [156, 157]:

$$k_L = \frac{V}{3k_B T^2}\int_0^\infty \left\langle \boldsymbol{J}(0)\cdot\boldsymbol{J}(t)\right\rangle dt, \tag{3.2}$$

where ⟨⟩ is the ensemble average, *V* is the equilibrium volume, and ***J*** is the heat-flux vector. Phonon density of states (D_p) , which helps in understanding the behavior of lattice thermal conductivity, is calculated through the Fourier transform of the velocity autocorrelation function obtained from MD simulations [112].

The coefficient of thermal expansion (*CTE*) using the centered finite difference method as [158]

$$CTE = \frac{1}{3V(P,T)}\frac{V(P,T+\varepsilon)-V(P,T-\varepsilon)}{2\varepsilon}, \tag{3.3}$$

where ε represents an increment/decrement value of temperature (±20 K).

The stiffness or elastic constants were determined from the stress-strain relation, as expressed by the Hooke's law [158, 159],

$$C_{ij} = \frac{\sigma_i}{\varepsilon_j}, \tag{3.4}$$

where σ_i is the stress tensor, and ε_j is the strain tensor. Due to the cubic symmetry of FCC and BCC HEAs, only three independent elastic constants (C_{11}, C_{12}, and C_{44}) were identified. Subsequently, the bulk modulus (B) was determined using these elastic constants results from MD simulations [159, 160]

$$B = \frac{C_{11} + 2C_{12}}{3}, \tag{3.5}$$

where C_{11} and C_{12} represent the elastic stiffness constants of a cubic single crystal.

Additionally, the B was also calculated, employing the Birch-Murnaghan equation of state and the average atomic energy with respect to the volume from the DFT calculations [161, 162]:

$$E(V) = E_0 + \frac{9V_0B}{16}\left\{\left[\left(\frac{V_0}{V}\right)^{\frac{2}{3}} - 1\right]B' + \left[\left(\frac{V_0}{V}\right)^{\frac{2}{3}} - 1\right]^2\left[6 - 4\left(\frac{V_0}{V}\right)^{\frac{2}{3}}\right]\right\}, \tag{3.6}$$

where B', and V_0 represent the derivative of the bulk modulus with respect to pressure, and the equilibrium volume, respectively.

3.5 Results and Discussion

A previous study [149] on $Al_xCoCrFeNi$ HEAs confirmed that lower Al contents ($0 \leq x_{Al} \leq 0.75$) result in FCC structure while higher Al contents ($0.875 \leq x_{Al} \leq 2$) stabilize the BCC structure, which is aligned with this research; x_{Al} = 0.3, 0.5, and 0.75 for FCC and x_{Al} = 1.0, 1.5, and 2.0 for BCC. The distinct phases observed in the $Al_xCoCrFeNi$ HEAs can be attributed to the valence electron concentration (VEC), which is dependent on the chemical composition. VEC is regarded as one of the key factors determining the phase stability of the HEAs [163]. It is calculated using the atomic fraction and the VEC value of each individual element, denoted as c_i

and $(VEC)i$ for element i, respectively, as $VEC = \sum_{i=1}^{n} c_i \left(VEC\right)_i$ [20, 163]. FCC solid solutions tend to form at VEC > 7.8, whereas BCC solid solutions are formed at VEC < 7.35 [163-165]. Our findings, revealing different concentration of element pairs in FCC and BCC phases, were aligned with this VEC analysis. Lower Al concentrations in $Al_{0.3}$CoCrFeNi HEA, led to a higher VEC (> 7.8) for a strong FCC phase formation whereas higher Al concentrations led to lower VEC (< 7.35) indicating a strong BCC phase formation.

The atomic structures were relaxed to obtain the minimum energy structure, and thus the equilibrium lattice constant using DFT calculations and MD simulations. The calculated lattice constants (3.59 Å for x_{Al} = 0.3 and 2.88 Å for x_{Al} = 2.0) from our simulations are in a good agreement with the experimental results (3.59 Å and 2.88 Å, respectively) [166, 167], as shown in Fig. 3.2.

High-entropy alloys exhibit different structural orders depending on their atomic composition and configuration. Here, the Warren-Cowley (WC) parameters (α_{ij}) for various element pairs in Al_xCoCrFeNi HEAs were calculated to understand such structural orders and their influence on the thermodynamic properties of the HEAs. Initial configurations of the HEAs for each atomic composition (x_{Al} = 0.3, 0.5, 0.75, 1.0, 1.5, and 2.0) were relaxed at room temperature (~300 K) using hybrid MD/MC simulations, and the initial and relaxed structures were then utilized to calculate the WC parameters for each element pair, within all FCC and BCC structures of Al_xCoCrFeNi HEAs. The WC parameters for each element pair in all initial and relaxed structures for FCC and BCC HEAs are presented in Fig. 3.3.

Almost zero values of WC parameters were observed in the random configurations of both FCC (x_{Al} = 0.3) and BCC (x_{Al} = 2.0) HEA cases, indicating no specific preference for certain atom pairs [168]. After the MC relaxation process, the WC parameters of the Al-Fe and Al-Al were found to be most negative and most positive, respectively, in both FCC HEAs (x_{Al} = 0.3) and BCC HEAs (x_{Al} = 2.0), as illustrated in Fig. 3.3. Negative or lower WC parameters suggest a

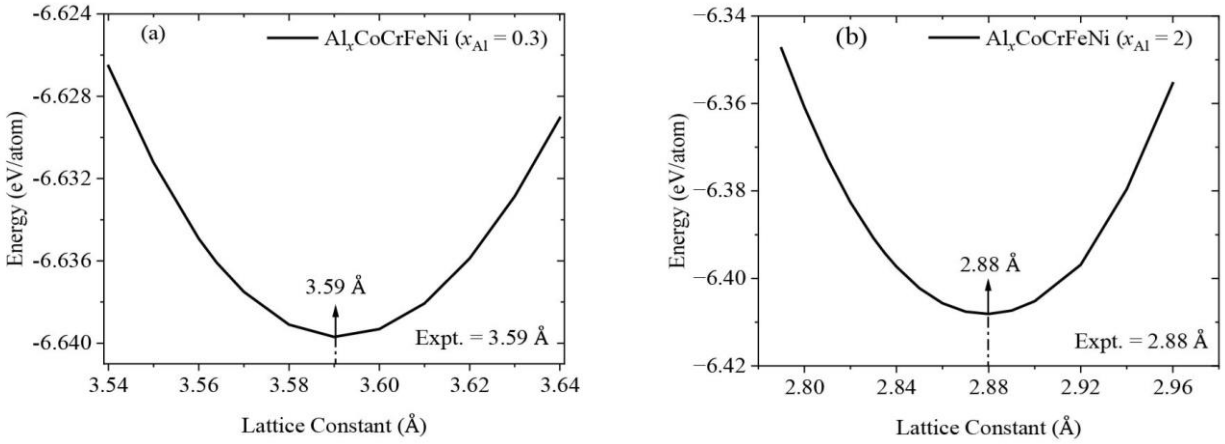

Figure 3.2: Equilibrium lattice constant for FCC (x_{Al} = 0.3) and BCC (x_{Al} = 2.0) HEAs using DFT calculations. Lattice constants from the simulations agree well with the experimental measurements [166, 167].

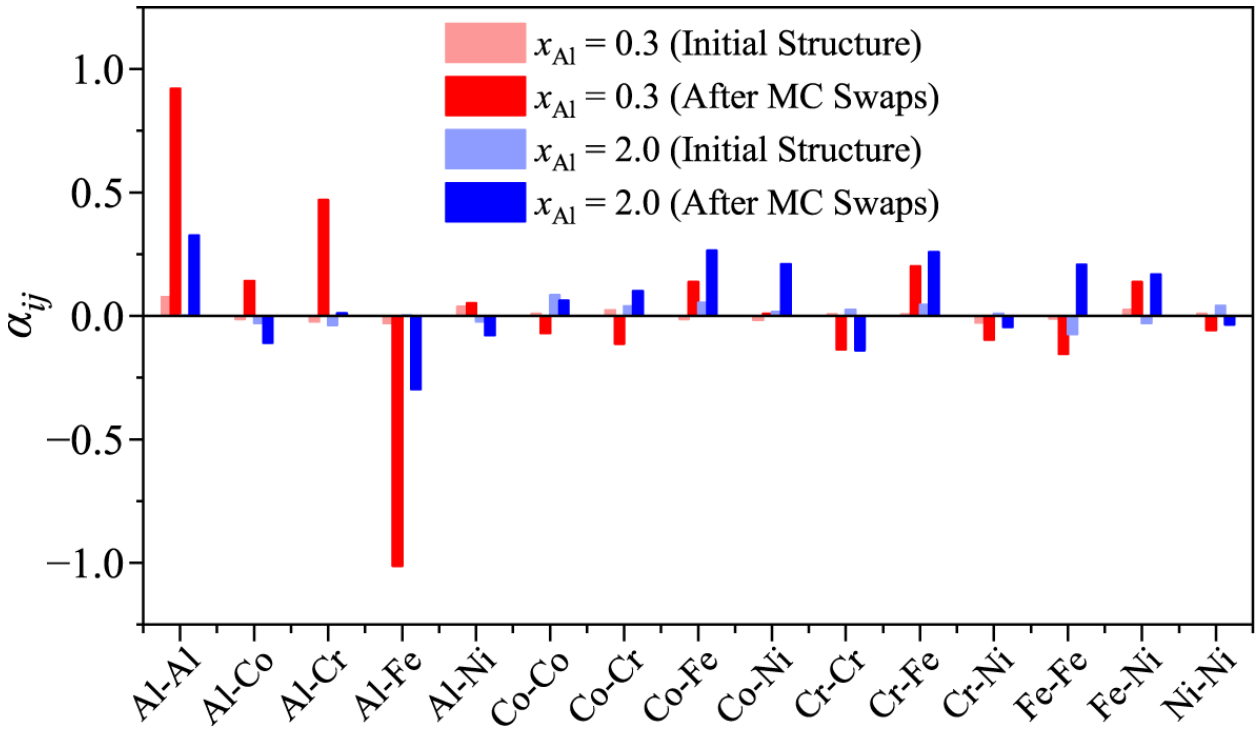

Figure 3.3: Warren-Cowley (WC) parameters for the FCC (x_{Al} = 0.3) and BCC (x_{Al} = 2.0) HEAs. Initial structures with WC parameters close to zero demonstrate randomness. Higher negative values of WC parameters in HEAs after MC swaps indicate strong short-range ordering (SRO) in the HEAs.

higher preference for the corresponding atom pair, indicating increased short-range ordering [168]. Therefore, Al-Fe was expected to be the dominant pairs for short-range ordering in the FCC and BCC HEAs. Conversely, the Al-Al pair was strongly unfavorable in both FCC and BCC HEAs. Apart from the dominant pairs, distinct SRO features were observed in FCC and BCC HEAs. Specifically, Al-Co was unfavorable while Co-Cr was favorable in the case of FCC HEAs, whereas the opposite trend was found for the BCC cases. Moreover, Al-Cr appeared to be unfavorable in FCC HEAs, whereas it did not have much impact in BCC HEAs. The opposite trend was found for the Co-Ni pair. Furthermore, Cr-Fe and Co-Fe pairs were unfavorable in both FCC and BCC HEAs.

To examine the effect of Al concentration on the SRO parameters, various HEAs with different Al concentrations (x_{Al} = 0.3, 0.5, 0.75, 1.0, 1.5, and 2.0) were analyzed, as demonstrated in Fig. 3.4. A discernible pattern in the SRO parameters was observed here: as the Al content increases in the HEAs, the absolute value of WC parameters of favorable Al-Fe pair, while those of unfavorable Al-Al pair also decreased. Consequently, it can be stated that the intensity of SRO is higher in the FCC HEAs with lower Al contents, and the SRO becomes less pronounced in the BCC HEAs with higher Al contents.

The lattice thermal conductivities (k_L), coefficient of thermal expansion (*CTE*), and bulk modulus (B) of the $Al_xCoCrFeNi$ ($0 \leq x_{Al} \leq 2$) HEAs were evaluated via MD simulations using initial random configurations (denoted as ‘random’ or ‘without SRO’) and those after MC swaps showing more significant SRO (denoted as ‘SRO’ or ‘with SRO’). Bulk modulus was also calculated using DFT, and the obtained values exhibit good agreement with the MD results, as presented in Table 3.1. Moreover, the simulated bulk modulus values agree well with the experimental results of AlCoCrFeNi HEA [167]. This concurrence between MD, DFT, and experimental results not only supports the validity of our approaches, but also underscores the reliability of the EAM potential employed in this study, specifically in calculating thermodynamic properties using MD simulations.

Table 3.1: Comparison of the bulk modulus of the AlxCoCrFeNi HEA from MD simulations, DFT calculations, and literature [52].

Configurations	Lattice Constant (Å)		Bulk Modulus (GPa)	
	MD Simulations	DFT Calculations	MD Simulations	DFT Calculations
FCC (x_{Al} = 0.3)	3.585	3.589	192.55	196.09
FCC (x_{Al} = 0.5)	3.538	3.536	183.55	180.79
FCC (x_{Al} = 0.75)	3.552	3.553	162.19	169.13
BCC (x_{Al} = 1.0)	2.841	2.839	151.28	152.07
BCC (x_{Al} = 1.5)	2.863	2.861	158.25	161.09
BCC (x_{Al} = 2.0)	2.875	2.882	148.36	156.84

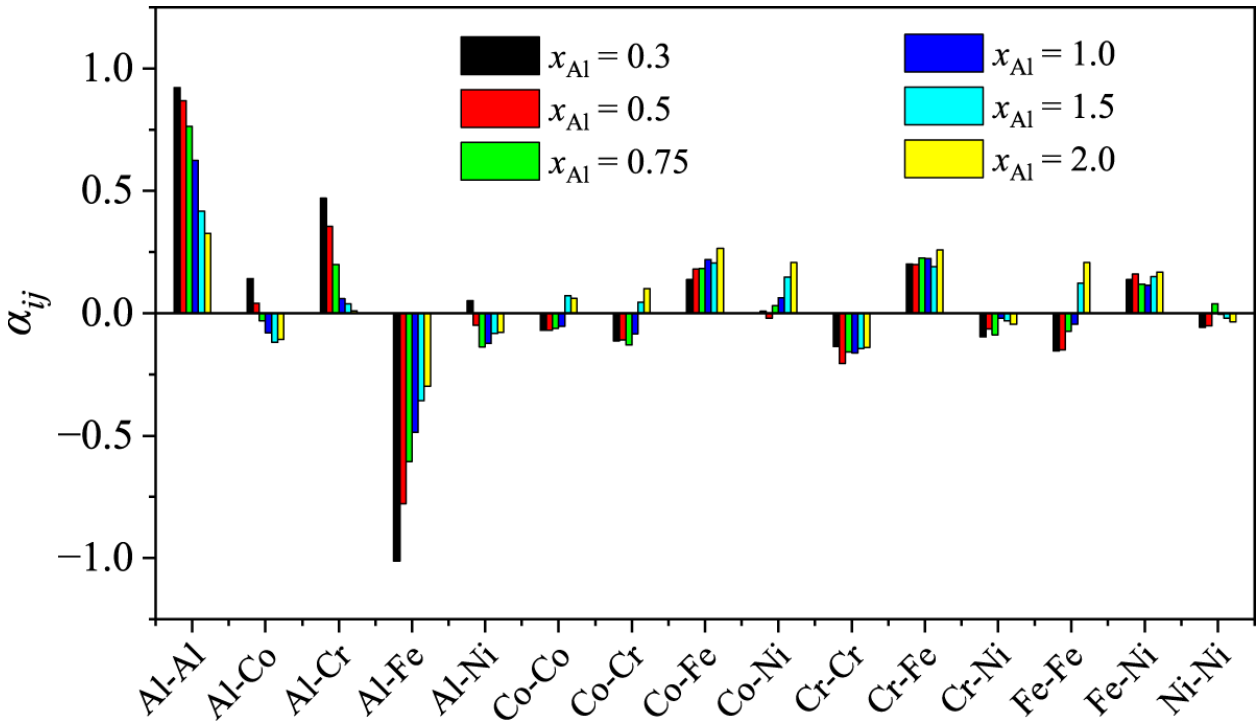

Figure 3.4: WC parameters in the FCC (x_{Al} = 0.3, 0.5, and 0.75) and BCC (x_{Al} = 1.0, 1.5, and 2.0) HEAs after the MC swap process.

Despite having identical atomic compositions, clear differences in thermodynamic properties between random and SRO structures have been observed, and these distinctions can be attributed to the different SROs. Figure 3.5 demonstrates the effect of short-range order on the lattice thermal conductivity, i.e., with the SRO configurations of the HEAs, the lattice thermal conductivity is higher compared to the random configurations.

To further investigate the correlation between SRO and the lattice thermal conductivity, changes in the lattice thermal conductivity from initial random structures to SRO structures are presented with respect to the WC parameters for two selected pairs of SROs, $\alpha_{Al\text{-}Fe}$ and $\alpha_{Al\text{-}Al}$ in Fig. 3.6. The selected Al-Fe pair and Al-Al pair were chosen to represent the most negative and the most positive values of WC parameters within the SRO configurations, respectively, as shown in Fig. 3.4. Absolute values for both $\alpha_{Al\text{-}Fe}$ and $\alpha_{Al\text{-}Al}$ decrease with the increase of Al content in the HEAs, indicating reduced SROs, i.e., less preference or aversion and more random short-range order. A more than 50% increase in lattice thermal conductivity was observed at $x_{Al} = 0.3$, where the SRO intensity is maximum among all the HEAs. In contrast, at $x_{Al} = 2.0$, where SRO is not prominent compared to the random counterpart, the change in lattice thermal conductivity is less than 20%.

Since phonon scattering is enhanced in more disordered structures [169], the higher lattice thermal conductivity in the SRO structures can be attributed to the increased structural order or a less extent of disorder. As shown in Figs. 3.7a and 3.7b, initial random structures without SRO have phonon density of states (or phonon spectra) with more broadened peaks compared to the SRO structures, allowing for an increased possibility of phonon-phonon interactions. These interactions scatter phonon transport, thereby reducing lattice thermal conductivity. Both FCC and BCC HEAs with SRO exhibit reduced broadening in phonon peaks. Specifically, the peak intensity of acoustic phonons, which are responsible for phonon transport, is increased as the Al content decreases. Thus, $Al_xCoCrFeNi$ HEAs exhibit higher thermal conductivity at lower Al contents, and accompanied by enhanced short-range orders.

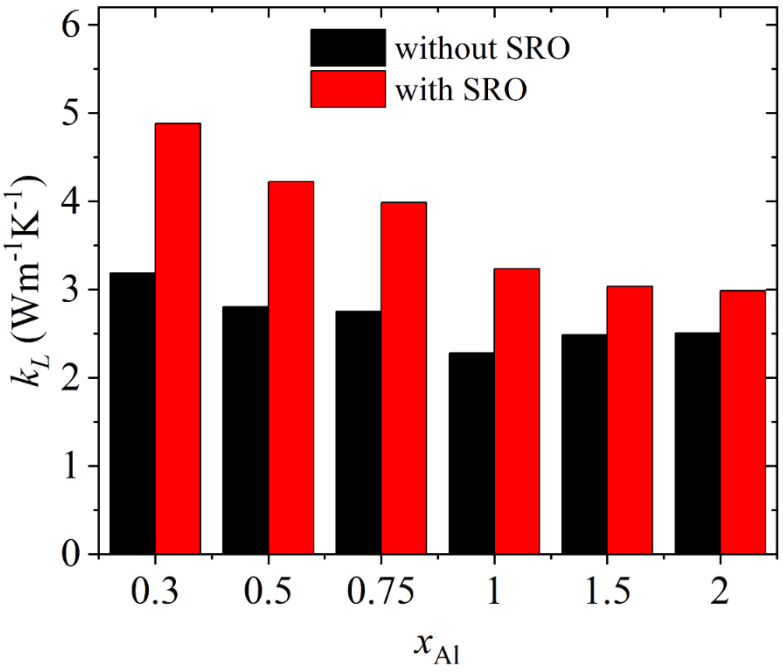

Figure 3.5: Lattice thermal conductivity of $Al_xCoCrFeNi$ ($0 \leq x_{Al} \leq 2$) HEAs with random initial (without SRO) and MC swapped configurations (with SRO).

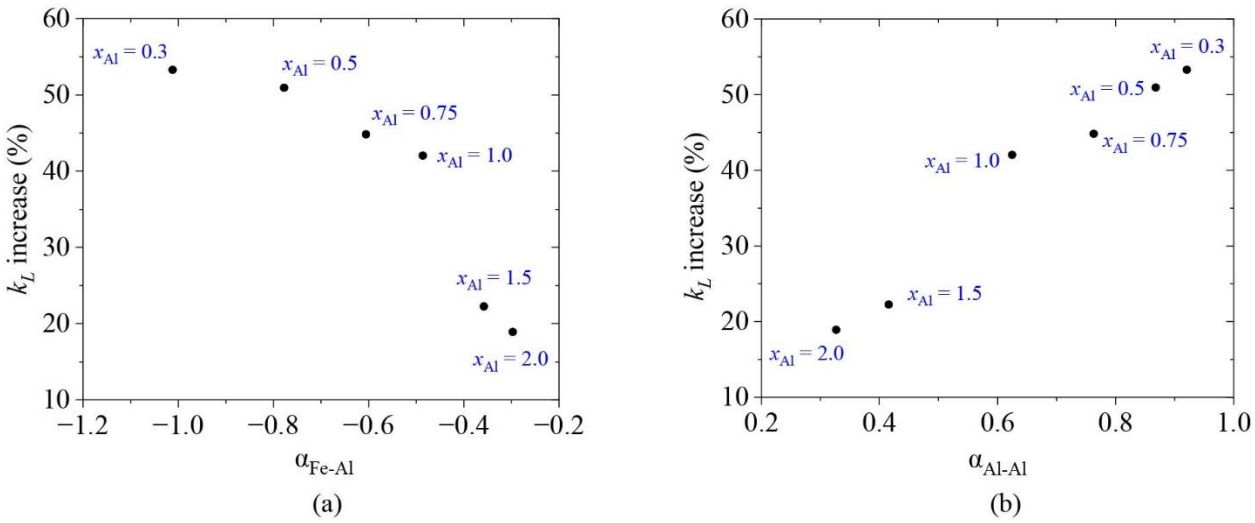

Figure 3.6: (a) Highest increase in lattice thermal conductivity (k_L) can be observed for $Al_xCoCrFeNi$ HEA at x_{Al} = 0.3 with highest negative Al-Fe WC parameters and a decreasing trend can be observed with lower Al-Fe WC values. (b) Lowest increase in lattice thermal conductivity (k_L) can be observed at x_{Al} = 2.0 with lowest positive Al-Al WC values and an increasing trend can be observed with higher Al-Al WC values.

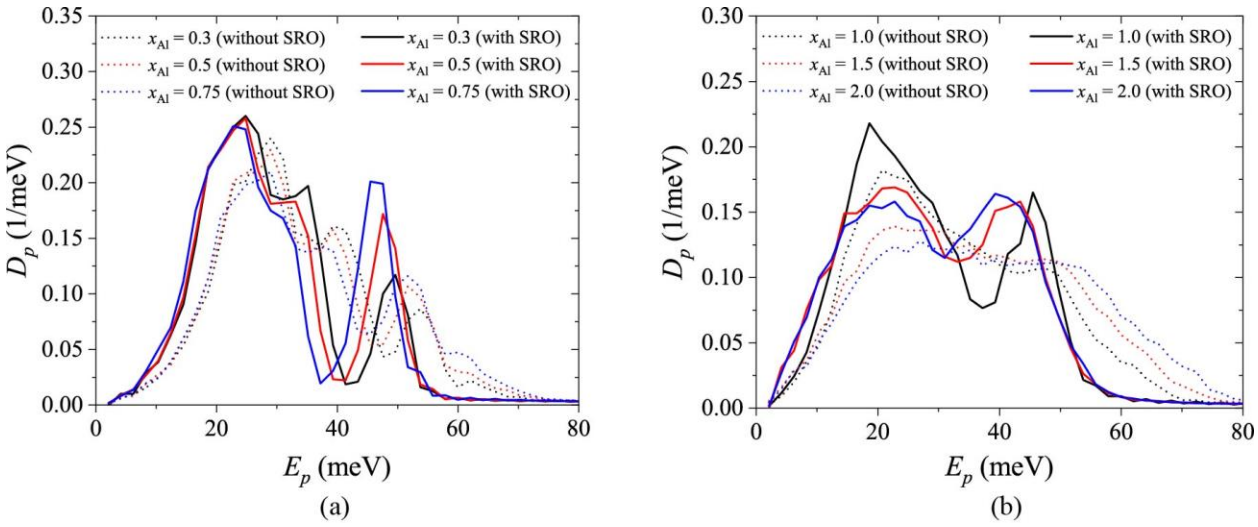

Figure 3.7: Phonon density of states of (a) FCC $Al_xCoCrFeNi$ HEAs ($0 \leq x_{Al} \leq 0.75$) and (b) BCC $Al_xCoCrFeNi$ HEAs ($0.875 \leq x_{Al} \leq 2.0$) with random initial (without SRO) and MC swapped configurations (with SRO).

The SRO configurations resulted in decreased thermal expansion coefficients as depicted in Fig. 3.8a. This decreasing trend contrasts with the case of lattice thermal conductivity. The calculated *CTE* values in this research are in reasonable agreement with the experimental results for $Al_xCoCrFeNi$ HEAs [166]. In addition to thermal expansion, the SRO also affects the bulk modulus of the HEAs. With the SRO configurations of the HEAs, the bulk modulus was found to be higher compared to the structures without SRO, as illustrated in Fig. 3.8b.

We attribute the reduction in thermal expansion coefficient and the increase in bulk modulus to the stronger atomic interactions in the SRO structures. The SRO structures, which result from the MC processes, are more energetically stable with stronger short-range atomic interactions. This leads to reduced sensitivity of structural changes to external temperature variations or mechanical pressure, that is, smaller thermal expansion and larger modulus can be induced. The changes in both the coefficient of thermal expansion and bulk modulus increase with the increasing WC parameters or more SRO in the configurations, similar to lattice thermal conductivity trend shown in Fig. 3.5. Finally, it can be stated that the properties of both FCC and BCC HEAs can be enhanced by tuning dominant element pairs according to their SRO parameters.

3.6 Conclusions

These changes are attributed to the suppressed phonon-scattering and increased energetic stability induced by the enhanced SRO. This work provides an insight into different interactions between element pairs and physical properties of the HEA. Therefore, this study will contribute to a quantitative theory-guided design strategy for selecting HEA elements and tuning composition to control the structural, chemical, and mechanical properties.

Thermodynamic properties of the HEAs and their correlation with local atomic ordering are crucial when designing efficient HEAs, however, this phenomenon was not explored in-depth yet. Thus, effect of short-range order on lattice thermal conductivity, thermal expansion coefficient, and bulk modulus of the $Al_xCoCrFeNi$ HEAs ($0 \leq x_{Al} \leq 2$) was investigated using

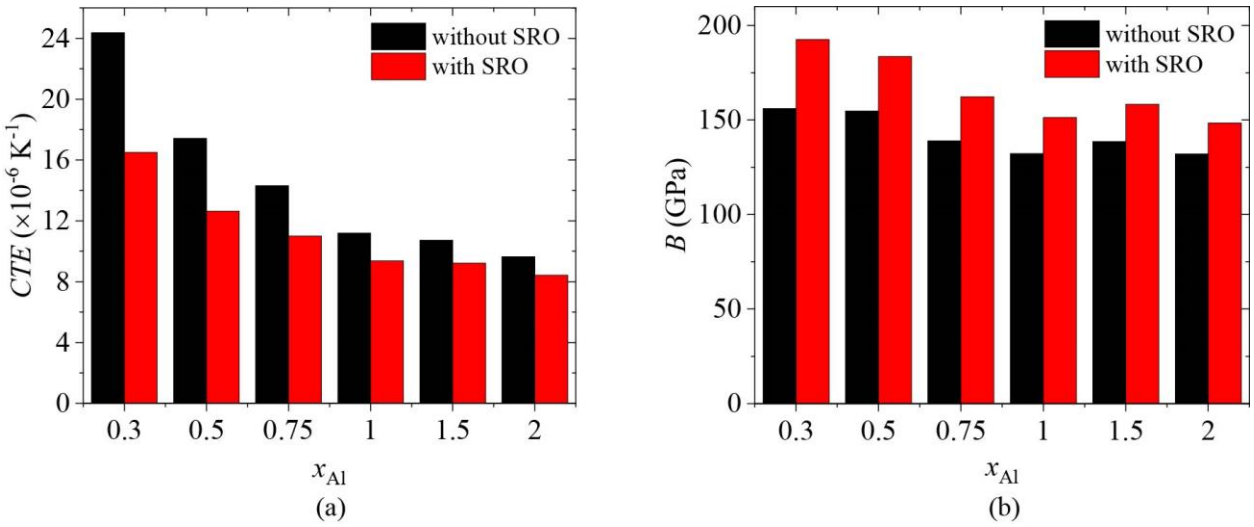

Figure 3.8: (a) Coefficient of thermal expansion of $Al_xCoCrFeNi$ ($0 \leq x_{Al} \leq 2$) HEAs with random initial (without SRO) and MC swapped configurations (with SRO). (b) Bulk modulus of $Al_xCoCrFeNi$ ($0 \leq x_{Al} \leq 2$) HEAs with random initial (without SRO) and MC swapped configurations (with SRO).

hybrid MD/MC simulations, classical MD simulations, and DFT calculations. The WC parameters were employed to characterize the ordering strength of the constituent element pairs in the $Al_xCoCrFeNi$ HEAs. From this study, Al-Fe was identified to be the most favorable pair, while Al-Al emerged as the most unfavorable pair among all the HEAs. We observed that increasing the element pairs with higher SRO results in higher thermal conductivity, lower thermal expansion, and higher bulk modulus of the HEAs.

Chapter 4

Effects of Alloying and Short-Range Order on the Mechanical Strength of AlCoCrFeNi High-Entropy Alloys via Atomistic Simulations and Modern Data Analytics

4.1 Abstract

High-entropy alloys (HEAs), specifically Cantor alloys, have garnered significant attention due to their adaptability in adjusting physical properties. Improving mechanical strength is crucial to broaden their effectiveness in structural applications. By varying alloy concentration in Cantor alloys, the mechanical strength is expected to be greatly enhanced. Additionally, recent investigations via computational and experimental approaches have revealed that short-range orders (SRO) significantly impact the physical properties of HEAs. Nevertheless, there remains a notable gap in comprehensive investigations into the correlation between SRO and the mechanical properties of HEAs. Therefore, in this study, the effect of alloying concentration and short-range order on the mechanical strength of the AlCoCrFeNi HEAs are investigated by utilizing molecular dynamics (MD) simulations, hybrid molecular dynamics/Monte Carlo (MD/MC) simulations, and modern data analytics. Correlation analysis was performed to determine the importance of the input features while evaluating the mechanical properties of the HEAs. Several machine learning (ML) algorithms are trained using SRO parameters and composition concentration to predict the yield strength of the HEAs. Finally, a performance comparison among the ML models was demonstrated and best predictive models were discussed. This research facilitates comprehensive understanding of the SRO-mechanical property relationship in the HEAs, contributing to the design of the HEAs with improved mechanical strength.

4.2 Disclosure

Chapter 4 is a modification of a manuscript preparing for publication: **Md Abdullah Al Hasan,** Seungha Shin*, Peter K. Liaw, " Effects of Alloying and Short-Range Order on the Mechanical Strength of AlCoCrFeNi High-Entropy Alloys via Atomistic Simulations and Modern Data Analytics". The dissertation author listed in this publication directed and supervised the research which forms the basis for this publication.

4.3 Introduction

The demand for new generations of materials that can function in extreme environments is rapidly increasing. To address this challenge, high-entropy alloys (HEAs) are being extensively studied due to their stability at high temperatures with promising mechanical properties, such as tensile strength, hardness, and ductility [10, 41, 135]. Since the discovery of HEAs by Yeh *et al*. and Cantor *et al*. in 2004 [8, 10], they have garnered significant attention among researchers because of their unique solid solution phase formation and enhanced physical properties [8, 10]. Cantor et al. initiated this investigation of multi-component alloys with 16-element and 20-element HEAs and found these alloys to have a brittle and multiphase nature [7]. However, within the alloys, they surprisingly discovered Fe, Ni, Cr, Co, Mn formed a single-phase FCC structure [8]. Since then, FeNiCrCoMn FCC HEAs and their derivatives have undergone extensive study. High configurational entropy, lattice distortion, sluggish diffusion, and cocktail effects are regarded as the factors related to this phase stability. Subsequently, notable efforts have been made to investigate various compositions in order to discover novel HEAs.

HEAs offer vast compositional space to explore, and due to their adjustable physical properties at different composition concentrations, it is crucial to investigate them comprehensively to identify HEAs with desirable properties. However, it is extremely difficult to examine all possible compositions both experimentally and theoretically. Investigating the multitude of alloy combinations experimentally is highly inefficient and costly, and thus, several computational techniques have been developed to tackle this challenge, such as atomistic simulations: molecular dynamics, hybrid molecular dynamics/Monte Carlo simulations, density functional theory and so on [104, 138, 149, 170, 171]. Even these atomistic simulations are not regarded effective in recent times since these methods require also substantial computational costs.

Recently, researchers have relied on machine learning (ML) algorithms, in combination with existing theoretical and experimental techniques, to identify new compositions and predict their properties [172-176]. Various machine learning algorithms, such as linear regression, support vector machine, artificial neural networks, and Random Forest have been employed to accelerate

the HEA design research [172, 175, 176]. Recent ML research can be categorized into two main groups: classification ML models and regression ML models. Classification ML models are used for phase prediction, determining single-phase (FCC or BCC), or multi-phase formation, whereas regression ML models are utilized for predicting mechanical properties, e.g., hardness, tensile strength, etc. However, the majority of ML research focuses on predicting phase formation in HEAs based on the similar descriptors, such as atomic radius, VEC (valence electron concentration), shear modulus, electronegativity, and so on [172, 177-180]. ML research on phase formation prediction that was performed by Yegi et al. implemented various classification ML models [181]. Zhang et al. introduced genetic algorithms for material descriptor selection while predicting phases in HEAs in his ML research [182], and they also improved the ML model accuracy by incorporating feature selection algorithms and support vector machine (SVM) [183]. The usage of various material descriptors has become popular in several studies of HEA phase prediction [173, 182, 184].

Besides phase formation prediction, the design of HEAs with targeted desirable properties is crucial for a wide range of industrial applications and ML models can be addressed to achieve this objective. Wen et al. reported ML models to predict the composition of the HEAs with increased hardness [173]. Huang et al. predicted HEA phase formation and enhanced hardness using ML models, even though the sample data was relatively small [178]. Sun et al. implemented ML algorithm to predict desired hardness in TiZrNbTa HEA [185]. Combination of ML model with molecular dynamics (MD) simulations to design multicomponent alloys was demonstrated by Li et al. [186]. Random Forest ML model along with feature selection were utilized by Xiong et al. to predict the hardness of the complex concentrated alloys [187]. One of the key challenges of ML methods is that it requires a large amount of training data which is mostly lacking in previous years. At present, ML models primarily concentrate on utilizing a limited available experimental dataset to model the physical properties of all HEAs, which includes overlapping elemental concentrations. Nevertheless, developing a reliable machine learning prediction model for HEAs with a specific composition requires precise adjustments to

element concentrations and the corresponding calculation of properties, an aspect that is currently lacking.

The most studied cantor HEAs contain equiatomic compositions since that is the most convenient way of studying a new alloy system [179, 188]. However, equiatomic HEAs might not always have the desirable properties. Additional elements were considered mixing with Cantor HEAs to increase physical properties, so far, Al content is the most notable one changing the microstructure of this FCC HEAs entirely, such as increasing Al concentration led to single FCC, FCC+BCC, and single BCC phase respectively [166, 189, 190]. This behavior might be attributed to the larger size and lower mass of Al content. Moreover, AlCoCrFeNi, being the most studied HEA, exhibits excellent yield strength, hardness, thermal conductivity by tuning this Al concentration [48-50]. However, unlike Al concentration, other constituent elements were not given due attention. Few studies suggest that Co, Cr, Fe, and Ni concentrations can also improve the HEA properties other than Al, for instance, a non-equiatomic $Fe_{40}Mn_{27}Ni_{26}Co_5Cr_2$ HEA was reported to possess extraordinary phase stability and outstanding tensile strength [191]. Moreover, $Co_{25}Ni_{25}Fe_{25}Al_{7.5}Cu_{17.5}$ demonstrated higher yield strength compared to other equiatomic FCC HEAs [192]. Famous pioneer of HEA, Yeh suggested that one may find great treasure by carefully exploring and tailoring microstructures of non-equimolar HEAs [43]. Although some previous studies focus on the mechanical properties of the AlCoCrFeNi HEAs via MD simulations and ML models [177-180], they lacked the inclusion of short-range order (SRO) parameters as input features while evaluating the HEA properties. Recent studies have emphasized that SRO parameters have significant impact on the physical properties of medium-entropy alloys and high-entropy alloys [26, 37, 38, 140, 193-195]. However, to our best knowledge, no ML models were developed leveraging these SRO parameters as input features to predict HEA properties.

Therefore, in this research, ML models are employed to predict mechanical strength of the AlCoCrFeNi HEA utilizing SRO parameters of different element pairs. Here, Al, Co, Cr, Fe, and Ni concentrations are adjusted incrementally and corresponding SRO parameters of all the element pairs are calculated for each combination of AlCoCrFeNi HEA. SRO parameters are

introduced via hybrid molecular dynamics/Monte-Carlo (MD/MC) simulations and yield stress of the HEAs are calculated employing molecular dynamics (MD) simulations. The correlation between SRO parameters and mechanical strength is determined, a performance comparison to evaluate the best predictive ML model is demonstrated, and effective design of HEAs is discussed.

4.4 Methodology

4.4.1 Atomic Configurations

Various concentrations of Al, Co, Cr, Fe, and Ni elements were employed to study the alloying effect on the mechanical properties of AlCoCrFeNi HEAs. Several initial structures with these contents were generated by random substitution of elements using large-scale molecular dynamics massively parallel simulator (LAMMPS) script, as shown in Fig. 4.1. For classical MD simulations, two major phases face-centered cubic (FCC) and body-centered cubic (BCC) are considered and 15 × 15 × 15 FCC supercells (13,500 atoms) and 15 × 15 × 15 BCC supercells (6,750 atoms) were created. A total of 250 HEA structures were created by adjusting the composition concentrations of Al, Co, Cr, Fe, and Ni ranging from a minimum of 5% to a maximum of 35%, with an increment of 1% for each element concentration.

4.4.2 Atomistic Simulations: Classical Molecular Dynamics & Hybrid Molecular Dynamics/Monte-Carlo Simulations

In this study, classical MD simulations were performed to simulate the HEAs to obtain the structural and dynamic behaviors at the atomic level. For these simulations, the LAMMPS (large-scale molecular dynamics massively parallel simulator) package was employed [151] with an embedded-atom-method (EAM) potential to describe the atomic interactions of Al-Co-Cr-Fe-Ni [108, 170]. Previous studies on the calculation of the phase stability as a function of Al, cohesive energy, elastic constants, and lattice distortions [108] demonstrate that this potential is

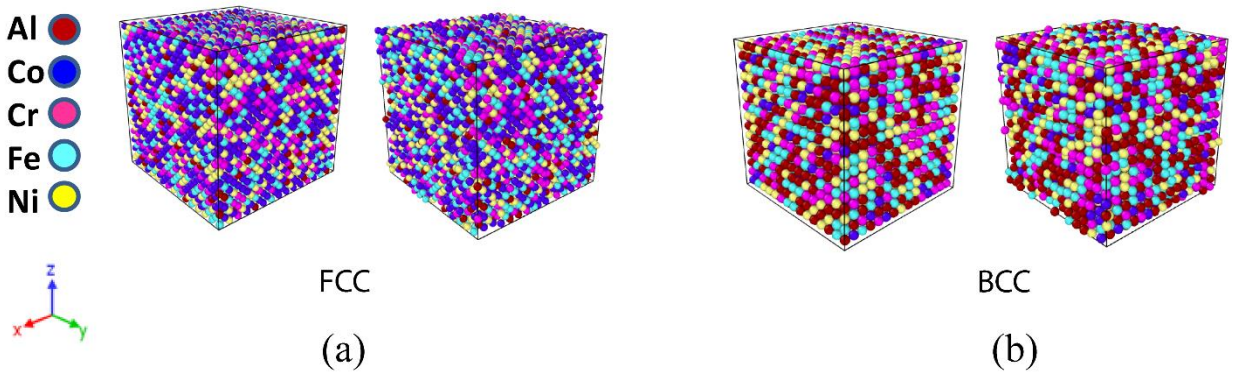

Figure 4.1: (a) Initial and energy minimized 15 × 15 × 15 FCC supercells (13,500 atoms) of $Al_{0.3}Co_{1.7}CrFeNi$ HEA and (b) initial and energy minimized 15 × 15 × 15 BCC supercells (6,750 atoms) of $Al_{1.5}Co_{0.5}CrFeNi$ HEA structures for MD simulations.

reliable and accurate for modeling the mechanical properties of the HEA. For the LAMMPS simulations, the timestep was chosen as 1 fs and the periodic boundary conditions were applied to the *x*, *y*, and *z* directions. The initial geometric structures of the HEAs were optimized via an energy minimization using conjugate-gradient algorithms with a force and energy precision of 10^{-10} eV/Å and 10^{-10}, respectively. After the minimization, a subsequent structure relaxation was performed for at least 50 ps by employing an isothermal, isobaric ensemble, *NPT* (constant number of atoms, constant pressure, and constant temperature). A Nose-Hoover thermostat was applied to control the temperature [152] and the velocity-Verlet algorithm was utilized to solve the MD equations. To calculate the yield stress, a uniaxial tensile loading method is adopted here. The tensile load was applied to the *x* direction of the HEAs with a strain rate of 1×10^9 s^{-1} in the simulations. The pressure in the *y* and *z* direction was always set to zero.

Moreover, in this research, hybrid molecular dynamics and Monte Carlo (MD/MC) was utilized to introduce the short-range order (SRO) in the HEAs via Monte Carlo atomic swaps. The variance-constrained semi-grand canonical ensemble [154] was used in these simulations. The potential energies of the original and swapped configurations were compared to determine the swap acceptance via Metropolis criterion. The hybrid MD/MC process was carried out for a total of 150,000 MD time steps with 1 fs timestep, in which for every 100 MD time steps, one MC cycle consisting of 100 MC trial swaps were attempted for each atom pair. Since there are 10 combinations of two dissimilar atomic types in a five-element HEA, therefore, in total, the atoms in each HEA were relaxed by 1500 ps and 1,500,000 attempted MC swaps. Then the SRO HEA structures were collected for further stress-strain calculations via MD simulations. The stress-strain curve for each HEAs were recorded from the MD simulations for both SRO and without SRO HEA structures.

4.4.3 Data Analytics

We quantified the correlations between mechanical properties (target properties) and SRO parameters (input features), using the Pearson's correlation coefficient (PCC) and maximal information coefficient (MIC) analysis [196-198]. PCC quantifies the linear correlations and is

represented as the quotient of the covariance of two variables and the product of their standard deviations, as shown in Eq. 1. While the PCC values range from -1 to 1, representing complete negative to complete positive correlation, absolute PCC values were used to demonstrate the relative correlation strength (the larger PCC value, the stronger correlation). The PCC values can be determined as [183, 199]

$$PCC = \frac{\sum_{i=1}^{n}(x_i - \bar{x})(y_i - \bar{y})}{\sqrt{\sum_{i=1}^{n}(x_i - \bar{x})^2}\sqrt{\sum_{i=1}^{n}(y_i - \bar{y})^2}}, \quad (1)$$

where x and y represent two distinct features, n is the total number of instances in the dataset, $\bar{x} = \frac{1}{n}\sum_{i=1}^{n} x_i$, and $\bar{y} = \frac{1}{n}\sum_{i=1}^{n} y_i$.

Moreover, the MIC is employed to explore to capture both linear and non-linear correlations between input features and target properties. MIC values range from 0 to 1, where '0' means statistical independence and '1' represents a noiseless functional relationship. These approaches complement each other, enabling a more comprehensive correlation analysis.

Machine-learning (ML) algorithms have been proven as effective optimization techniques for the modeling of complex systems and prediction of various physical quantities [172, 200, 201]. For instance, prediction of interatomic potentials [202-204], atomic forces, and formation energy using machine learning has demonstrated a success [205-207]. Several ML algorithms were considered in this study, such as Neural Network (NN), Gradient-Boosting Regression (GBR), Random Forest (RF), Linear Regression (LR), Bayesian Ridge (BR), Decision Tree Regression (DTR), Elastic-Net Regression (ENR), Support Vector Regression (SVR), and Least Absolute Shrinkage and Selection Operator Regression (LASSO). The selected algorithms are widely used regression models and can predict the linear relationship among the variables. Moreover, ML models employing these algorithms tend to perform better while working with a small sample size. The data generated from MD simulations was employed to train the machine learning (ML)

models. The trained ML models were then employed to predict mechanical properties using alloying concentrations.

To evaluate the performance of the ML models, mean absolute error (MAE), mean squared error (MSE), root-mean squared error (RMSE), and coefficient of determination (R^2) for both train and test data were calculated as below [208]:

$$MAE = \frac{1}{n}\sum_{i=1}^{n}\left(y_i - \hat{y}_i\right), \tag{2}$$

$$MSE = \frac{1}{n}\sum_{i=1}^{n}\left(y_i - \hat{y}_i\right)^2, \tag{3}$$

$$RMSE = \sqrt{\frac{1}{n}\sum_{i=1}^{n}\left(y_i - \hat{y}_i\right)^2}, \tag{4}$$

$$R^2 = 1 - \frac{\sum_{i=1}^{n}\left(y_i - \hat{y}_i\right)^2}{\sum_{i=1}^{n}\left(y_i - \bar{y}_i\right)^2}, \tag{5}$$

where n represents the total data points, y_i is the observed values, $\bar{y}_i$ is the mean of the observed values, and $\hat{y}_i$ is the predicted values.

4.5 Results and Discussion

In this study, we calculated the yield stress for the randomly generated 250 high entropy alloy structures of Al-Co-Cr-Fe-Ni families. Single solid solutions such as FCC and BCC phases were considered in this study. Since short-range order (SRO) was found to have a significant impact on the thermodynamic properties [209] and mechanical properties [37] for the case of high entropy alloys, measured theoretically and experimentally, respectively. Therefore, we

introduced SRO in the HEA structures to capture the impact of SRO on the mechanical strength of AlCoCrFeNi HEA family. In total 250 random HEA structures containing 5 elements (Al, Co, Cr, Fe, and Ni) were created and relaxed using MD simulations. Half of these HEA structures were further processed using hybrid molecular dynamics/Monte Carlo (MD/MC) to introduce SRO in these HEAs. From these HEAs, the Warren-Cowley (WC) parameters for different element pairs were calculated to assess the SRO values.

The SRO or WC parameters for each element pair of Al-Co-Cr-Fe-Ni HEA families by varying the constituent elements along with Al concentration, as shown in Fig. 4.2. Different combinations of Al_xCoCr_yFeNi, $Al_xCoCrFe_yNi$, and $Al_xCoCrFeNi_y$ HEAs were created by changing Al and Cr, Al and Fe, Al and Ni concentration, respectively. Figure 4.2 exhibited SRO trend for various element pair for 3 FCC cases (x_{Al} = 0.25 + x_M = 1.75; M = Cr or Fe or Ni) and 3 BCC cases (x_{Al} = 1.5 + x_M = 0.5; M = Cr or Fe or Ni) among all selected HEA configurations. As usual, the most favorable Al-Fe pair and unfavorable Al-Al pair were observed for both FCC $Al_{0.25}CoCr_{1.75}FeNi$, FCC $Al_{0.25}CoCrFeNi_{1.75}$, BCC $Al_{1.5}CoCr_{0.5}FeNi$, and $Al_{1.5}CoCrFeNi_{0.5}$ HEAs. However, in the case of FCC $Al_{0.25}CoCrFe_{1.75}Ni$ HEA, Al-Fe SRO changed from most favorable to unfavorable element pair and Al-Co was the newly most favorable pair. Moreover, in BCC $Al_{1.5}CoCrFe_{0.5}Ni$ HEA, Al-Co was found to be the most favorable instead of Al-Fe pair. The SRO change in both HEA cases was shown in marked boxes in Fig. 4.3. These results demonstrate that different concentrations of constituent elements in the HEAs can produce different short-range ordering (SRO).

To examine the different SRO effect on mechanical strength of the HEA, we have analyzed the yield stress of $Al_xCo_yCrFeNi$ HEA for various Al and Co concentrations with the initial structures (without SRO) and the structures after MC swaps (with SRO). A significant increase in the yield stress can be observed with the SRO structures, as shown in Fig. 4.3. In the FCC cases, the increment values of yield stress ranges from 7.82% to 17.41% whereas for the BCC

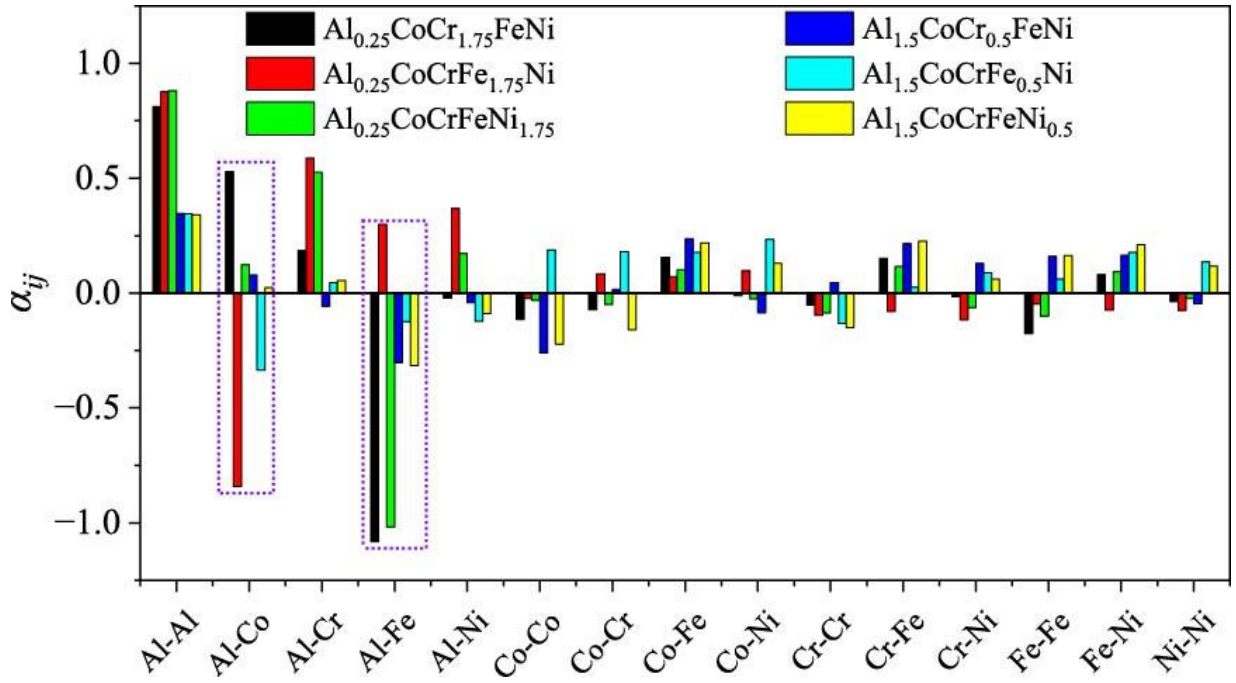

Figure 4.2: Evolution of SRO parameters among different element pairs in $Al_{0.25}CoCr_{1.75}FeNi$, $Al_{0.25}CoCrFe_{1.75}Ni$, $Al_{0.25}CoCrFeNi_{1.75}$, $Al_{1.5}CoCr_{0.5}FeNi$, $Al_{1.5}CoCrFe_{0.5}Ni$, and $Al_{1.5}CoCrFeNi_{0.5}$ HEAs.

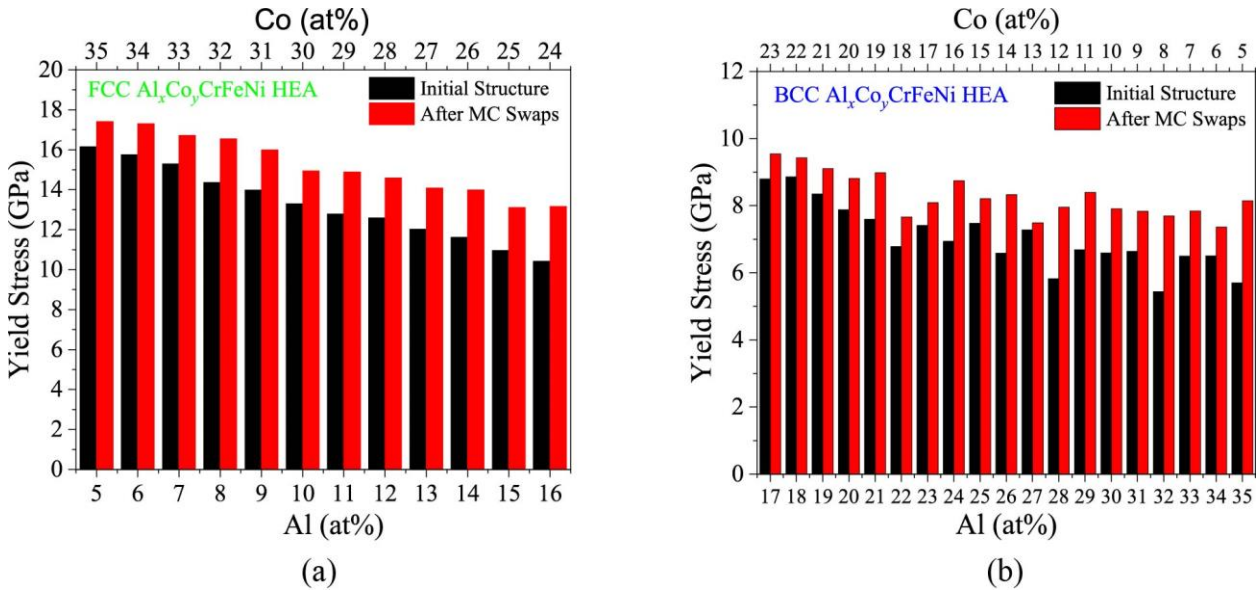

Figure 4.3: Yield Stress of (a) FCC $Al_xCo_yCrFeNi$ HEAs and (b) BCC $Al_xCo_yCrFeNi$ HEAs with random initial (without SRO) and MC swapped configurations (with SRO).

cases, the increment of yield stress values ranges from 2.93% to 42.79%. This type of increment in yield strength due to the SRO presence in the HEAs was also observed experimentally [210, 211].

Analyzing the above findings, it can be stated that the yield strength of various HEAs containing SRO should be considered for further investigation. However, it is important to note that the strain rates utilized in our MD simulations are several orders of magnitude higher than those in real experiments due to the intrinsic limitations of MD method. So, generally the calculated yield stress values from MD simulations are significantly higher than the experimental values. Despite this variation, the outcomes from our simulations remained consistent qualitatively with experimental findings, highlighting the importance of exploring these HEAs through MD simulations to gain diverse insights and applications.

SRO parameters of the selected HEAs in this study, originating from different alloying concentrations were calculated. Due to the extensive range of HEAs involved in this further investigation, modern data analytics, such as correlation analysis and machine learning were employed to predict the HEA property by leveraging the SRO parameters and composition concentrations.

It is well known that the inclusion of irrelevant features during machine learning leads to poor model performance [212]. Feature selection is a critical endeavor, particularly when working with regression models that yield numerical outputs, necessitating the utilization of numerical feature selection techniques to identify and eliminate redundant input features. Thus, Pearson's correlation coefficients (PCC) among the input features were calculated and a heatmap of feature matrix was generated, as shown in Fig. 4.4. The PCC values among features range from -1 to +1, where +1 represents strong positive correlation, -1 for strong negative correlation, and 0 value means no correlation. From the heatmap, features with a PCC score exceeding 0.9 were assessed for reduction, however, as none met this threshold, all features outlined here should be included for machine learning modeling.

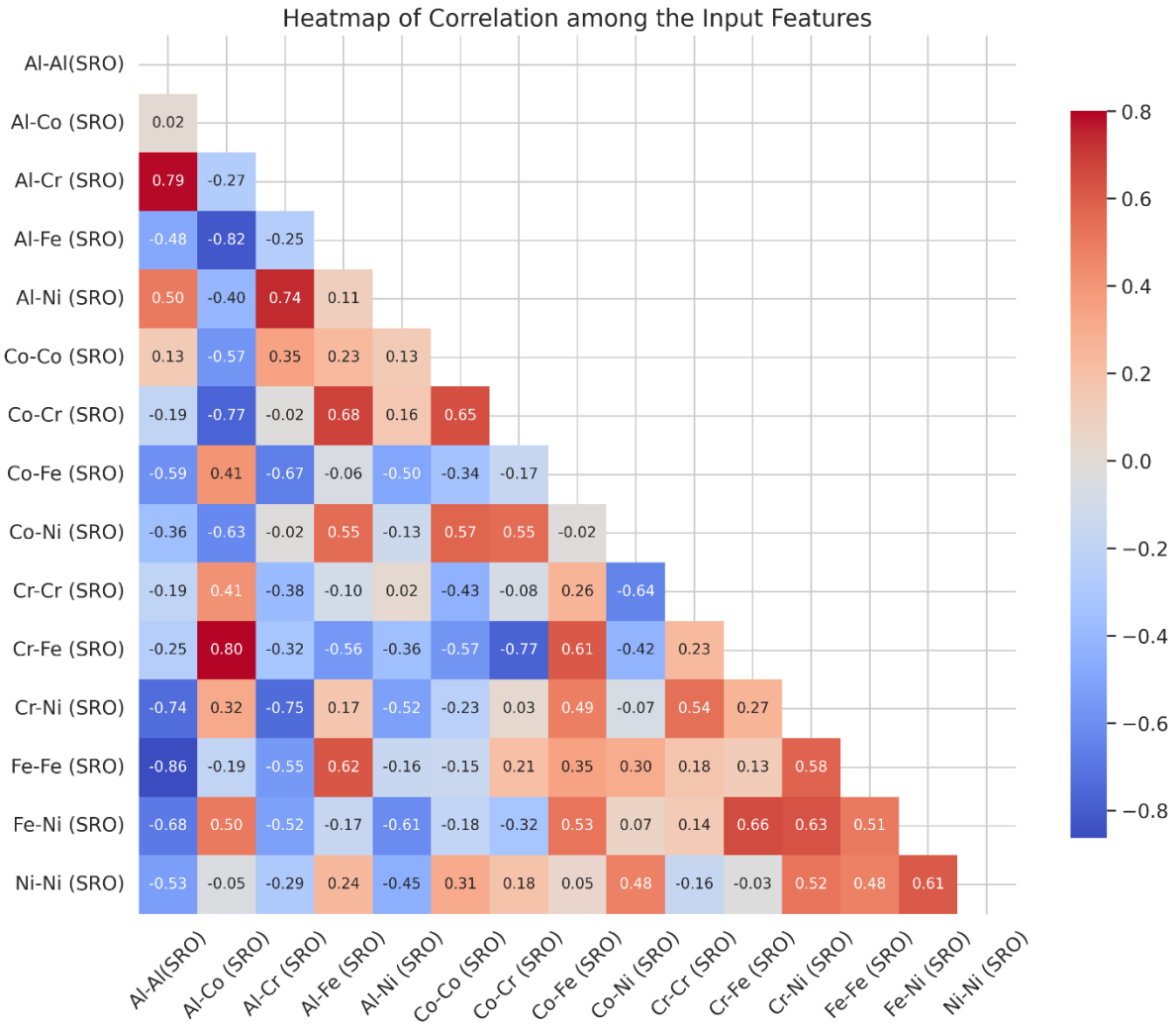

Figure 4.4: Heatmap of the correlation matrix among the features contained within the datasets.

To evaluate the sensitivity of the SRO parameters of each element pair with the target property of the HEAs, PCC values of the SRO parameters with yield stress were analyzed as shown in Fig. 4.5a. The assessment of the input feature relevance is further complemented by maximal information coefficient (MIC) analysis between the SRO parameters and yield stress, as displayed in Fig. 4.5b. The highest values for both PCC and MIC were observed in the Al-Al pair SRO, underscoring the significance of aluminum concentrations in HEAs. Besides, Al-Al pair, the Al-Cr, Fe-Fe, and Cr-Ni pair demonstrated higher PCC values, indicating a significant linear correlation with yield stress, whereas the Al-Fe, Fe-Fe, and Co-Ni pair SRO displayed higher MIC values, indicating a notable non-linear correlation with yield stress.

Various machine learning (ML) models to predict the yield stress were trained using SRO parameters and composition concentrations. The models were evaluated by several metrics, such as MAE, MSE, RMSE, and R^2 values. Higher values of R^2 in the training and testing datasets, coupled with lower values for other metrics, such as MAE, MSE, and RMSE indicate superior performance of a machine learning model in regression analysis. However, when comparing the R^2 values across different ML models, it is important to provide more consideration to the R^2 values calculated for the testing dataset. The performance metrics for all the selected ML models in this study were displayed in Table 4.1. It can be observed that the performance order of the ML models is: Random Forest (RF) Regression > Neural Network (NN) > Gradient Boosting Regression (GBR) > Linear Regression (LR) > Decision Tree Regression (DTR) > Ridge Regression (RR) > Support Vector Regression (SVR) > Least Absolute Shrinkage and Selection Operator Regression (LASSO) > Elastic Net Regression (ENR).

Among the selected ML models, the graph of the calculated and predicted value of yield stress for the three best performing ML models, i.e., Random Forest (RF) Regression, Neural Network (NN), and Gradient Boosting Regression (GBR) ML models, as shown in Fig. 4.6. It can be inferred that ensemble methods such as Random Forest Regression and Gradient Boosting Regression tend to outperform individual models such as Linear Regression or Support Vector Regression, and so on. This better predictive performance might be attributed to the complexity and flexibility offered by the ensemble methods that enable them to capture more convoluted

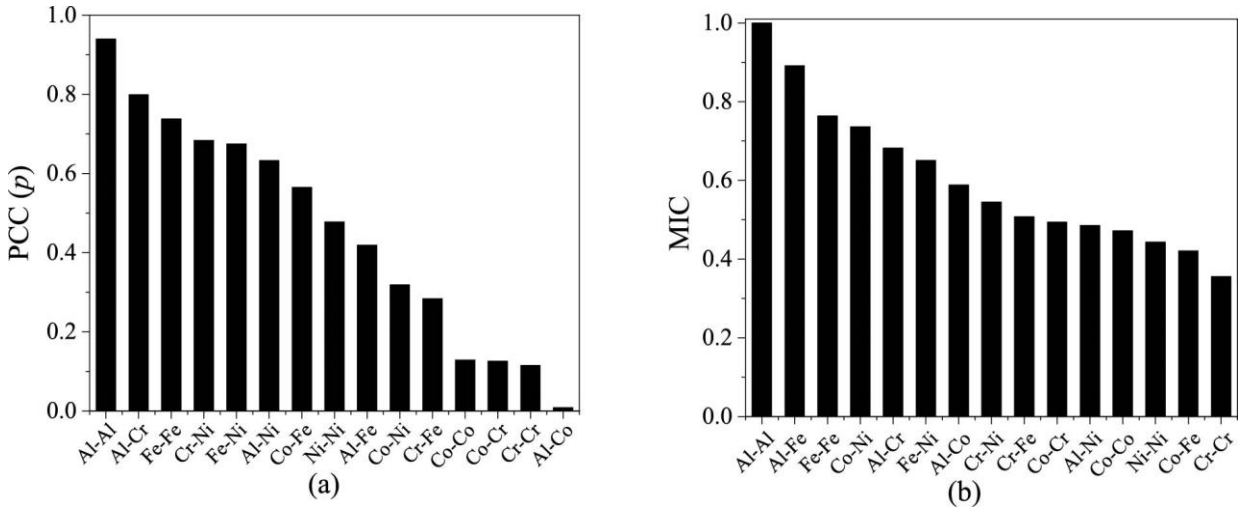

Figure 4.5: Correlations between the input features (WC parameters) and target property (Yield Stress) of Al-Co-Cr-Fe-Ni HEA family: (a) PCC values and (b) MIC values.

Table 4.1: Performance comparison among the selected ML models employing various metrics, such as mean absolute error (MAE), mean squared error (MSE), and root-mean squared error (RMSE), R^2 (train) and R^2 (test)

	MAE	MSE	RMSE	R^2 (train)	R^2 (test)
RF	0.62	0.642	0.801	0.996	0.973
NN	0.64	0.637	0.798	0.988	0.971
GBR	0.709	1.091	1.045	0.999	0.954
LR	0.836	1.213	1.101	0.967	0.947
DTR	0.94	1.402	1.184	1	0.941
RR	1.051	1.79	1.338	0.965	0.924
SVR	1.116	2.13	1.459	0.962	0.91
LASSO	1.051	1.79	1.338	0.87	0.809
ENR	1.051	1.79	1.338	0.848	0.796

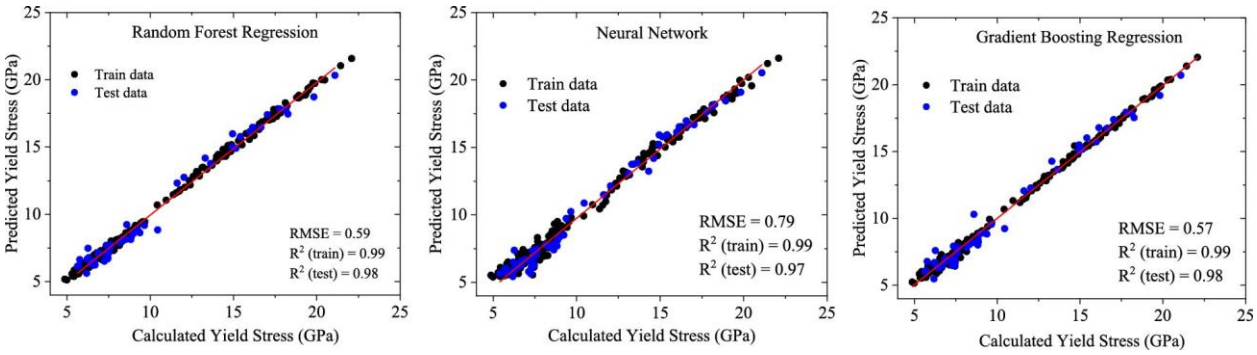

Figure 4.6: Scatter plot for the top performing three ML models: (a) Gradient Boosting Regression ML model, (b) Random Forest Regression ML model, and (c) Neural Network ML model trained using the atomistic simulation data of HEAs. The *x*- and *y*-axes represent the calculated yield strength and model-predicted yield strength.

patterns of SRO and relationships with the yield stress data. Additionally, Neural Network model performance falls between Random Forest Regression and Gradient Boosting Regression, demonstrating its capability to capture the complex SRO patterns here like ensemble methods while still maintaining a competitive edge over traditional linear models.

In general, the performance order may vary depending on the specific dataset and problem domain, highlighting the importance of selecting the suitable model based on the characteristics of the data and objective of the analysis. This study demonstrated the significance of understanding and manipulating SRO patterns in the HEAs to enhance the mechanical strength of the HEAs which will be beneficial to guide experimental designs in the development of HEAs.

4.6 Conclusions

Short-range orders (SRO) generating from different alloying concentration and their effect on the yield strength of the AlCoCrFeNi HEA families with different crystal structures was investigated using classical MD simulations, hybrid molecular dynamics/Monte Carlo (MD/MC) simulations, and modern data analytics. Different alloying concentration demonstrates significant changes in the short-range ordering pairs in the HEAs. The HEA structures containing SRO display superior mechanical strength compared to those lacking SRO. To capture the relationship between SRO patterns and yield stress, modern data analytics such as correlation analysis and machine learning modeling were employed. A heatmap of the correlation matrix between the features in the dataset demonstrates relevance of the features for ML modeling. The correlation analysis using MIC and PCC shows the linear and non-linear correlation strength of the SRO parameters of different element pairs with the yield strength in the HEAs. Several machine-learning models were trained using the SRO parameters of different element pairs for the selected alloying concentrations. Among all trained ML models, a performance comparison shows the best predictive models are Random Forest Regression, Neural Network, and Gradient Boosting Regression ML models to predict the yield stress of the HEAs based on the SRO parameters of the element pairs. This work will provide an insight into different interactions between element

pairs and physical properties of the HEA. Therefore, this study will contribute to a quantitative theory-guided design strategy for selecting HEA elements and tuning composition and local atomic order to control the structural, chemical, and mechanical properties.

Chapter 5

Summary and Future Work

5.1 Conclusions and Impacts

In this research, a comprehensive evaluation of HEAs was performed to study their physical properties effectively via fundamental investigation of thermal and electrical transport of HEAs utilizing various combinations of computational simulations. Effective manipulation of elemental compositions and structural configurations, including element concentration, size, mass mismatch, and chemical short-range ordering led to enhanced thermoelectric, thermodynamic, and mechanical properties of AlCoCrFeNi HEAs. The effect of aluminum concentration on the thermoelectric properties of $Al_xCoCrFeNi$ HEA was studied via classical molecular dynamics (MD) simulations, *ab initio* MD (AIMD) simulations, and semi-classical Boltzmann transport calculations, as discussed in Chapter 2. Local atomic order effect on the thermodynamic properties of the $Al_xCoCrFeNi$ HEA was conducted by employing classical MD simulations, hybrid molecular dynamics/Monte Carlo (MD/MC) simulations, and DFT calculations as demonstrated in Chapter 3. Finally, in Chapter 4, alloying concentration and short-range order effect on the mechanical properties of AlCoCrFeNi HEA families were investigated by implementing classical MD simulations, hybrid MD/MC simulations, and modern data analytics, such as correlation analysis and machine learning algorithms. The conclusions and impacts of the research outlined in each chapter are summarized below:

Chapter 2: This study explored the impact of various Al concentrations on the thermoelectric performance of $Al_xCoCrFeNi$ HEAs ($0 \leq x_{Al} \leq 2$) across a wide range of temperatures (300 K - 1200 K) using MD simulations, DFT calculations, and Boltzmann transport theory. With the increase of Al concentration, a phase shift from face-centered cubic (FCC) to body-centered cubic (BCC) was observed along with a significant enhancement in phonon scattering and suppressed phonon transport. Higher Al concentrations resulted in larger Seebeck coefficients, electrical conductivities, and electronic thermal conductivities due to increased electron carriers in BCC structures, which was supported by electronic band structures and density of states calculations. While temperature was found to have minor effects on phonon transport due to minimal inter-phonon scattering, both Seebeck coefficient and electrical conductivity exhibited

an increase with temperature, particularly at higher Al concentrations. This indicates that increasing Al content in the $Al_xCoCrFeNi$ HEA primarily enhances their thermoelectric performance at high temperatures. However, at lower temperatures, the enhanced phonon scattering due to significant mass mismatch also plays a critical role. In conclusion, this research will aid in the development of effective thermoelectric HEAs via manipulation of composition and temperature, making them suitable for high-temperature applications under extreme environments. Moreover, this work will contribute to the effective discovery of cost-effective, high-performance thermoelectric materials, which is essential to broader applications of thermoelectric energy conversion. Since thermoeletrics directly converts heat into electricity and vice versa, it will enable to harvest a huge portion of wasted heat and to improve power generation and refrigeration. As a result, society will benefit from low-cost electricity, clean energy, and less pollution.

Chapter 3: This study focused on understanding the relationship between local atomic arrangements, i.e., chemical short-range order (SRO) and thermodynamic properties such as lattice thermal conductivity, thermal expansion coefficient, and bulk modulus of $Al_xCoCrFeNi$ HEAs ($0 \leq x_{Al} \leq 2$) by employing a combination of hybrid MD/MC simulations, classical MD simulations and DFT calculations. SRO (or WC) parameters was utilized to assess the degree of ordering between constituent element pairs in the $Al_xCoCrFeNi$ HEAs. Through this investigation, Al-Fe exhibited as the most favorable element pair, whereas Al-Al was found to be the least favorable pair among all the studied HEAs. It was noted that the element pairs exhibiting higher SRO led to increased thermal conductivity, decreased thermal expansion, and enhanced bulk modulus of the HEAs. This observation can be attributed to the reduced phonon-scattering and enhanced energetic stability stemming from the increased SRO. This research offers valuable insights into the diverse interactions among element pairs and the physical characteristics of the HEAs. As a result, it will aid in developing a quantitative theory-guided approach to HEA design, facilitating the selection of HEA elements and composition concentrations to regulate the structural, chemical, and thermodynamic properties. Moreover,

this study will contribute to advancement of knowledge in HEA materials engineering by providing insights into their microstructural stability and performance under extreme conditions.

Chapter 4: This study represented the pioneering research aimed at implementing machine learning (ML) modeling to predict the mechanical strength of HEAs based on SROs arising from various alloying concentrations. A large number of HEA structures were created, and hybrid MD/MC simulations were utilized to incorporate the SRO in the HEA structures. Classical MD simulations were employed to the yield stress of AlCoCrFeNi HEA families with different crystal structures. It was found that different alloying concentrations induced significant changes in dominant SRO element pairs within HEAs. Moreover, structures containing SRO exhibited superior yield stress compared to those without SROs. Modern data analytics techniques, including correlation analysis and ML modeling, were utilized to capture the relationship between SRO patterns and yield stress of the HEAs. Correlation analysis using MIC and PCC assessed the linear and non-linear correlation strength between SRO parameters of different element pairs and HEA yield strength. Several ML learning models were trained using SRO parameters of different element pairs for the selected HEAs with various alloying concentrations. Random Forest Regression, Neural Network, and Gradient Boosting Regression were identified as the most effective models for predicting HEA yield stress based on these SRO parameters. In summary, this research provides insights into leveraging various interactions between element pairs to improve the mechanical strength of AlCoCrFeNi HEA families. In addition, the current work facilitates the discovery of novel HEAs with desired mechanical strength, an essential trait for construction and structural applications.

5.2 Recommendation for Future Studies

The following suggestions outline future research directions aimed at gaining deeper insights into the interplay among composition concentration, atomic structure, mass and thermal transport properties of high-entropy alloys (HEAs) to enhance their microstructural stability, mechanical strength, and energy conversion efficiency.

Advancing High-Entropy Alloys: Strategies for Enhanced Thermoelectric Performance through Structural Evaluation and Data Analytics

The research of Al concentrations effect on the thermoelectric performance of high-entropy alloys in Chapter 2 initiated a pioneer comprehensive computational study on assessing HEAs as efficient thermoelectric materials. However, further improvements in the thermoelectricity of HEAs are expected to necessitate comprehensive evaluations, including considerations of their atomic structures, such as addressing chemical short-range order and quantifying random structures. This thorough examination will provide deeper insights into thermoelectric properties of HEAs, enabling a more precise understanding of their properties and behavior and effective material design by considering atomic arrangement and interactions.

In the current research, either single-phase face-centered cubic (FCC) or single-phase body-centered cubic (BCC) crystal structures were taken into consideration in the thermoelectric performance evaluations. However, the coexistence of both FCC and BCC phases within the HEAs presents intriguing possibilities, potentially leading to notable observations and opportunities for enhancing thermoelectric HEA performance.

Moreover, the inclusion of modern data analytics techniques, specifically machine learning, can facilitate the study of a large number of HEAs and identify patterns in the relationships among alloy concentrations, atomic structures, and thermoelectric performance. By leveraging this advanced data analytics technique, experimentalists can make informed decisions when designing HEAs tailored for specific applications. This holistic approach of structural evaluation and predictive modeling will not only enhance the efficiency of design process but also pave the way for the development of high-performance thermoelectric HEAs.

Advancing High-Entropy Alloys: Unraveling Thermodynamic Properties and Short-Range Order Effects for Enhanced Design Strategies

Chapter 3 discusses the effect of short-range order (SRO) on the thermodynamic properties of the $Al_xCoCrFeNi$ HEAs such as lattice thermal conductivity, thermal expansion coefficient, and bulk modulus, which were calculated via atomistic simulations. While evaluating the short-range orders within HEAs, room temperature was selected for this study. However, conducting investigations across a broad temperature range to examine the effect of SROs on the thermodynamics properties will unveil the intricate relationship among the SRO, temperature, and thermodynamic properties. In particular, the inclusion of temperature in this analysis will be essential for understanding and optimizing HEAs for high-temperature applications.

Moreover, in the present study, only the aluminum content (x_{Al} = 0.3, 0.5, 0.75, 1.0, 1.5, and 2.0) in $Al_xCoCrFeNi$ HEAs was varied. However, in future studies, it is recommended to vary the concentrations of all constituent elements in HEAs to achieve the optimized SRO parameters that correlate with the enhanced thermodynamic properties of the HEAs. Modern data analytics can facilitate the inclusion of a large number of alloy concentrations for further investigation of the relationship between SRO and thermodynamic properties of HEAs. By incorporating ML modeling, it becomes feasible to identify both favorable and unfavorable element pairs, aiding in the design of the HEAs with targeted thermodynamic properties.

Advancing High-Entropy Alloy Design: Unraveling the Relationship Between Short-Range Ordering and Mechanical Properties through Atomistic Simulations and Machine Learning

Alloying concentration and short-range order effect on mechanical properties of the AlCoCrFeNi HEA families discussed in Chapter 4 were investigated employing classical MD simulations, Monte Carlo simulations and machine learning (ML) modeling. Though this research contains a significant number of HEA configurations to predict the mechanical strength, it is limited to Al, Co, Cr, Fe, and Ni compositions. Future research efforts should explore a broader range of

concentrations for the constituent elements, extending beyond the currently selected alloying levels. Moreover, incorporating additional compositions, such as Cu or Mn, into the investigation of high-entropy alloys (HEAs) is expected to be beneficial for cost and weight reduction. Furthermore, this research can be extended to a wider array of alloy compositions, particularly refractory HEAs containing elements like Mo, Nb, Ta, W, and V. This exploration will provide deeper insights into the influence of various alloy concentrations on short-range ordering (SRO) and its consequent effects on mechanical properties.

It is recommended to expand the investigation to include other mechanical properties beyond yield strength, such as ductility, fracture toughness, and fatigue resistance. This can provide a more comprehensive understanding of the relationship between SRO and mechanical behavior in HEAs.

As short-range ordering remains a relatively novel area of investigation in HEA research, it would be intriguing to conduct experimental studies to verify the observed correlations between SRO, mechanical properties, and predictions made by machine learning models. This could involve conducting mechanical tests on actual HEA samples to compare with simulation results. It is advised to collaborate with materials engineers to create and experiment with new HEA compositions. This collaboration will enable the utilization of knowledge obtained from this study to guide the development of new HEAs with customized structural, chemical, and mechanical properties tailored for specific applications.

Bibliography

[1] J.R. Davis, Alloying: understanding the basics, ASM international, 2001.
[2] G.L. Chen and C.T. Liu, Moisture induced environmental embrittlement of intermetallics, International Materials Reviews **46**(6) 253-270 (2001).
[3] A. Peker and W.L. Johnson, A highly processable metallic glass: Zr41.2Ti13.8Cu12.5Ni10.0Be22.5, Applied Physics Letters **63**(17) 2342-2344 (1993).
[4] A. Inoue and A. Takeuchi, Recent progress in bulk glassy, nanoquasicrystalline and nanocrystalline alloys, Materials Science and Engineering: A **375-377** 16-30 (2004).
[5] W.H. Wang, C. Dong, and C.H. Shek, Bulk metallic glasses, Materials Science and Engineering: R: Reports **44**(2) 45-89 (2004).
[6] A.L. Greer, Confusion by design, Nature **366**(6453) 303-304 (1993).
[7] A.J.B. Vincent, A study of three multicomponent alloys, University of Sussex Library, 1981.
[8] B. Cantor, I.T.H. Chang, P. Knight, and A.J.B. Vincent, Microstructural development in equiatomic multicomponent alloys, Materials Science and Engineering: A **375-377** 213-218 (2004).
[9] B. Cantor, Multicomponent and High Entropy Alloys, Entropy, 2014, pp. 4749-4768.
[10] J.W. Yeh, S.K. Chen, S.J. Lin, J.Y. Gan, T.S. Chin, T.T. Shun, C.H. Tsau, and S.Y. Chang, Nanostructured High-Entropy Alloys with Multiple Principal Elements: Novel Alloy Design Concepts and Outcomes, Advanced Engineering Materials **6**(5) 299-303 (2004).
[11] J.W. Yeh, S.K. Chen, and Y.L. Chen, Novel alloy concept, challenges and opportunities of high-entropy alloys, CRC Press2007.
[12] J.-W. Yeh, Alloy Design Strategies and Future Trends in High-Entropy Alloys, JOM **65**(12) 1759-1771 (2013).
[13] B.S. Murty, J.W. Yeh, S. Ranganathan, and P.P. Bhattacharjee, High-Entropy Alloys, Elsevier Science2019.
[14] S. Praveen and H.S. Kim, High-Entropy Alloys: Potential Candidates for High-Temperature Applications – An Overview, Advanced Engineering Materials **20**(1) 1700645 (2018).
[15] F. Otto, Y. Yang, H. Bei, and E.P. George, Relative effects of enthalpy and entropy on the phase stability of equiatomic high-entropy alloys, Acta Materialia **61**(7) 2628-2638 (2013).
[16] Z.G. Zhu, K.H. Ma, X. Yang, and C.H. Shek, Annealing effect on the phase stability and mechanical properties of (FeNiCrMn)(100−x)Cox high entropy alloys, Journal of Alloys and Compounds **695** 2945-2950 (2017).
[17] O.N. Senkov, J.D. Miller, D.B. Miracle, and C. Woodward, Accelerated exploration of multi-principal element alloys with solid solution phases, Nature Communications **6**(1) 6529 (2015).
[18] D. Ma, B. Grabowski, F. Körmann, J. Neugebauer, and D. Raabe, Ab initio thermodynamics of the CoCrFeMnNi high entropy alloy: Importance of entropy contributions beyond the configurational one, Acta Materialia **100** 90-97 (2015).
[19] S. Praveen, B.S. Murty, and R.S. Kottada, Alloying behavior in multi-component AlCoCrCuFe and NiCoCrCuFe high entropy alloys, Materials Science and Engineering: A **534** 83-89 (2012).

[20] S. Guo and C.T. Liu, Phase stability in high entropy alloys: Formation of solid-solution phase or amorphous phase, Progress in Natural Science: Materials International **21**(6) 433-446 (2011).
[21] Y.P. Wang, H.Z. Fu, B.S. Li, and H.I.o.T.H. Micro/Nano Technology Research Center, Solid solution or intermetallics in a high-entropy alloy, **11** (2009).
[22] I. Toda-Caraballo, J.S. Wróbel, S.L. Dudarev, D. Nguyen-Manh, and P.E.J. Rivera-Díaz-del-Castillo, Interatomic spacing distribution in multicomponent alloys, Acta Materialia **97** 156-169 (2015).
[23] R. Kozak, A. Sologubenko, and W. Steurer, Single-phase high-entropy alloys – an overview, Zeitschrift für Kristallographie - Crystalline Materials **230**(1) 55-68 (2015).
[24] S. Yin, J. Ding, M. Asta, and R.O. Ritchie, Ab initio modeling of the energy landscape for screw dislocations in body-centered cubic high-entropy alloys, npj Computational Materials **6**(1) 110 (2020).
[25] W. Feng, Y. Qi, and S. Wang, Effects of Short-Range Order on the Magnetic and Mechanical Properties of FeCoNi(AlSi)x High Entropy Alloys, Metals **7**(11) 482 (2017).
[26] A. Tamm, A. Aabloo, M. Klintenberg, M. Stocks, and A. Caro, Atomic-scale properties of Ni-based FCC ternary, and quaternary alloys, Acta Materialia **99** 307-312 (2015).
[27] D.B. Miracle and O.N. Senkov, A critical review of high entropy alloys and related concepts, Acta Materialia **122** 448-511 (2017).
[28] P.K. Huang, J.W. Yeh, T.T. Shun, and S.K. Chen, Multi-Principal-Element Alloys with Improved Oxidation and Wear Resistance for Thermal Spray Coating, Advanced Engineering Materials **6**(1-2) 74-78 (2004).
[29] J.W. Yeh, Recent progress in high-entropy alloys; Progres recents dans les alliages a haute entropie, **31** (2006).
[30] J.W. Yeh, Y.L. Chen, S.J. Lin, and S.K. Chen, High-Entropy Alloys – A New Era of Exploitation, Materials Science Forum **560** 1-9 (2007).
[31] Y.H. Jo, S. Jung, W.M. Choi, S.S. Sohn, H.S. Kim, B.J. Lee, N.J. Kim, and S. Lee, Cryogenic strength improvement by utilizing room-temperature deformation twinning in a partially recrystallized VCrMnFeCoNi high-entropy alloy, Nature Communications **8**(1) 15719 (2017).
[32] M.A. Hemphill, T. Yuan, G.Y. Wang, J.W. Yeh, C.W. Tsai, A. Chuang, and P.K. Liaw, Fatigue behavior of Al0.5CoCrCuFeNi high entropy alloys, Acta Materialia **60**(16) 5723-5734 (2012).
[33] M.-H. Chuang, M.-H. Tsai, W.-R. Wang, S.-J. Lin, and J.-W. Yeh, Microstructure and wear behavior of AlxCo1.5CrFeNi1.5Tiy high-entropy alloys, Acta Materialia **59**(16) 6308-6317 (2011).
[34] J.Y. He, H. Wang, Y. Wu, X.J. Liu, T.G. Nieh, and Z.P. Lu, High-temperature plastic flow of a precipitation-hardened FeCoNiCr high entropy alloy, Materials Science and Engineering: A **686** 34-40 (2017).
[35] E.J. Pickering and N.G. Jones, High-entropy alloys: a critical assessment of their founding principles and future prospects, International Materials Reviews **61**(3) 183-202 (2016).

[36] D.B. Miracle, J.D. Miller, O.N. Senkov, C. Woodward, M.D. Uchic, and J. Tiley, Exploration and development of high entropy alloys for structural applications, Entropy **16**(1) 494-525 (2014).
[37] Q. Ding, Y. Zhang, X. Chen, X. Fu, D. Chen, S. Chen, L. Gu, F. Wei, H. Bei, Y. Gao, M. Wen, J. Li, Z. Zhang, T. Zhu, R.O. Ritchie, and Q. Yu, Tuning element distribution, structure and properties by composition in high-entropy alloys, Nature **574**(7777) 223-227 (2019).
[38] Q.-J. Li, H. Sheng, and E. Ma, Strengthening in multi-principal element alloys with local-chemical-order roughened dislocation pathways, Nature Communications **10**(1) 3563 (2019).
[39] D.B. Miracle, Critical Assessment 14: High entropy alloys and their development as structural materials, MATERIALS SCIENCE AND TECHNOLOGY **31**(10) 1142-1147 (2015).
[40] H. Bhadeshia, High entropy alloys, MATERIALS SCIENCE AND TECHNOLOGY **31**(10) 1139-1141 (2015).
[41] Y. Zhang, T.T. Zuo, Z. Tang, M.C. Gao, K.A. Dahmen, P.K. Liaw, and Z.P. Lu, Microstructures and properties of high-entropy alloys, Progress in Materials Science **61** 1-93 (2014).
[42] H.Y. Diao, R. Feng, K.A. Dahmen, and P.K. Liaw, Fundamental deformation behavior in high-entropy alloys: An overview, Current Opinion in Solid State and Materials Science **21**(5) 252-266 (2017).
[43] M.-H. Tsai and J.-W. Yeh, High-Entropy Alloys: A Critical Review, Materials Research Letters **2**(3) 107-123 (2014).
[44] S. Ranganathan, Alloyed pleasures: Multimetallic cocktails, Current science **85**(5) 1404-1406 (2003).
[45] Y.F. Kao, T.J. Chen, S.K. Chen, and J.W. Yeh, Microstructure and mechanical property of as-cast, -homogenized, and -deformed $Al_xCoCrFeNi$ ($0 \le x \le 2$) high-entropy alloys, Journal of Alloys and Compounds **488**(1) 57-64 (2009).
[46] W.R. Wang, W.L. Wang, S.C. Wang, Y.C. Tsai, C.H. Lai, and J.W. Yeh, Effects of Al addition on the microstructure and mechanical property of $Al_xCoCrFeNi$ high-entropy alloys, Intermetallics **26** 44-51 (2012).
[47] H.P. Chou, Y.S. Chang, S.K. Chen, and J.W. Yeh, Microstructure, thermophysical and electrical properties in $Al_xCoCrFeNi$ ($0 \le x \le 2$) high-entropy alloys, Materials Science and Engineering: B **163**(3) 184-189 (2009).
[48] S.A. Uporov, R.E. Ryltsev, V.A. Bykov, S.K. Estemirova, and D.A. Zamyatin, Microstructure, phase formation and physical properties of AlCoCrFeNiMn high-entropy alloy, Journal of Alloys and Compounds **820** 153228 (2020).
[49] R. John, A. Karati, J. Joseph, D. Fabijanic, and B.S. Murty, Microstructure and mechanical properties of a high entropy alloy with a eutectic composition (AlCoCrFeNi2.1) synthesized by mechanical alloying and spark plasma sintering, Journal of Alloys and Compounds **835** 155424 (2020).
[50] G. Shang, L. Jiang, Z.-Z. Liu, and X.-G. Lu, High-throughput experimental study on the microstructural and compositional variations of mechanical properties for AlCoCrFeNi high entropy alloys, Journal of Alloys and Compounds **917** 165513 (2022).
[51] D. Marx and J. Hutter, Ab initio molecular dynamics: Theory and implementation, Modern methods and algorithms of quantum chemistry **1**(301-449) 141 (2000).

[52] F.M. Bickelhaupt and E.J. Baerends, Kohn-Sham Density Functional Theory: Predicting and Understanding Chemistry, Reviews in Computational Chemistry2000, pp. 1-86.
[53] M.P. Allen, Introduction to molecular dynamics simulation, Computational soft matter: from synthetic polymers to proteins **23**(1) 1-28 (2004).
[54] J.P. Bouanich, Site-site Lennard-Jones potential parameters for N2, O2, H2, CO and CO2, Journal of Quantitative Spectroscopy and Radiative Transfer **47**(4) 243-250 (1992).
[55] L.A. Girifalco and V.G. Weizer, Application of the Morse Potential Function to Cubic Metals, Physical Review **114**(3) 687-690 (1959).
[56] V.V. Ogorodnikov and Y.I. Rogovoi, Buckingham-potential parameters and relations between them for solids, Powder Metallurgy and Metal Ceramics **33**(5) 327-333 (1995).
[57] M.S. Daw and M.I. Baskes, Embedded-atom method: Derivation and application to impurities, surfaces, and other defects in metals, Physical Review B **29**(12) 6443-6453 (1984).
[58] J. Nord, K. Albe, P. Erhart, and K. Nordlund, Modelling of compound semiconductors: analytical bond-order potential for gallium, nitrogen and gallium nitride, Journal of Physics: Condensed Matter **15**(32) 5649 (2003).
[59] A. Ramasubramaniam, M. Itakura, and E.A. Carter, Interatomic potentials for hydrogen in $\ensuremath{\alpha}$--iron based on density functional theory, Physical Review B **79**(17) 174101 (2009).
[60] M.S. Daw, S.M. Foiles, and M.I. Baskes, The embedded-atom method: a review of theory and applications, Materials Science Reports **9**(7) 251-310 (1993).
[61] A. Cao, Y. Wei, and E. Ma, Grain boundary effects on plastic deformation and fracture mechanisms in Cu nanowires: Molecular dynamics simulations, Physical Review B **77**(19) 195429 (2008).
[62] H. Grubmüller, H. Heller, A. Windemuth, and K. Schulten, Generalized Verlet Algorithm for Efficient Molecular Dynamics Simulations with Long-range Interactions, Molecular Simulation **6**(1-3) 121-142 (1991).
[63] L. Verlet, Computer "Experiments" on Classical Fluids. I. Thermodynamical Properties of Lennard-Jones Molecules, Physical Review **159**(1) 98-103 (1967).
[64] W.F. Van Gunsteren and H.J.C. Berendsen, A Leap-frog Algorithm for Stochastic Dynamics, Molecular Simulation **1**(3) 173-185 (1988).
[65] J.R. Ray and H. Zhang, Correct microcanonical ensemble in molecular dynamics, Physical Review E **59**(5) 4781-4785 (1999).
[66] S. Nosé, A molecular dynamics method for simulations in the canonical ensemble, Molecular Physics **52**(2) 255-268 (1984).
[67] D. Fincham, Choice of timestep in molecular dynamics simulation, Computer Physics Communications **40**(2) 263-269 (1986).
[68] C.A. Mead and D.G. Truhlar, On the determination of Born–Oppenheimer nuclear motion wave functions including complications due to conical intersections and identical nuclei, The Journal of Chemical Physics **70**(5) 2284-2296 (1979).
[69] K. Laasonen, A. Pasquarello, R. Car, C. Lee, and D. Vanderbilt, Car-Parrinello molecular dynamics with Vanderbilt ultrasoft pseudopotentials, Physical Review B **47**(16) 10142-10153 (1993).

[70] N. Metropolis, A.W. Rosenbluth, M.N. Rosenbluth, A.H. Teller, and E. Teller, Equation of State Calculations by Fast Computing Machines, The Journal of Chemical Physics **21**(6) 1087-1092 (1953).
[71] D. Landau and K. Binder, A guide to Monte Carlo simulations in statistical physics, Cambridge university press, 2021.
[72] P. Allen, Boltzmann theory and resistivity of metals, Kluwer International Series In Engineering And Computer Science 219-250 (1996).
[73] J.M. Ziman, Electrons and phonons: the theory of transport phenomena in solids, Oxford university press2001.
[74] C. Hurd, The Hall effect in metals and alloys, Springer Science & Business Media2012.
[75] G.K.H. Madsen and D.J. Singh, BoltzTraP. A code for calculating band-structure dependent quantities, Computer Physics Communications **175**(1) 67-71 (2006).
[76] W.W. Schulz, P.B. Allen, and N. Trivedi, Hall coefficient of cubic metals, Physical Review B **45**(19) 10886-10890 (1992).
[77] P.B. Allen, W.E. Pickett, and H. Krakauer, Anisotropic normal-state transport properties predicted and analyzed for high-Tc oxide superconductors, Physical Review B **37**(13) 7482-7490 (1988).
[78] W. Jia, H. Wang, M. Chen, D. Lu, L. Lin, R. Car, E. Weinan, and L. Zhang, Pushing the Limit of Molecular Dynamics with Ab Initio Accuracy to 100 Million Atoms with Machine Learning, SC20: International Conference for High Performance Computing, Networking, Storage and Analysis, 2020, pp. 1-14.
[79] C.W. Park, M. Kornbluth, J. Vandermause, C. Wolverton, B. Kozinsky, and J.P. Mailoa, Accurate and scalable graph neural network force field and molecular dynamics with direct force architecture, npj Computational Materials **7**(1) 73 (2021).
[80] C. Nyshadham, M. Rupp, B. Bekker, A.V. Shapeev, T. Mueller, C.W. Rosenbrock, G. Csányi, D.W. Wingate, and G.L.W. Hart, Machine-learned multi-system surrogate models for materials prediction, npj Computational Materials **5**(1) 51 (2019).
[81] S. Yin, Y. Zuo, A. Abu-Odeh, H. Zheng, X.-G. Li, J. Ding, S.P. Ong, M. Asta, and R.O. Ritchie, Atomistic simulations of dislocation mobility in refractory high-entropy alloys and the effect of chemical short-range order, Nature Communications **12**(1) 4873 (2021).
[82] Z. Pei, J. Yin, J.A. Hawk, D.E. Alman, and M.C. Gao, Machine-learning informed prediction of high-entropy solid solution formation: Beyond the Hume-Rothery rules, npj Computational Materials **6**(1) 50 (2020).
[83] J.M. Rickman, H.M. Chan, M.P. Harmer, J.A. Smeltzer, C.J. Marvel, A. Roy, and G. Balasubramanian, Materials informatics for the screening of multi-principal elements and high-entropy alloys, Nature Communications **10**(1) 2618 (2019).
[84] J. Zhang, X. Liu, S. Bi, J. Yin, G. Zhang, and M. Eisenbach, Robust data-driven approach for predicting the configurational energy of high entropy alloys, Materials & Design **185** 108247 (2020).
[85] S. Shafeie, S. Guo, Q. Hu, H. Fahlquist, P. Erhart, and A. Palmqvist, High-entropy alloys as high-temperature thermoelectric materials, Journal of Applied Physics **118**(18) 184905 (2015).
[86] J.M. Cowley, Short-Range Order and Long-Range Order Parameters, Physical Review **138**(5A) A1384-A1389 (1965).

[87] H.A. Rahnamaye Aliabad, M. Ghazanfari, I. Ahmad, and M.A. Saeed, *Ab initio* calculations of structural, optical and thermoelectric properties for $CoSb_3$ and ACo_4Sb_{12} (A=La, Tl and Y) compounds, Computational Materials Science **65** 509-519 (2012).
[88] B. Poudel, Q. Hao, Y. Ma, Y. Lan, A. Minnich, B. Yu, X. Yan, D. Wang, A. Muto, D. Vashaee, X. Chen, J. Liu, M.S. Dresselhaus, G. Chen, and Z. Ren, High-thermoelectric performance of nanostructured bismuth antimony telluride bulk alloys, Science **320**(5876) 634 (2008).
[89] L.E. Bell, Cooling, heating, generating power, and recovering waste heat with thermoelectric systems, Science **321**(5895) 1457 (2008).
[90] J. He, M.G. Kanatzidis, and V.P. Dravid, High performance bulk thermoelectrics via a panoscopic approach, Materials Today **16**(5) 166-176 (2013).
[91] S. LeBlanc, S.K. Yee, M.L. Scullin, C. Dames, and K.E. Goodson, Material and manufacturing cost considerations for thermoelectrics, Renewable and Sustainable Energy Reviews **32** 313-327 (2014).
[92] D.M. Rowe, CRC handbook of thermoelectrics, CRC Press2018.
[93] G.J. Snyder and E.S. Toberer, Complex thermoelectric materials, Co-Published with Macmillan Publishers Ltd., UK2010.
[94] J. de Boor, T. Dasgupta, H. Kolb, C. Compere, K. Kelm, and E. Mueller, Microstructural effects on thermoelectric efficiency: A case study on magnesium silicide, Acta Materialia **77** 68-75 (2014).
[95] S. Chen, K.C. Lukas, W. Liu, C.P. Opeil, G. Chen, and Z. Ren, Effect of Hf concentration on thermoelectric properties of nanostructured n-type half-Heusler materials $Hf_xZr_{1-x}NiSn_{0.99}Sb_{0.01}$, Advanced Energy Materials **3**(9) 1210-1214 (2013).
[96] Q. Shen, L. Chen, T. Goto, T. Hirai, J. Yang, G.P. Meisner, and C. Uher, Effects of partial substitution of Ni by Pd on the thermoelectric properties of ZrNiSn-based half-Heusler compounds, Applied Physics Letters **79**(25) 4165-4167 (2001).
[97] S. Populoh, M.H. Aguirre, O.C. Brunko, K. Galazka, Y. Lu, and A. Weidenkaff, High figure of merit in (Ti,Zr,Hf)NiSn half-Heusler alloys, Scripta Materialia **66**(12) 1073-1076 (2012).
[98] B. Gludovatz, A. Hohenwarter, D. Catoor, E.H. Chang, E.P. George, and R.O. Ritchie, A fracture-resistant high-entropy alloy for cryogenic applications, Science **345**(6201) 1153 (2014).
[99] Y. Pei, X. Shi, A. LaLonde, H. Wang, L. Chen, and G.J. Snyder, Convergence of electronic bands for high performance bulk thermoelectrics, Nature **473**(7345) 66-69 (2011).
[100] Y.F. Kao, S.K. Chen, T.J. Chen, P.C. Chu, J.W. Yeh, and S.J. Lin, Electrical, magnetic, and Hall properties of $Al_xCoCrFeNi$ high-entropy alloys, Journal of Alloys and Compounds **509**(5) 1607-1614 (2011).
[101] Y. Shi, L. Collins, R. Feng, C. Zhang, N. Balke, P.K. Liaw, and B. Yang, Homogenization of $Al_xCoCrFeNi$ high-entropy alloys with improved corrosion resistance, Corrosion Science **133** 120-131 (2018).
[102] W. Feng, Y. Qi, and S. Wang, Effects of Mn and Al addition on structural and magnetic properties of FeCoNi-based high entropy alloys, Materials Research Express **5**(10) 106511 (2018).
[103] S. Li, X. Ni, and F. Tian, *Ab initio* predicted alloying effects on the elastic properties of $Al_xHf_{1-x}NbTaTiZr$ high entropy alloys, Coatings **5**(3) 366-377 (2015).

[104] H. Zhang, X. Sun, S. Lu, Z. Dong, X. Ding, Y. Wang, and L. Vitos, Elastic properties of $Al_xCrMnFeCoNi$ ($0 \leq x \leq 5$) high-entropy alloys from *ab initio* theory, Acta Materialia **155** 12-22 (2018).
[105] F. Tian, L. Delczeg, N. Chen, L.K. Varga, J. Shen, and L. Vitos, Structural stability of $NiCoFeCrAl_x$ high-entropy alloy from *ab initio* theory, Physical Review B **88**(8) 085128 (2013).
[106] S. Wang, Atomic Structure Modeling of Multi-Principal-Element Alloys by the Principle of Maximum Entropy, Entropy **15**(12) 5536-5548 (2013).
[107] L. Xie, P. Brault, A.L. Thomann, and J.M. Bauchire, AlCoCrCuFeNi high entropy alloy cluster growth and annealing on silicon: A classical molecular dynamics simulation study, Applied Surface Science **285** 810-816 (2013).
[108] D. Farkas and A. Caro, Model interatomic potentials for Fe–Ni–Cr–Co–Al high-entropy alloys, Journal of Materials Research **35**(22) 3031-3040 (2020).
[109] J. Cai and Y.Y. Ye, Simple analytical embedded-atom-potential model including a long-range force for fcc metals and their alloys, Physical Review B **54**(12) 8398-8410 (1996).
[110] M.A.A. Hasan, J. Wang, Y.C. Lim, A. Hu, and S. Shin, Concentration dependence of hydrogen diffusion in α-iron from atomistic perspectives, International Journal of Hydrogen Energy **44**(51) 27876-27884 (2019).
[111] M.C. Payne, M.P. Teter, D.C. Allan, T.A. Arias, and J.D. Joannopoulos, Iterative minimization techniques for *ab initio* total-energy calculations: molecular dynamics and conjugate gradients, Reviews of Modern Physics **64**(4) 1045-1097 (1992).
[112] S. Shin, M. Kaviany, T. Desai, and R. Bonner, Roles of atomic restructuring in interfacial phonon transport, Physical Review B **82**(8) 081302 (2010).
[113] R.T. Azuah, L.R. Kneller, Y. Qiu, P.L.W. Tregenna-Piggott, C.M. Brown, J.R.D. Copley, and R.M. Dimeo, DAVE: A comprehensive software suite for the reduction, visualization, and analysis of low energy neutron spectroscopic data, J Res Natl Inst Stand Technol **114**(6) 341-358 (2009).
[114] J. Fourier, Analytical theory of heat, translated with notes of A. Freeman, 1955.
[115] G. Kresse and J. Furthmüller, Efficient iterative schemes for *ab initio* total-energy calculations using a plane-wave basis set, Physical Review B **54**(16) 11169-11186 (1996).
[116] P.E. Blöchl, Projector augmented-wave method, Physical Review B **50**(24) 17953-17979 (1994).
[117] J.P. Perdew, K. Burke, and M. Ernzerhof, Generalized gradient approximation made simple, Physical Review Letters **77**(18) 3865-3868 (1996).
[118] M. Methfessel and A.T. Paxton, High-precision sampling for Brillouin-zone integration in metals, Physical Review B **40**(6) 3616-3621 (1989).
[119] S. Nosé, A unified formulation of the constant temperature molecular dynamics methods, Journal of Chemical Physics **81**(1) 511-519 (1984).
[120] J. Yang, H. Li, T. Wu, W. Zhang, L. Chen, and J. Yang, Evaluation of half-Heusler compounds as thermoelectric materials based on the calculated electrical transport properties, Advanced Functional Materials **18**(19) 2880-2888 (2008).
[121] G.K.H. Madsen, Automated search for new thermoelectric materials: The case of LiZnSb, Journal of the American Chemical Society **128**(37) 12140-12146 (2006).

[122] T. Thonhauser, T.J. Scheidemantel, J.O. Sofo, J.V. Badding, and G.D. Mahan, Thermoelectric properties of Sb_2Te_3 under pressure and uniaxial stress, Physical Review B **68**(8) 085201 (2003).
[123] L.J. Santodonato, Y. Zhang, M. Feygenson, C.M. Parish, M.l.C. Gao, R.J.K. Weber, J.C. Neuefeind, Z. Tang, and P.K. Liaw, Deviation from high-entropy configurations in the atomic distributions of a multi-principal-element alloy, Nature Communications **6**(1) 5964 (2015).
[124] J.C. Huang, Evaluation of tribological behavior of Al-Co-Cr-Fe-Ni high entropy alloy using molecular dynamics simulation, Scanning **34**(5) 325-331 (2012).
[125] C. Li, M. Zhao, J.C. Li, and Q. Jiang, B2 structure of high-entropy alloys with addition of Al, Journal of Applied Physics **104**(11) 113504 (2008).
[126] Z. Tang, M.C. Gao, H. Diao, T. Yang, J. Liu, T. Zuo, Y. Zhang, Z. Lu, Y. Cheng, Y. Zhang, K.A. Dahmen, P.K. Liaw, and T. Egami, Aluminum alloying effects on lattice types, microstructures, and mechanical behavior of high-entropy alloys systems, JOM **65**(12) 1848-1858 (2013).
[127] K. Jin, B.C. Sales, G.M. Stocks, G.D. Samolyuk, M. Daene, W.J. Weber, Y. Zhang, and H. Bei, Tailoring the physical properties of Ni-based single-phase equiatomic alloys by modifying the chemical complexity, Scientific Reports **6**(1) 20159 (2016).
[128] Y.K. Weng, A. Yousefzadi Nobakht, S. Shin, K.D. Kihm, and D.S. Aaron, Effects of mass and interaction mismatches on in-plane and cross-plane thermal transport of Si-doped graphene, International Journal of Heat and Mass Transfer **149** 120979 (2021).
[129] M. Kaviany, Heat transfer physics, Cambridge University Press2014.
[130] D. Koskimaki and J.T. Waber, Calculation of thermodynamic information based on the density of states curves of two allotropes of iron, NBS, 1971, pp. 741-754.
[131] E.C. Snow and J.T. Waber, The APW energy bands for the body centered and face centered cubic modifications of the 3d transition metals, Acta Metallurgica **17**(5) 623-635 (1969).
[132] P. Singh, A. Marshal, A.V. Smirnov, A. Sharma, G. Balasubramanian, K.G. Pradeep, and D.D. Johnson, Tuning phase stability and short-range order through Al doping in $(CoCrFeMn)_{100-x}Al_x$ high-entropy alloys, Physical Review Materials **3**(7) 075002 (2019).
[133] L.H. Bennett, Electronic density of states, US National Bureau of Standards, 1971.
[134] Y.F. Ye, Q. Wang, J. Lu, C.T. Liu, and Y. Yang, High-entropy alloy: challenges and prospects, Materials Today **19**(6) 349-362 (2016).
[135] L. Wang, F. Zhang, S. Yan, G. Yu, J. Chen, J. He, and F. Yin, Microstructure evolution and mechanical properties of atmosphere plasma sprayed AlCoCrFeNi high-entropy alloy coatings under post-annealing, Journal of Alloys and Compounds **872** 159607 (2021).
[136] C.C. Tasan, Y. Deng, K.G. Pradeep, M.J. Yao, H. Springer, and D. Raabe, Composition Dependence of Phase Stability, Deformation Mechanisms, and Mechanical Properties of the CoCrFeMnNi High-Entropy Alloy System, JOM **66**(10) 1993-2001 (2014).
[137] T. Egami, W. Guo, P.D. Rack, and T. Nagase, Irradiation Resistance of Multicomponent Alloys, Metallurgical and Materials Transactions A **45**(1) 180-183 (2014).
[138] M. Widom, W.P. Huhn, S. Maiti, and W. Steurer, Hybrid Monte Carlo/Molecular Dynamics Simulation of a Refractory Metal High Entropy Alloy, Metallurgical and Materials Transactions A **45**(1) 196-200 (2014).

[139] R.L. McGreevy, Reverse Monte Carlo modelling, Journal of Physics: Condensed Matter **13**(46) R877-R913 (2001).
[140] Z. Lei, X. Liu, Y. Wu, H. Wang, S. Jiang, S. Wang, X. Hui, Y. Wu, B. Gault, P. Kontis, D. Raabe, L. Gu, Q. Zhang, H. Chen, H. Wang, J. Liu, K. An, Q. Zeng, T.-G. Nieh, and Z. Lu, Enhanced strength and ductility in a high-entropy alloy via ordered oxygen complexes, Nature **563**(7732) 546-550 (2018).
[141] X. Huang, X. Dong, L. Liu, and P. Li, Liquid structure of Al-Si alloy: A molecular dynamics simulation, Journal of Non-Crystalline Solids **503-504** 182-185 (2019).
[142] E. Antillon, C. Woodward, S.I. Rao, B. Akdim, and T.A. Parthasarathy, Chemical short range order strengthening in a model FCC high entropy alloy, Acta Materialia **190** 29-42 (2020).
[143] D. Modupeola, P. Patricia, A. Samson, and M. Ntombi, High Entropy Alloys for Aerospace Applications, in: G.-B. Mofid, A. Aly-Mousaad (Eds.), Aerodynamics, IntechOpen, Rijeka, 2019, p. Ch. 7.
[144] X. Yan and Y. Zhang, Functional properties and promising applications of high entropy alloys, Scripta Materialia **187** 188-193 (2020).
[145] H. Ren, R.R. Chen, X.F. Gao, T. Liu, G. Qin, S.P. Wu, and J.J. Guo, High-performance AlCoCrFeNi high entropy alloy with marine application perspective, Journal of Materials Research and Technology **25** 6751-6763 (2023).
[146] Y. Geng, H. Tan, L. Wang, A.K. Tieu, J. Chen, J. Cheng, and J. Yang, Nano-coupled heterostructure induced excellent mechanical and tribological properties in AlCoCrFeNi high entropy alloy, Tribology International **154** 106662 (2021).
[147] L.J. Santodonato, P.K. Liaw, R.R. Unocic, H. Bei, and J.R. Morris, Predictive multiphase evolution in Al-containing high-entropy alloys, Nature Communications **9**(1) 4520 (2018).
[148] A. Sharma, P. Singh, D. D. Johnson, P. K. Liaw, and G. Balasubramanian, Atomistic clustering-ordering and high-strain deformation of an Al0.1CrCoFeNi high-entropy alloy, Scientific Reports **6**(1) 31028 (2016).
[149] M.A.A. Hasan, J. Wang, S. Shin, D.A. Gilbert, P.K. Liaw, N. Tang, W.L.N.C. Liyanage, L. Santodonato, L. DeBeer-Schmitt, and N.P. Butch, Effects of aluminum content on thermoelectric performance of AlxCoCrFeNi high-entropy alloys, Journal of Alloys and Compounds **883** 160811 (2021).
[150] Z. Sun, C. Shi, L. Gao, S. Lin, and W. Li, Thermal physical properties of high entropy alloy Al0.3CoCrFeNi at elevated temperatures, Journal of Alloys and Compounds **901** 163554 (2022).
[151] S. Plimpton, Fast Parallel Algorithms for Short-Range Molecular Dynamics, Journal of Computational Physics **117**(1) 1-19 (1995).
[152] D.J. Evans and B.L. Holian, The Nose–Hoover thermostat, The Journal of Chemical Physics **83**(8) 4069-4074 (1985).
[153] G.J. Martyna, D.J. Tobias, and M.L. Klein, Constant pressure molecular dynamics algorithms, The Journal of Chemical Physics **101**(5) 4177-4189 (1994).
[154] B. Sadigh, P. Erhart, A. Stukowski, A. Caro, E. Martinez, and L. Zepeda-Ruiz, Scalable parallel Monte Carlo algorithm for atomistic simulations of precipitation in alloys, Physical Review B **85**(18) 184203 (2012).

[155] A. Stukowski, Visualization and analysis of atomistic simulation data with OVITO–the Open Visualization Tool, Modelling and Simulation in Materials Science and Engineering **18**(1) 015012 (2010).
[156] M.S. Green, Markoff Random Processes and the Statistical Mechanics of Time-Dependent Phenomena. II. Irreversible Processes in Fluids, The Journal of Chemical Physics **22**(3) 398-413 (1954).
[157] R. Kubo, Statistical-Mechanical Theory of Irreversible Processes. I. General Theory and Simple Applications to Magnetic and Conduction Problems, Journal of the Physical Society of Japan **12**(6) 570-586 (1957).
[158] H. Nejat Pishkenari, E. Mohagheghian, and A. Rasouli, Molecular dynamics study of the thermal expansion coefficient of silicon, Physics Letters A **380**(48) 4039-4043 (2016).
[159] G. Clavier, N. Desbiens, E. Bourasseau, V. Lachet, N. Brusselle-Dupend, and B. Rousseau, Computation of elastic constants of solids using molecular simulation: comparison of constant volume and constant pressure ensemble methods, Molecular Simulation **43**(17) 1413-1422 (2017).
[160] S.M. Rassoulinejad-Mousavi, Y. Mao, and Y. Zhang, Evaluation of copper, aluminum, and nickel interatomic potentials on predicting the elastic properties, Journal of Applied Physics **119**(24) 244304 (2016).
[161] F. Birch, Finite Elastic Strain of Cubic Crystals, Physical Review **71**(11) 809-824 (1947).
[162] F. Murnaghan, The Compressibility of Media under extreme Pressures in Proceeding of the National Academy of Sciences, (1944).
[163] S. Guo, C. Ng, J. Lu, and C.T. Liu, Effect of valence electron concentration on stability of fcc or bcc phase in high entropy alloys, Journal of Applied Physics **109**(10) 103505 (2011).
[164] G. Zhang, X. Yang, W. Qi, Y. Li, W. Wang, Y. Chen, J. Li, and L. Li, Effect of Co on phase stability and mechanical behavior of CoxCrFeNiMnAl0.3 high entropy alloys with micro/nano hierarchical structure, Materials & Design **215** 110442 (2022).
[165] Y. Ma, Q. Wang, B.B. Jiang, C.L. Li, J.M. Hao, X.N. Li, C. Dong, and T.G. Nieh, Controlled formation of coherent cuboidal nanoprecipitates in body-centered cubic high-entropy alloys based on Al2(Ni,Co,Fe,Cr)14 compositions, Acta Materialia **147** 213-225 (2018).
[166] H.-P. Chou, Y.-S. Chang, S.-K. Chen, and J.-W. Yeh, Microstructure, thermophysical and electrical properties in AlxCoCrFeNi ($0 \leq x \leq 2$) high-entropy alloys, Materials Science and Engineering: B **163**(3) 184-189 (2009).
[167] B. Cheng, F. Zhang, H. Lou, X. Chen, P.K. Liaw, J. Yan, Z. Zeng, Y. Ding, and Q. Zeng, Pressure-induced phase transition in the AlCoCrFeNi high-entropy alloy, Scripta Materialia **161** 88-92 (2019).
[168] X. Huang, L. Liu, X. Duan, W. Liao, J. Huang, H. Sun, and C. Yu, Atomistic simulation of chemical short-range order in HfNbTaZr high entropy alloy based on a newly-developed interatomic potential, Materials & Design **202** 109560 (2021).
[169] F. Körmann, Y. Ikeda, B. Grabowski, and M.H.F. Sluiter, Phonon broadening in high entropy alloys, npj Computational Materials **3**(1) 36 (2017).
[170] L. Xie, P. Brault, A.-L. Thomann, and J.-M. Bauchire, AlCoCrCuFeNi high entropy alloy cluster growth and annealing on silicon: A classical molecular dynamics simulation study, Applied Surface Science **285** 810-816 (2013).

[171] Y. Qi, T. He, H. Xu, Y. Hu, M. Wang, and M. Feng, Effects of microstructure and temperature on the mechanical properties of nanocrystalline CoCrFeMnNi high entropy alloy under nanoscratching using molecular dynamics simulation, Journal of Alloys and Compounds **871** 159516 (2021).
[172] A.S. Bundela and M.R. Rahul, Machine learning-enabled framework for the prediction of mechanical properties in new high entropy alloys, Journal of Alloys and Compounds **908** 164578 (2022).
[173] C. Wen, Y. Zhang, C. Wang, D. Xue, Y. Bai, S. Antonov, L. Dai, T. Lookman, and Y. Su, Machine learning assisted design of high entropy alloys with desired property, Acta Materialia **170** 109-117 (2019).
[174] Z. Rao, P.-Y. Tung, R. Xie, Y. Wei, H. Zhang, A. Ferrari, T.P.C. Klaver, F. Körmann, P.T. Sukumar, A. Kwiatkowski da Silva, Y. Chen, Z. Li, D. Ponge, J. Neugebauer, O. Gutfleisch, S. Bauer, and D. Raabe, Machine learning–enabled high-entropy alloy discovery, Science **378**(6615) 78-85 (2022).
[175] W. Huang, P. Martin, and H.L. Zhuang, Machine-learning phase prediction of high-entropy alloys, Acta Materialia **169** 225-236 (2019).
[176] X. Liu, J. Zhang, and Z. Pei, Machine learning for high-entropy alloys: Progress, challenges and opportunities, Progress in Materials Science **131** 101018 (2023).
[177] R. Jain, U. Lee, S. Samal, and N. Park, Machine-learning-guided phase identification and hardness prediction of Al-Co-Cr-Fe-Mn-Nb-Ni-V containing high entropy alloys, Journal of Alloys and Compounds **956** 170193 (2023).
[178] X. Huang, C. Jin, C. Zhang, H. Zhang, and H. Fu, Machine learning assisted modelling and design of solid solution hardened high entropy alloys, Materials & Design **211** 110177 (2021).
[179] L. Zhang, K. Qian, B.W. Schuller, and Y. Shibuta, Prediction on Mechanical Properties of Non-Equiatomic High-Entropy Alloy by Atomistic Simulation and Machine Learning, Metals, 2021, p. 922.
[180] L. Chen, A. Jarlöv, H.L. Seet, M.L.S. Nai, Y. Li, and K. Zhou, Exploration of V–Cr–Fe–Co–Ni high-entropy alloys with high yield strength: A combination of machine learning and molecular dynamics simulation, Computational Materials Science **217** 111888 (2023).
[181] Y.V. Krishna, U.K. Jaiswal, and R.M. R, Machine learning approach to predict new multiphase high entropy alloys, Scripta Materialia **197** 113804 (2021).
[182] Y. Zhang, C. Wen, C. Wang, S. Antonov, D. Xue, Y. Bai, and Y. Su, Phase prediction in high entropy alloys with a rational selection of materials descriptors and machine learning models, Acta Materialia **185** 528-539 (2020).
[183] L. Zhang, H. Chen, X. Tao, H. Cai, J. Liu, Y. Ouyang, Q. Peng, and Y. Du, Machine learning reveals the importance of the formation enthalpy and atom-size difference in forming phases of high entropy alloys, Materials & Design **193** 108835 (2020).
[184] U.K. Jaiswal, Y. Vamsi Krishna, M.R. Rahul, and G. Phanikumar, Machine learning-enabled identification of new medium to high entropy alloys with solid solution phases, Computational Materials Science **197** 110623 (2021).

[185] Y. Sun, Z. Lu, X. Liu, Q. Du, H. Xie, J. Lv, R. Song, Y. Wu, H. Wang, S. Jiang, and Z. Lu, Prediction of Ti-Zr-Nb-Ta high-entropy alloys with desirable hardness by combining machine learning and experimental data, Applied Physics Letters **119**(20) 201905 (2021).
[186] J. Li, B. Xie, Q. Fang, B. Liu, Y. Liu, and P.K. Liaw, High-throughput simulation combined machine learning search for optimum elemental composition in medium entropy alloy, Journal of Materials Science & Technology **68** 70-75 (2021).
[187] J. Xiong, S.-Q. Shi, and T.-Y. Zhang, Machine learning of phases and mechanical properties in complex concentrated alloys, Journal of Materials Science & Technology **87** 133-142 (2021).
[188] Z. Li, S. Zhao, R.O. Ritchie, and M.A. Meyers, Mechanical properties of high-entropy alloys with emphasis on face-centered cubic alloys, Progress in Materials Science **102** 296-345 (2019).
[189] Y.-F. Kao, T.-J. Chen, S.-K. Chen, and J.-W. Yeh, Microstructure and mechanical property of as-cast, -homogenized, and -deformed AlxCoCrFeNi ($0 \leq x \leq 2$) high-entropy alloys, Journal of Alloys and Compounds **488**(1) 57-64 (2009).
[190] W.-R. Wang, W.-L. Wang, S.-C. Wang, Y.-C. Tsai, C.-H. Lai, and J.-W. Yeh, Effects of Al addition on the microstructure and mechanical property of AlxCoCrFeNi high-entropy alloys, Intermetallics **26** 44-51 (2012).
[191] M.J. Yao, K.G. Pradeep, C.C. Tasan, and D. Raabe, A novel, single phase, non-equiatomic FeMnNiCoCr high-entropy alloy with exceptional phase stability and tensile ductility, Scripta Materialia **72-73** 5-8 (2014).
[192] Z. Fu, W. Chen, H. Wen, D. Zhang, Z. Chen, B. Zheng, Y. Zhou, and E.J. Lavernia, Microstructure and strengthening mechanisms in an FCC structured single-phase nanocrystalline Co25Ni25Fe25Al7.5Cu17.5 high-entropy alloy, Acta Materialia **107** 59-71 (2016).
[193] J. Ding, Q. Yu, M. Asta, and R.O. Ritchie, Tunable stacking fault energies by tailoring local chemical order in CrCoNi medium-entropy alloys, Proceedings of the National Academy of Sciences **115**(36) 8919-8924 (2018).
[194] Y. Ma, Q. Wang, C. Li, L.J. Santodonato, M. Feygenson, C. Dong, and P.K. Liaw, Chemical short-range orders and the induced structural transition in high-entropy alloys, Scripta Materialia **144** 64-68 (2018).
[195] F.X. Zhang, S. Zhao, K. Jin, H. Xue, G. Velisa, H. Bei, R. Huang, J.Y.P. Ko, D.C. Pagan, J.C. Neuefeind, W.J. Weber, and Y. Zhang, Local Structure and Short-Range Order in a NiCoCr Solid Solution Alloy, Physical Review Letters **118**(20) 205501 (2017).
[196] J. Benesty, J. Chen, Y. Huang, and I. Cohen, Pearson correlation coefficient, Noise reduction in speech processing, Springer2009, pp. 1-4.
[197] J.B. Kinney and G.S. Atwal, Equitability, mutual information, and the maximal information coefficient, Proceedings of the National Academy of Sciences **111**(9) 3354-3359 (2014).
[198] D.N. Reshef, Y.A. Reshef, H.K. Finucane, S.R. Grossman, G. McVean, P.J. Turnbaugh, E.S. Lander, M. Mitzenmacher, and P.C. Sabeti, Detecting Novel Associations in Large Data Sets, Science **334**(6062) 1518-1524 (2011).
[199] J.L. Rodgers and W.A. Nicewander, Thirteen Ways to Look at the Correlation Coefficient, The American Statistician **42**(1) 59-66 (1988).

[200] L. Qiao, Y. Liu, and J. Zhu, A focused review on machine learning aided high-throughput methods in high entropy alloy, Journal of Alloys and Compounds **877** 160295 (2021).
[201] H. Chang, Y. Tao, P.K. Liaw, and J. Ren, Phase prediction and effect of intrinsic residual strain on phase stability in high-entropy alloys with machine learning, Journal of Alloys and Compounds **921** 166149 (2022).
[202] V.L. Deringer and G. Csányi, Machine learning based interatomic potential for amorphous carbon, Physical Review B **95**(9) 094203 (2017).
[203] A.P. Bartók, J. Kermode, N. Bernstein, and G. Csányi, Machine Learning a General-Purpose Interatomic Potential for Silicon, Physical Review X **8**(4) 041048 (2018).
[204] J. Wang, S. Shin, and S. Lee, Interatomic Potential Model Development: Finite-Temperature Dynamics Machine Learning, Advanced Theory and Simulations **3**(2) 1900210 (2020).
[205] S. Chmiela, A. Tkatchenko, E. Sauceda Huziel, I. Poltavsky, T. Schütt Kristof, and K.-R. Müller, Machine learning of accurate energy-conserving molecular force fields, Science Advances **3**(5) 1603015 (2017).
[206] Z. Li, J.R. Kermode, and A. De Vita, Molecular Dynamics with On-the-Fly Machine Learning of Quantum-Mechanical Forces, Physical Review Letters **114**(9) 096405 (2015).
[207] A.R. Natarajan and A. Van der Ven, Machine-learning the configurational energy of multicomponent crystalline solids, npj Computational Materials **4**(1) 56 (2018).
[208] X. Jiang, H.-Q. Yin, C. Zhang, R.-J. Zhang, K.-Q. Zhang, Z.-H. Deng, G.-q. Liu, and X.-h. Qu, An materials informatics approach to Ni-based single crystal superalloys lattice misfit prediction, Computational Materials Science **143** 295-300 (2018).
[209] M.A.A. Hasan, S. Shin, and P.K. Liaw, Short-range order effects on the thermodynamic behavior of AlxCoCrFeNi high-entropy alloys, Computational Materials Science **239** 112980 (2024).
[210] Y.P. Wang, B.S. Li, M.X. Ren, C. Yang, and H.Z. Fu, Microstructure and compressive properties of AlCrFeCoNi high entropy alloy, Materials Science and Engineering: A **491**(1) 154-158 (2008).
[211] Q. Li, T.W. Zhang, J.W. Qiao, S.G. Ma, D. Zhao, P. Lu, B. Xu, and Z.H. Wang, Superior tensile properties of Al0.3CoCrFeNi high entropy alloys with B2 precipitated phases at room and cryogenic temperatures, Materials Science and Engineering: A **767** 138424 (2019).
[212] G.H. John, R. Kohavi, and K. Pfleger, Irrelevant Features and the Subset Selection Problem, in: W.W. Cohen, H. Hirsh (Eds.), Machine Learning Proceedings 1994, Morgan Kaufmann, San Francisco (CA), 1994, pp. 121-129.

Journal Publications

- **Md Abdullah Al Hasan**, Seungha Shin, and Peter K. Liaw, "Short-range order effects on the thermodynamic behavior of $Al_xCoCrFeNi$ high-entropy alloys", Computational Materials Science, **239**, 112980 (2024).
- **Md Abdullah Al Hasan,** Jiaqi Wang, Seungha Shin*, Dustin A. Gilbert, Peter K. Liaw, Nan Tang, W.L. Namila C. Liyanage, Louis Santodonato, Lisa DeBeer-Schmitt, and Nicholas P. Butch, "Effects of aluminum content on thermoelectric performance of $Al_xCoCrFeNi$ high-entropy alloys", Journal of Alloys and Compounds, **883**, 160811 (2021).
- **Md Abdullah Al Hasan**, Jiaqi Wang, Yong Chae Lim, Anming Hu, and Seungha Shin*, "Concentration dependence of hydrogen diffusion in α-iron from atomistic perspectives", International Journal of Hydrogen Energy, **44**(51), 27876-27884 (2019).
- Yongchao Yu, Yangbao Deng, **Md Abdullah Al Hasan**, Yanfeng Bai, Ruozhou Li, Shuguang Deng, Pooran C. Joshi, Seungha Shin, and Anming Hu, "Femtosecond laser-induced non-thermal welding for a single Cu nanowire glucose sensor" Nanoscale Advances, **2**(3), 1195-1205 (2020).
- **Md Abdullah Al Hasan,** Seungha Shin*, and Peter K. Liaw "Effects of alloying concentration and short-range order on the mechanical strength of AlCoCrFeNi high-entropy alloys via atomistic simulation and modern data analytics", *in preparation.*

Conference Presentations/Proceedings

- **Md Abdullah Al Hasan**, Seungha Shin*, and Peter K. Liaw, “Short-Range Order Effect on the Thermodynamic Properties of $Al_xCoCrFeNi$ High-Entropy Alloys,” International Conference on High-Entropy Materials (ICHEM), Knoxville, TN, Jun. 18-22, 2023.
- **Md Abdullah Al Hasan**, Yu-Kai Weng, and Seungha Shin*, “Coupling of Electric Field Driven Ion Transport with Convective Flow in Graphene Nanochannels,” TMS 2023 Annual Meeting & Exhibition, San Diego, CA, Mar. 19-23, 2023.
- **Md Abdullah Al Hasan**, Seungha Shin*, and Peter K. Liaw, “Effects of Short-Range Order on the Thermodynamic Properties of $Al_xCoCrFeNi$ High-Entropy Alloys,” TMS 2022 Annual Meeting & Exhibition, Anaheim, CA, Feb. 27 - Mar. 03, 2022.
- Seungha Shin*, **Md Abdullah Al Hasan**, Jiaqi Wang, Yu-Kai Weng, and Dustin A. Gilbert, “Thermal Transport Calculation of High Entropy Alloys for Thermoelectric Applications,” TMS 2020 Annual Meeting & Exhibition, San Diego, CA, Feb. 23-27, 2020 (invited).
- Md Moinul Islam, **Md Abdullah Al Hasan**, Md Mominur Rahman, Md Mashiur Rahaman*, "Validation of Numerical Model for Cook Stove Using Reynolds Averaged Navier-Stokes Based Solver". AIP Conference Proceedings. 1919(1), 020040 (2017).

Vita

Md Abdullah Al Hasan was born in December 1992, to the parents of Md Abul Kashem and Hosne Ara Begum, in Chattogram, Bangladesh. He graduated with a Bachelor of Science with a major in Naval Architecture and Marine Engineering from Bangladesh University of Engineering and Technology (BUET) in February 2017, and a concurrent Master of Science with a major in Mechanical Engineering from the University of Tennessee in December 2021. He came to the United States for pursuing his Ph.D. at the University of Tennessee - Knoxville in August 2018. Since then, he has been working as a graduate research assistant in Dr. Seungha Shin's Nanoscale Heat Transfer Laboratory in the Department of Mechanical, Aerospace, and Biomedical Engineering. His research interest is fundamental investigation of heat and mass transfer in materials via multiscale simulations such as classical molecular dynamics simulations, quantum mechanical simulations, and machine learning.